STATISTICAL DYNAMICS OF SOFT LOW-FRICTION GRAINS

Thesis
for the degree of

doctor rerum naturalium (Dr. rer. nat.)

approved by the Faculty of Natural Sciences of Otto von Guericke University Magdeburg

by M.Eng. Jing Wang

born on 29.10.1993 in Hebei, China

Examiner: Prof. Dr. Ralf Stannarius

Prof. Dr. Devaraj van der Meer

submitted on 24.01.2023 defended on 27.06.2023

Abstract

Granular systems are very common in nature and have been applied widely in industry. Even though granular systems have been studied for decades, the behavior of some granular material systems has been rarely studied before, for example, soft, smooth grains.

To study the behaviors of granular material, discharging particles in a silo is one of the experiments to characterize the statistical dynamics of granular systems. A silo is also an important container for the storage of particles in industry. Shear cells are another important experimental setup to study on rheology of granular systems, especially on shear banding.

In this thesis, we systematically study the statistical dynamics of granular systems, especially soft, low-friction grains. The first chapter is about the introduction of granular systems and the experimental methods to characterize granular behavior. The second chapter starts on the intermittent flow of soft grains passing narrow orifices compared with hard beads. Then the next chapter discusses mixtures of soft and hard grains in silo discharge and both of these two chapters strongly demonstrate the influence of elasticity and friction of grains on silo discharge and probabilities of clog formation. Continuing on the research of the factor of silo discharge and clogging, we also present the effect of an obstacle in silo discharge with soft, low-friction grains in the 4th chapter. Additionally, based on identical features of soft grains, the dynamics of soft grains in a shear cell is presented in the 5th chapter. An MRI method is applied in this chapter to track the shear flow of soft particles. In the end, the summary of soft granular systems and the outlook of this research are given in the 6th chapter.

Keywords: soft elastic grain, granular flow, dynamics in granular systems

Zusammenfassung

Granulares Systeme sind in der Natur weit verbreitet und werden in der Industrie vielseitig angewendet. Obwohl granulare Systeme seit Jahrzehnten untersucht werden, ist das Verhalten verschiedener granularer Systeme, beispielsweise weicher, glatter Körner, unzureichend verstanden.

Um das Verhalten von granularem Material zu untersuchen, wird beispielsweise das Ausfließen von Partikeln aus einem Silo in Experimenten angewendet, um die statistische Dynamik des Schüttgutes zu charakterisieren. Silos sind wichtige Behälter für die Lagerung von Partikeln in der Industrie. Scherzellen sind ein weiterer wichtiger experimenteller Aufbau zur Untersuchung der Rheologie granularer Systeme, insbesondere von Scherbändern.

In dieser Arbeit untersuchen wir systematisch die statistische Dynamik granularer Systeme, insbesondere aus weichen, reibungsarmen Partikeln. Das erste Kapitel befasst sich mit der Einführung granularer Systeme und der experimentellen Methoden zur Charakterisierung des granularen Verhaltens. Das zweite Kapitel beginnt mit dem intermittierenden Fluss weicher Partikel, die eine enge Öffnung passieren, im Vergleich zu harten Kugeln. Dann, nach dem nächsten Kapitel, wird die Mischung von weichen und harten Körnern bei der Siloentleerung diskutiert, und beide Kapitel deuten stark auf den Einfluss der Elastizität und Reibung von Körnern auf die Siloentleerung und die Wahrscheinlichkeit der Bildung von Verstopfungen hin. Als Fortsetzung der Erforschung der Auswirkung auf Siloausfluss und Verstopfung stellen wir im 4. Kapitel auch den Effekt von Hindernissen beim Siloausfluss von weichen, reibungsarmen Körnern vor. Zusätzlich wird, basierend auf den gleichen Merkmalen der weichen Körper, die Dynamik in Scherzellen im 5. Kapitel vorgestellt. Technisch wird in diesem Kapitel eine MRI-Methode angewendet, um den Scherfluss von weichen Partikeln zu verfolgen. Abschließend wird im 6. Kapitel die Zusammenfassung und der Ausblick dieser Forschung gegeben.

Schlüsselworte: Weiche elastischer granulare Partikel, granularer Fluss, Dynamik von Schüttgütern

Contents

1 Introduction

1.1 Background

Granular materials consist of a collection of discrete particles. When external energy is transferred into granular systems, the collections of discrete particles, which would have fluid-like behavior, are usually called granular flow. The granular flow exists widely in agriculture and industry, e. g. grinding of grains, transportation of the crop, storage or unloading of the wheat, presence in daily life e. g. pedestrian dynamics, and traffic flow [1]. It also exists in natural environments, e. g. landslide, debris flow, and even the interaction or evolution of stars in the universe.

Granular flow has been widely and actively studied for decades, which includes funnel flow [2–4], ramp flow [5], shearing flow [6, 7] and so on. Granular flow is often classified into three different regimes [8]: Three distinct regimes can be identified: a dense quasi-static regime characterized by gradual deformations and frictional particle interactions, a gaseous regime marked by rapid and dilute flow where particles interact through collisions, and an intermediate liquid regime where the material remains dense yet flows akin to a liquid, with particles interacting through both collisions and friction [9–11]. Moreover, the granular flow may not only show up in one of the regimes as presented above but also transform between different regimes, like dilute-dense flow or dense flow-jamming [12–14].

1.1.1 Silo flow

The storage and transfer of granular materials generally apply in silos which are containers with outlets, usually at their bottom. Generally speaking, the systems allowing granular materials to flow in or out could be treated as a silo, and the flow is correspondingly called silo flow. A simple silo flow is the flow in an hourglass as a timer. Once grains are piled up over a certain height, the outflow rate stabilizes, remaining constant and independent of the filling height. In 1895, H.A. Janssen [15, 16] inferred the saturation of pressure with height from experiments with corn and explained it by the mechanics that the walls carry part of the weight, the maximum pressure exerted on the cell walls is proportional to the side length of the cell profile, which is famous as Janssen effect. The Janssen effect continues to serve as a significant source of inspiration for numerous researchers up to the present. The description is shown in Fig 1.1, $p_{s,max}$ is the maximum pressure in the horizontal direction against the wall, μ is the friction coefficient between corn and column walls, s is the side length of the quadratic cell profile, dh is the height of a corn layer, m_s is the specific weight of the corn.

The essential interaction in granular flow results from friction and elasticity because of particles' deformations. Particles in local regions can assemble into robust force chains, causing granular systems with stability akin to crystals. Moreover, granular flow exhibits energy-dissipative behavior and demonstrates local non-equilibrium attributes [17, 18]. The study of the silo flow mainly involves granular dynamics at the orifices. In general, the flow through orifices is primarily categorized into 3 patterns [19]: continuous flow, intermittent flow, and clogging. When orifices are large enough, particles can continuously flow out. Otherwise, if orifices are small enough, arches would be formed by particles above orifices and then block orifices. When arches are not stable, they can autonomously dissolve, allowing particles to resume flowing, thus constituting intermittent flow. When arches become persistent and only an external force can

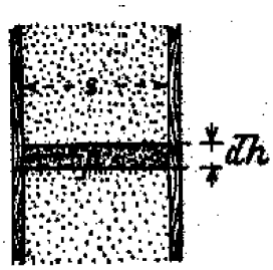

$$p_{s,max}\mu 4sdh = m_s s^2 dh$$
$$p_{s,max} = \frac{m_s s}{4\mu}$$

Figure 1.1: the sketch(on the left) and the formula(on the right) for describing the Janssen effect. The image was taken from [16] with permission.

disrupt them, this phenomenon is known as clogging [19]. The granular dynamics at the orifices is related to the shapes of the orifices. Some shapes of orifices are shown In Fig 1.2. Meanwhile,

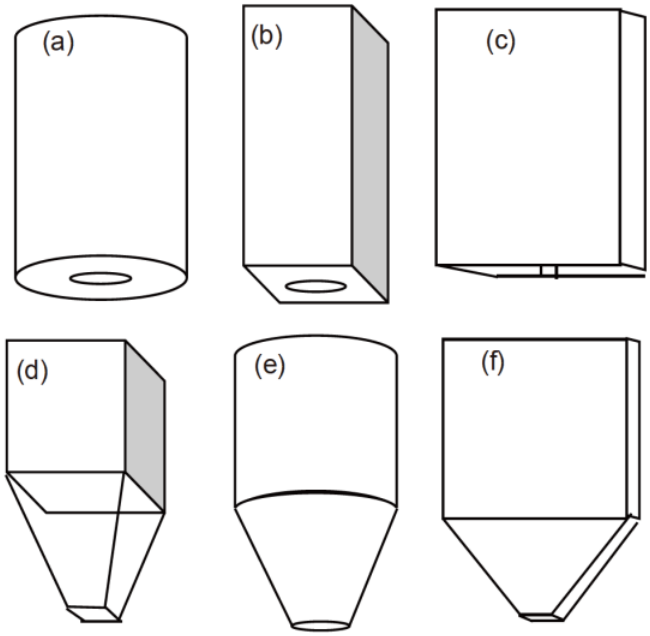

Figure 1.2: examples of typical silos. (a)-(c) silos with flat bottom; (d)-(f) silos with inclined bottom. The figure was taken from [20] with permission.

the shape of orifices and some other physical factors influence the characteristics of granular flow, which will be discussed in detail in the next section.

Based on the geometry and dimension of silos, the Beverloo equation [21] has been raised and widely developed as the standard for describing the flow rate of particles passing through orifices.

$$Q = C\rho\sqrt{g}(D-kd)^{n+\frac{1}{2}} \tag{1.1}$$

Q is the flow rate, ρ is granular bulk density, d is the diameter of particles, $n = 1$ is for quasi-2D silo, and D is correspondingly the width of orifices, $n = 2$ is for 3D silo and D is the diameter of the orifices, C and k are the dimensionless curve-fitting parameters which are related to the shapes of particles. Usually, C is in the range of $0.55 \sim 0.65$ and k is $1 \sim 2$. The free-fall arch model [22] was proposed to physically explain Beverloo equation (equation 1.1): supposing an imaginary stable arch at the orifice, the particles above the arch move very slowly while the particles under the arch freely fall, given by Newton's second law, the velocity v of particles

moving to the orifice in the quasi-2D silo will be $v \propto \sqrt{gD}$, and the relation of flow rate with orifice size is $Q \propto \rho D v$, so $Q \propto \rho \sqrt{g} D^{\frac{3}{2}}$. With the empty annulus hypothesis [22], i. e. in the area of $\frac{d}{2}$ from the outlet borders, the centroids of spherical particles cannot go through so the effective size of the orifice could be $D - kd$, the final form of outflow rate Q comes to $Q \propto \rho \sqrt{g}(D - kd)^{\frac{3}{2}}$.

1.1.2 Shear flow

When talking about dense granular flows, it is related to six geometries shown in Fig 1.3 to achieve shearing the material and measuring rheological properties. These geometries can be categorized into two classes: confined (Fig 1.3(a)-(c)) and free surface flows (Fig 1.3(d)-(f)). In the aim of studying flow rheology, the plane shear geometry (Fig 1.3(a)) is the simple geometry, which configures two rough plates applying the motion to one of the plates, and the Couette cell (Fig 1.3(b)) is another classical geometry, where the material is filled in between two cylinders with annular shear by rotating the inner cylinder. For rigid particles, dimensional analysis

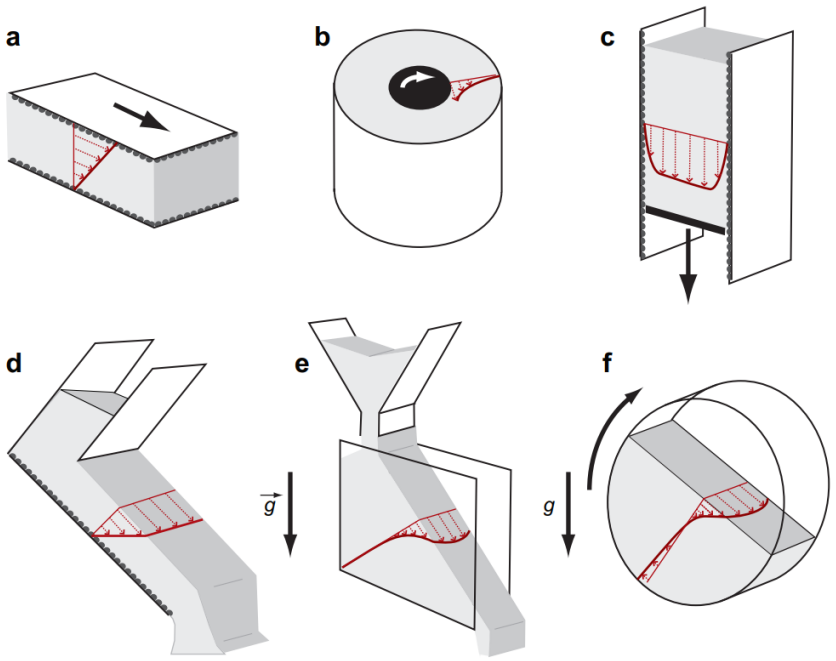

Figure 1.3: different flow configurations: (a) plane shear, (b) Couette cell, (c) silo, (d) flows down an inclined plane, (e) flows on a pile (heap flow), (f)flows in a rotating drum. The figure was taken from [23] with permission.

constrains the stress or shear rate relations. In large systems supposing no boundary effect, the system is controlled by a dimensionless parameter called the inertial number:

$$I = \frac{\dot{\gamma} d}{\sqrt{p/\rho}} \tag{1.2}$$

where $\dot{\gamma}$ is the shear rate, d the mean particle diameter, p the pressure and ρ the bulk density. This parameter can be interpreted in terms of two kinds of time scales [24]: (a) a microscopic time scale $\frac{d}{\sqrt{p/\rho}}$, which represents the time for a particle falling in a hole of size d under the pressure p or which indicates the time scale of rearrangements, (b) a macroscopic time scale $\frac{1}{\dot{\gamma}}$ related to the bulk deformation. Small values of I reflect a quasi-static regime where bulk deformation is slow

compared to microscopic rearrangement, whereas large values of I correspond to rapid flows. By either increasing the shear rate $\dot{\gamma}$ or decreasing the pressure p, it can induce the transition from a quasi-static to an inertial regime. For rigid grains, the shear stress τ is proportional to the pressure p with the effective friction coefficient μ, i. e. $\tau = P\mu(I)$ and the volume fraction Φ being functions of I, i. e. $\Phi = \Phi(I)$ [23]. I of soft particles is different from rigid particles, an elastic time scale should be additionally introduced [25, 26], which is still under discussion.

Moreover, in the regime of slow flows, unlike local rapid flow, the inertial number I tends to zero (e. g. in the range $I < 10^{-3}$), and momentum transfer is dominated by contacts between particles. The averaged stresses and flow profiles become independent of the flow rate in this slow flow regime. Shear bands, localizing near the moving boundary of a container, are usually narrow, which indicates steep strain gradients that are difficult to capture by a continuum theory [27].

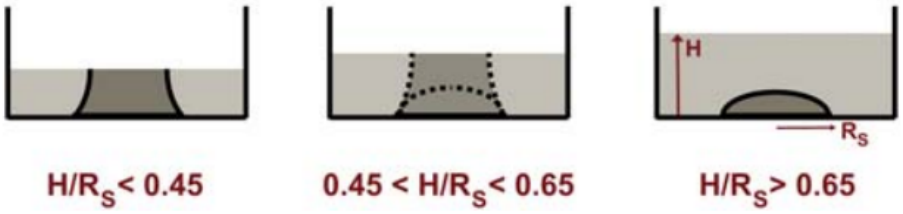

Figure 1.4: the transition in flow structure from shallow to deep flows in the cylindrical split-bottom geometry. In the dark grey region, the material moves together with the disk. The figure was taken from [28] with permission.

Fortunately, split-bottom geometries can generate broad shear bands, which have been extensively examined in numerous experiments, numerical simulations, and theoretical studies. The split-bottom geometry is characterized by three parameters: the radius of the bottom disc R_s, the thickness of the granular bed H, and its rotation angle Ω. As the disc rotates, propelling the flow, the geometry and dimension of the shear zone depend on the ratio $\frac{H}{R_s}$ of the filling height H and the radius R_s of the rotating bottom plate [27, 29–31]. Three regimes can be identified as depicted in Fig 1.4. At low filling height ($H < 0.6R_s$), it was found for rigid, frictional spherical grains that the shear zone traverses the granular bed vertically in its entirety and the inner part of the granular material rotates synchronously with the rotating bottom. As the filling height increases, the shear zone closes in, and at a sufficient height, it forms a closed dome above the bottom disk.

1.2 The effects of physical factors on granular flow in silos

It remains a significant challenge to understand the mechanics of granular flow and establish a relationship between the macroscopic dynamics of granular flow and the microscopic interactions between particles. Therefore, it is significant to characterize granular flow by a wide range of physical factors. Silo flow is the main topic of this thesis. Investigating the impact of physical factors on silo flow contributes valuable insights into understanding granular kinetics, establishing granular constitutive relations, and designing well industrial facilities.

1.2.1 Geometry of the silo

The Beverloo equation (Equation 1.1) can successfully predict the outflow rate for large orifices, but it has some limitations: this equation is just valid for round orifices in 3D silo and rectangular

orifices in 2D silo. The equation ignores interactions with gas flow, however, it cannot well predict the cases of other shapes of orifices such as rectangle outlets and the cases of small orifices. So shapes and sizes of orifices have obvious effects on granular flow in a silo: the characteristics of granular flow through a flat-plate orifice have been investigated [32]. Granular materials are stored in an upper container. The gate opens or shuts down granular flows from the container. Below the gate is a flow controller to feed the tube with an orifice. The orifice with a gauge at the end of the tube is to measure the normal stress of the orifice. When the flow starts to run, the discharge rate increases with normal stress at the silo bottom, once the orifice gets clogged, the discharge rate starts decreasing with further increasing normal stress at the bottom, and then the discharge rate doesn't change with normal stress at the bottom, see Fig 1.5. Similarly, in the study of quasi-2D and 3D silo [33], it found that the negligible kinetic pressure in an arch-like region, where a transition surface of velocities of particles is defined, is scaled by the orifice diameter and located above the orifice. So the pressure in radial directions near orifices is significant to consider designing silo outlets for the safe storage of particles. In another

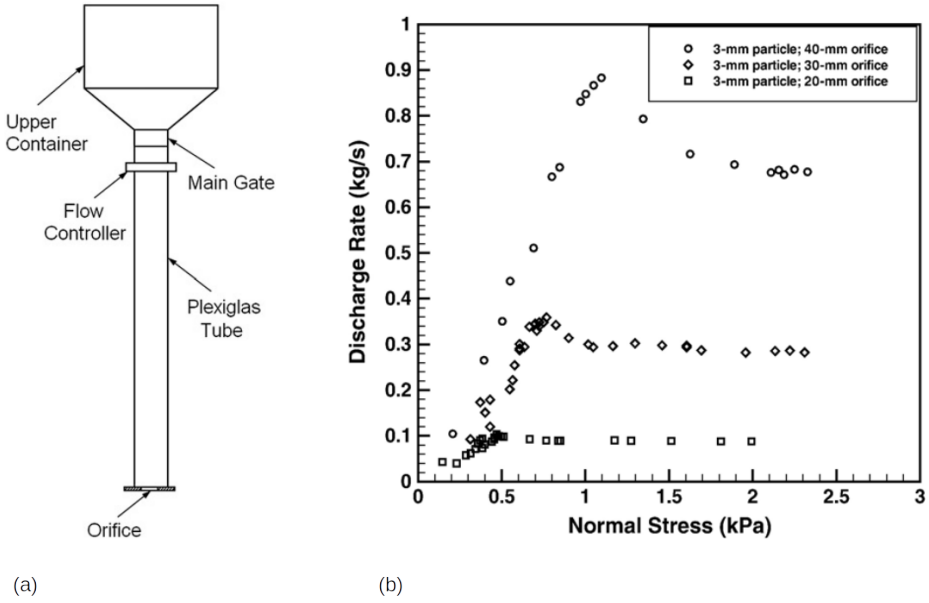

Figure 1.5: (a)scheme of the experimental setup; (b)discharge rate as a function of normal stress on the orifice plate for 3mm glass particles with various orifice sizes. The figure was taken from [32] with permission.

study of a quasi-2D silo [34], the distributions in the radial direction of granular velocity and granular packing fraction are measured, and they show correlations with the granular velocity: as usual, the velocity profile at the orifice can be written as $v(x) = \sqrt{2gR}\sqrt{1-(\frac{x}{R})^2}$ considering particles fall only by gravity, see in Fig 1.6. Correspondingly, the density profiles can be fitted by using a fractional power of dimensionless radius $(1-(\frac{x}{R})^2)^{\frac{1}{\mu}}$. Additionally, there is a critical size of orifice A_c ($A_c \approx 4.5D$) [35], when $A > A_c$, the outflow rate with little fluctuation following a Gaussian distribution, when $A < A_c$, cloggings would happen and the transient flow rates are with large fluctuation, see in Fig 1.7. In a study [12] of granular flows in a 2D channel placed on an inclined plate, granular flows in the test section ($D \times l$ shown in Fig 1.8(a)) are initiated by allowing the steel beads in the hopper to fall by gravity. The relation of the flow rate in transition with the outlet size was proposed: at a given inclined angle and a given inflow rate, there is a

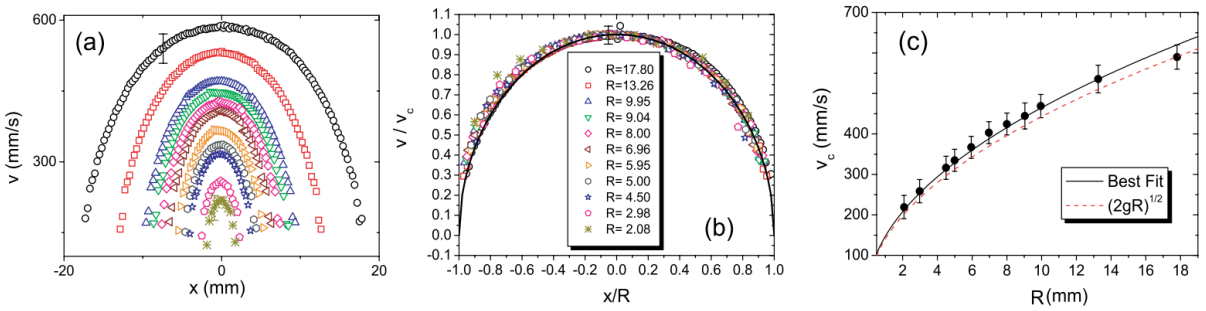

Figure 1.6: (a) Velocity profiles for different outlet sizes (labels are in the (b) panel); (b) normalized velocities and the black continuous line is a scaling function of velocity; (c) the velocity in the outlet center as a function of R of the outlet. The solid line is the best fitting and the dotted $v_c = \sqrt{2gR}$. The figure was taken from [34] with permission.

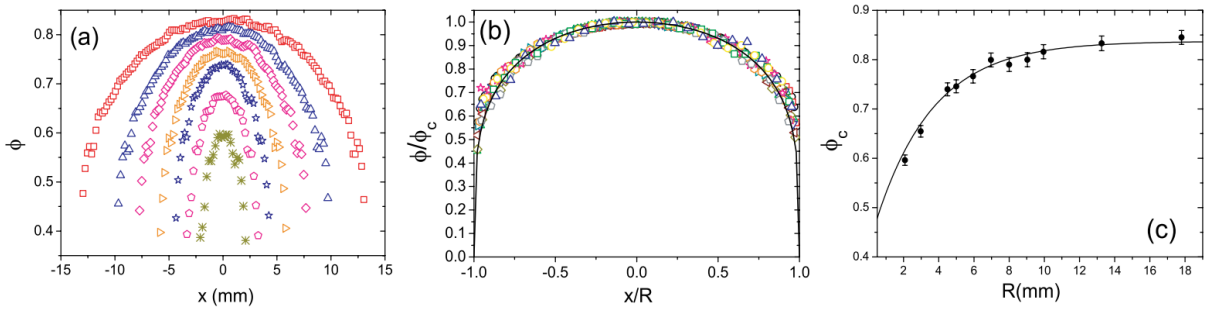

Figure 1.7: (a) Density profiles for different outlet sizes (b) Collapsed profiles of the data displayed in fig(a). The symbols are the same as in Fig 1.6 and the continuous line is the scaling function introduced in the text. (c) Dependence of the volume fraction in the center of the orifice with R. The solid line is the fitting function explained in the text. The figure was taken from [34] with permission.

critical size of outlet d_c resulting in a sudden decrease of the outflow rate as shown in Fig 1.8(b), which made the flow transit from dilute flow to dense flow. In a simulation study [13] of 2D granular flow in a channel with a small exit, the authors obtained a relationship between the local flow rate and the local packing fraction as shown in Fig 1.9, according to this result, four flow states, i. e. stable dilute flow, metastable dilute flow, unstable dense flow, and stable dense flow, are described at a given inflow rate according to this result.

1.2.2 Properties of particles

The properties of particles, such as the friction of particles, shapes of particles, or the elasticity of particles, etc, play an important role in silo discharge. Studies on the effect of friction are mainly from simulations. In MD simulations of quasi-2D silos [36], it was found that the outflow rate decreases with the increase of the coefficient of friction between particles. In another study [37] of discharging particles in a submersed silo with liquid and a drained silo without liquid, the outflow rate in the submersed cases decreases during the discharge, similar to the behavior of the Newtonian fluid. Conversely, in dry and rough granular scenarios, the outflow rate remains constant. In DEM simulations of a 3D conical hopper [38], the flow pattern changes from mass flow to funnel flow with the increase of the coefficient of static friction of particle-wall. The static friction of the particle wall also influences the velocity distribution at the wall. In other DEM simulations of two-dimensional and three-dimensional hoppers [39], it was shown that the wall frictions influenced force chain lengths and volume fractions (the statistical properties of

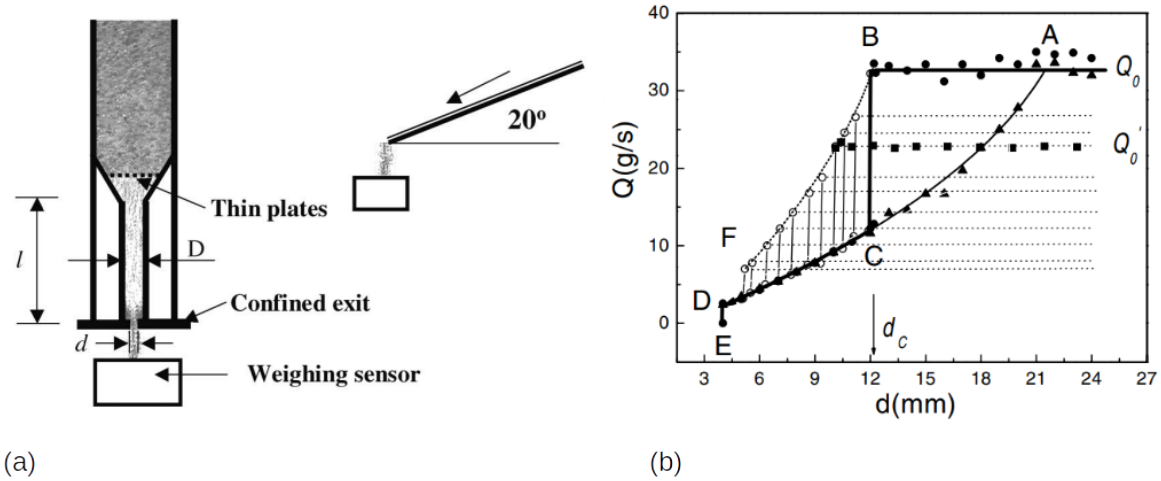

Figure 1.8: (a) Top and side views of the inclined channel. (b) A transition from dilute to dense occurs at a critical opening size d_c, and the outflow follows curve *ABCDE*. For a dense flow, as d increases the flow follows curve *DC* and is extended to *A* with no abrupt change. For different Q_0 (given inflow rate), the transition occurs at different d, as shown by dashed lines. The curve *BF* determines the optimal outflow rate at any given Q_0. The figure referred to was taken from [12] with permission.

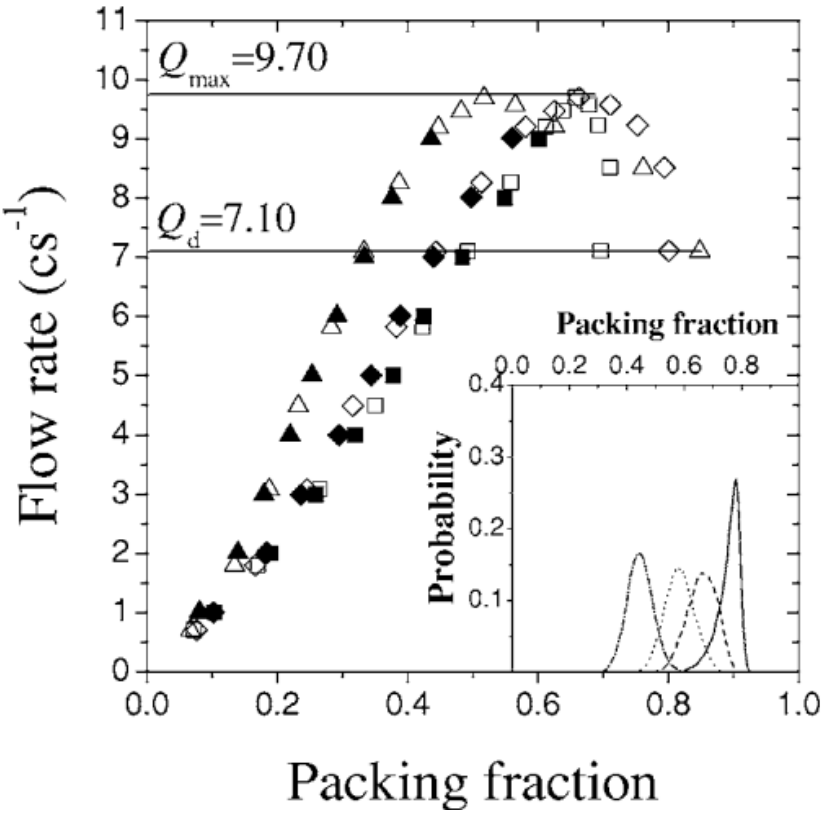

Figure 1.9: The relationship between flow rate and packing fraction. Q_{max} and Q_d are respectively the maximum flow rate and the flow rate of a stable dense flow state. The figure was taken from [13] with permission.

granular flows). In a study of the two-dimensional granular flow on an incline [40] shown in Fig

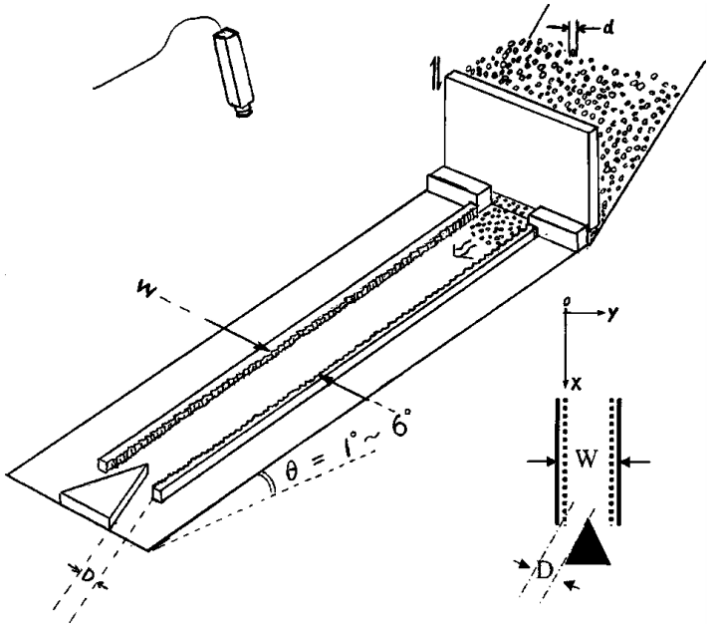

Figure 1.10: The inclined channel and the definition of the geometrical parameters W and D. The figure was taken from [40] with permission.

1.10, the granular density distribution is sensitive to the roughness of the wall in an oscillatory dilute-dense flow regime. The collision resistance at the boundary causes the dense areas to decelerate. The high dissipation of collision may bring spheres into long-duration contacts, which leads to temporary arching or rolling beads into a stagnant cluster sliding against the bottom plate.

Actually in nature and industry, specifically in segregation processing, it is common that the granular flow consists of a mixture of particles. It is more complex to study the flow of mixtures compared with the homogeneous granular flow, especially considering the factors, such as components of mixtures and size ratios of different particles in mixtures that may have important effects on the bulk density. In the study [41] of binary granular mixture in a flat-bottom 3D silo, it is discussed that the bulk volume fraction could be affected by the mass concentration χ_f of fine particles in binary mixtures. In another studies [42, 43] of mixtures of fine and coarse particles with equal density in cylindrical and conical hoppers, a semi-empirical model was proposed to determine static and flowing bulk densities of the mixtures by the mass concentration of fine particles and the size ratio. The model indicates a coarse-particle-dominated or fine-particle-dominated flow field explaining the segregation behavior.

In the research of transportation in silos like drug delivery, the shape of particles plays an important role in silo flow. The alignment of contacting ellipse particles enhances the probability of forming stable arches because of structural force chains [44, 45] and further decreases the flow rate and forms clogging. Among the researches, one study [46] experimentally and numerically discussed the morphological and mechanical properties of non-spherical, convex particles in a silo. The shapes of grains have a profound effect on the morphology in the arrangement and the way of stress propagation. In another study [47, 48], ellipsoidal particles are used in DEM simulations to investigate the shape effect on the granular flow in a cylindrical hopper, spheres with unified aspect ratio have the highest flow rate but ellipses with the lower or higher aspect ratio have lower flow rates.

Furthermore, the elastic behavior of particles has been studied for the last decades but to a low extent, which is mostly for modeling calibration. The elasticity of particles is essential for discrete element modeling (DEM) which is used to investigate the granular dynamics by simulation. The contact theory and continuum mechanics are developed to describe the contact between particles. To consider the elastic part of a contact, which needs to be calibrated for soft particles in the contact model of the simulation, either the contact stiffness, Young's modulus, or shear modulus is introduced in the contact model. The contact stiffness k_n reflects the particle overlap and resulting normal force. Young's modulus E and shear modulus G are dependent on each other through the Poisson ratio ν:

$$E = 2G(1+\nu) \tag{1.3}$$

In a study [49] of soft particles discharged from a silo with a flat bottom, the soft particles were simulated with Young's modulus of 70MPa and the hard particles with Young's modulus of 70GPa. It was found that the system of soft particles discharged faster. This was explained by less strong interaction between the particles due to higher deformation and greater energy dissipation. It was also found that a minor reduced Young's modulus of soft particles didn't influence the discharge rate but strongly affected the contact forces. Elastic particles are good models for biological cells to exploit granular dynamics in biology. Different constitutive equations are employed to model the mechanical behavior of deformable particles. There are three elastic constitutive equations considered in the literature, namely the Hookean, neo-Hookean, and Gent models. Hooke's law states a linear relationship between stress and strain. The neo-Hooke model [50] predicts a nonlinear relation between stress and strain at high deformation while it is similar to Hooke's law at low deformation. Further, the Gent model is another hyper-elastic model and includes material stiffening at large deformation. Apart from the theoretical prediction, some experiments are studied for contact model calibrations. They focus on the deformation of an individual elastic particle in a liquid flow [51–53]. The dynamics of an individual particle are related to shape-changing, particularly involving the particle's surface in response to the liquid flow. However, the behavior of a collection of elastic particles has not been calibrated widely, which would be useful to provide proof for the corresponding constitutive relations of elastic particles. It would be an interesting topic and show different dynamics from inelastic particles like sand or beads based on the previous studies of individual soft particle mechanics. So the flow of elastic, low-frictional particles will be the focus of this thesis, and the flow characteristics, such as flow rate, bulk density, pressure, etc., will be studied in the following chapters.

1.2.3 External factors

To prevent clogging during silo discharge, one method is to vibrate the silo. In the investigation [54] of the discharge of granular materials from a silo with vertical sinusoidal oscillations by experiments and DEM simulations, it was found that the flow rate went down with vibrating acceleration increasing when the frequency of vibration is lower than $50Hz$ as shown in Fig 1.11, which was explained by a decrease of the bulk density of granular materials when the vibration is applied. In another study [55] of a packed granular column with rotational shear discharging, it was concluded that the flow rate increased in response to the applied shear as shown in Fig 1.12. It was also found that the flow rate under shearing is independent of the particle diameter, inter-grain friction, and shearing geometries. In the study [56] of a quasi-2D hopper placed on a vibrating inclined plane, the granular flow on the inclined plane could simulate different traffic flows, and increasing the angle θ of the plane in granular flow can be interpreted as increasing the driving force of the social force model. The granular flow would be intermittent flow with

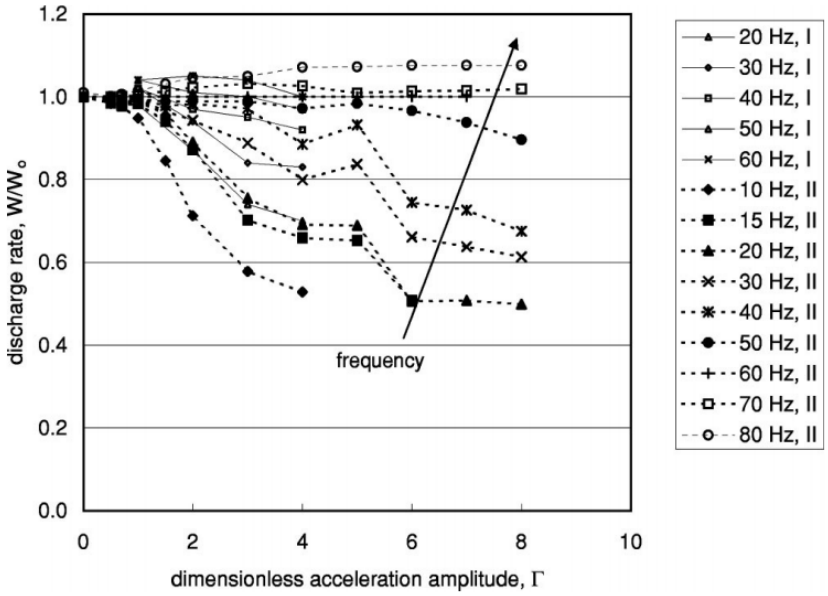

Figure 1.11: The ratio of the mass discharge rate from an oscillating hopper W divided by the mass discharge rate from a non-vibrating hopper W_0, plotted as a function of the dimensionless oscillation acceleration amplitude $\Gamma = a\omega^2/g$. The figure was taken from [54] with permission.

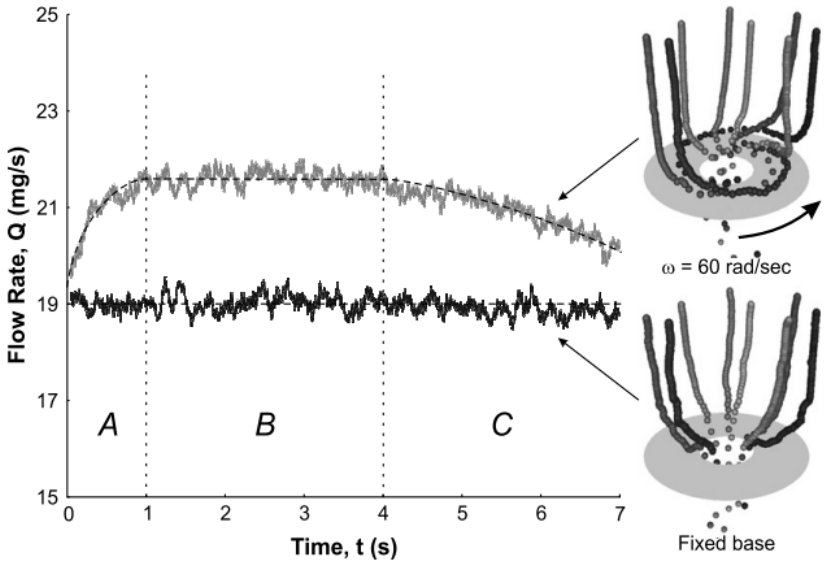

Figure 1.12: Discharge flow rate against time (left) and particle trajectories during discharge (right) for flat-based setup, comparing a stationary base and a base with angular rotation speed $\omega = 60$rad/s. The figure was taken from [55] with permission.

small outlets, and if increasing the angle of the plane in this situation, the outflow rate slows down, which performs the "Faster is Slower" effect. However, in the context of continuous granular flow through large outlets, when increasing the angle of the plane, the outflow rate correspondingly increases, demonstrating the "Faster is Faster" effect.

In another study [57] of a quasi-2D silo with an obstacle above the outlet, where the obstacle can be seen as an external object to influence the flow. It is found that the clogging probability of granular matter is lowest when the obstacle is placed four times of particle diameter away from the orifice, which is explained by the simulation that the presence of the obstacle reduces the pressure and further loosens the packing of particles above the orifice. In the next study [58] of

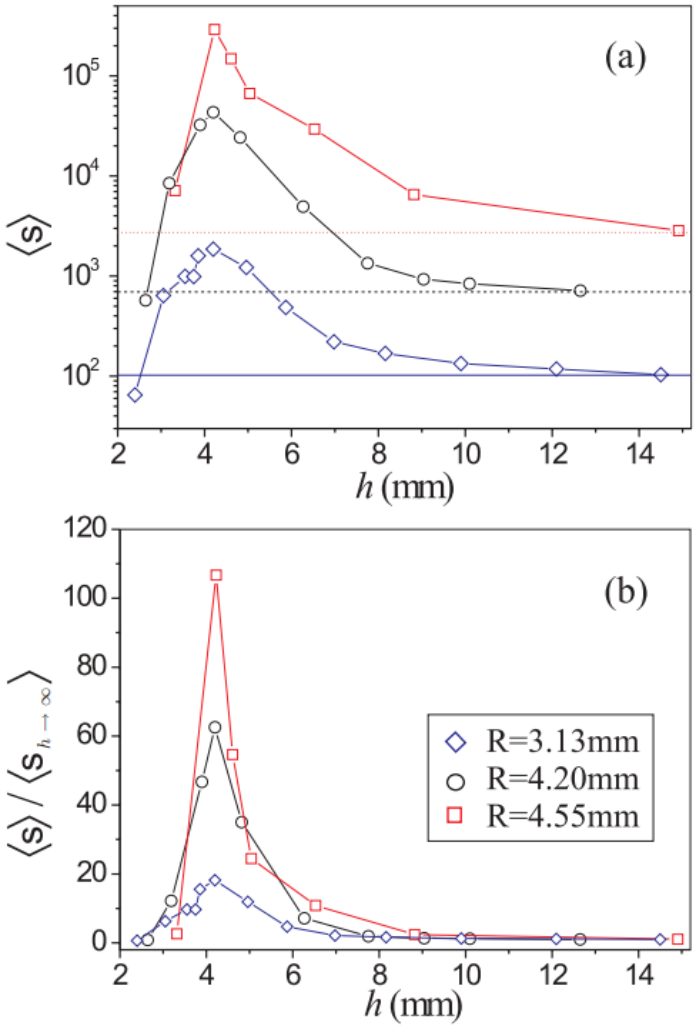

Figure 1.13: (a) Mean avalanche size vs obstacle height h for orifice sizes R=3.13mm, R=4.20mm, and R=4.55mm. (b) The same data as in subfigure(a), but the mean avalanche size $\langle s \rangle$ is divided by the mean avalanche size at $h \to \infty$ corresponding to each value of R The figure was taken from [58] with permission.

the obstacle effect, it was found that for large orifice (R = 4.55mm) of 2D-silo, no matter where the obstacle is placed, it cannot help to speed up the flow rate. In another simulation study [59] of the granular flow across a bottleneck, the results support that the flow rate increases if an obstacle is optimally placed in front of the outlet. it was found that the peak flow rate corresponds to a transition from free flow to congested flow, similar to the phase transition in traffic flow.

1.3 A short guide of the thesis

This thesis is organized as follows:

- Based on the **Introduction** about the two types of granular flow and the effects of physical factors on granular flows, the following chapters will be presented in the perspective of these topics about the dynamics of soft, elastic, and low-friction particles.
- **Chapter 2** investigates the basic but unique characteristics of soft, nearly frictionless granular flow in silos passing through narrow orifices.
- **Chapter 3** is to continue characterizing soft, frictionless granular flow. In this chapter, a few rigid particles with roughness are introduced into the system. We aim to investigate these mixtures and discern whether the frictional properties of the granular systems play a pivotal role in influencing the pressure-dependent outflow rate within soft granular systems.
- **Chapter 4** studies the effect of the obstacle on the silo discharge of soft granular material. From the **Introduction**, it is learned that the pressure changes above the orifices because of the presence of obstacles in front of the orifices in the silo flow and it helps granular flow transform from intermittent flow to continuous flow. Since it has been known that the outflow rate of a soft granular system is pressure-dependent, the effect of obstacles would be peculiar and critical to improving the description of soft granular flow.
- **Chapter 5** casts the perspective on the shear flow of soft particles. This work is only about methodology and the beginning of the shear flow study. MRI technology was applied in this study. We used $CuSO_4$ with water instead of pure water for MRI to mark objects. We successfully detected the marked particles and observed the shear zone with the MRI technology.
- **Chapter 6** contains the summary and outlook for this thesis. The thesis brings a lot of interest to continue the investigations on soft hydrogel particles.

2 Intermittent flow and transient congestion in a quasi-2D silo

Granular materials stored in containers have been in use for decades. One of the early scientific studies describes the pressure conditions in granular beds within vertical cylinders, it observes that the flow of grains is pressure independent [60]. Another finding predicts the pressure at the bottom of silos changes with increasing fill levels from the study of wheat-filled silos. On the other hand, the dynamics of hard particles discharging from silos is described in many researches [21,61–64]: the grains flow freely when the orifice size is sufficiently large (about five times of particle diameter or more); with smaller orifice sizes, the discharge rate decreases continuously, the outflow rate is independent of filling height of containers and the pressure at the container bottom. In some other studies, it is shown that non-adhesive colloidal particles in suspension flow across constrictions in a similar way to dry non-cohesive granular materials [65,66]. Otherwise, some differences arise in the silo discharge of soft materials from hard grains. The low-friction soft grains hardly clog, even when the orifice size is slightly more than twice the particle diameter [67,68]. Secondly, the low friction coefficient of hydrogel particles leads to the feature of hydrostatic pressure, at least when the filling height is up to about 100 particle diameters. The pressure in the quasi-2D hopper is linearly related to the filling height [68].

In this chapter, We load the quasi-2D silo with hydrogel particles and investigate the flow of soft, low-friction grains through small orifices and discuss non-permanent congestions at the outlet. Hydrogel spheres serve as elastic solids which are incompressible and moderately deformed with the elastic modulus of the order of 10kPa to 100kPa [67–70]. We also filled it with hard particles for comparison.

2.1 Experimental setup

The setup consists of a flat box of 80 cm in height and 40 cm in width, slightly thicker than the diameter of the particles (6.5mm), with a flexible slider for adjusting the size of the orifice in the center of the bottom plate [69]. A front view is shown in Fig 2.1. As shown in Fig 2.1, the side edges are hidden by 3cm wide aluminum bars carrying the front and rear glass plates, so that the optically accessible area in the frames is 34cm wide. Two symmetric sliders at the bottom are applied to fix the orifice width W. They are in the shape of a right-angled trapezoid. Our quasi-2D silo can contain around 9500 grains with a total weight of around 1.75kg when we fill the silo up to the height of 80cm. But in this experiment, the initial filling height is around 60cm.

Hydrogel spheres (HGS is used in the following context) are from a commercial supplier (*Happy Store, Nanjing*, shown in Fig2.2a) in dry form. They are immersed for at least 24 hours in 3.8g/L NaCL solution to swell into a bigger diameter of 6.5mm. What we used in the experiment is monosized HGS particles with 6.5mm diameter, varying by approximately 3 %. The friction coefficient is very low, of in the order of 0.01 or even lower (partially depending on wetness on the surface). The elastic modulus is about 50kPa (Note that HGS particles in the experiment are slightly softer in the outer shell layers than in their cores). The elastic modulus is measured by contact diameters of the Hertz contact model displayed by pressing particles under given weights.

The discharge is recorded with a commercial motion video camera (*XiaoYi 4K+ Action*

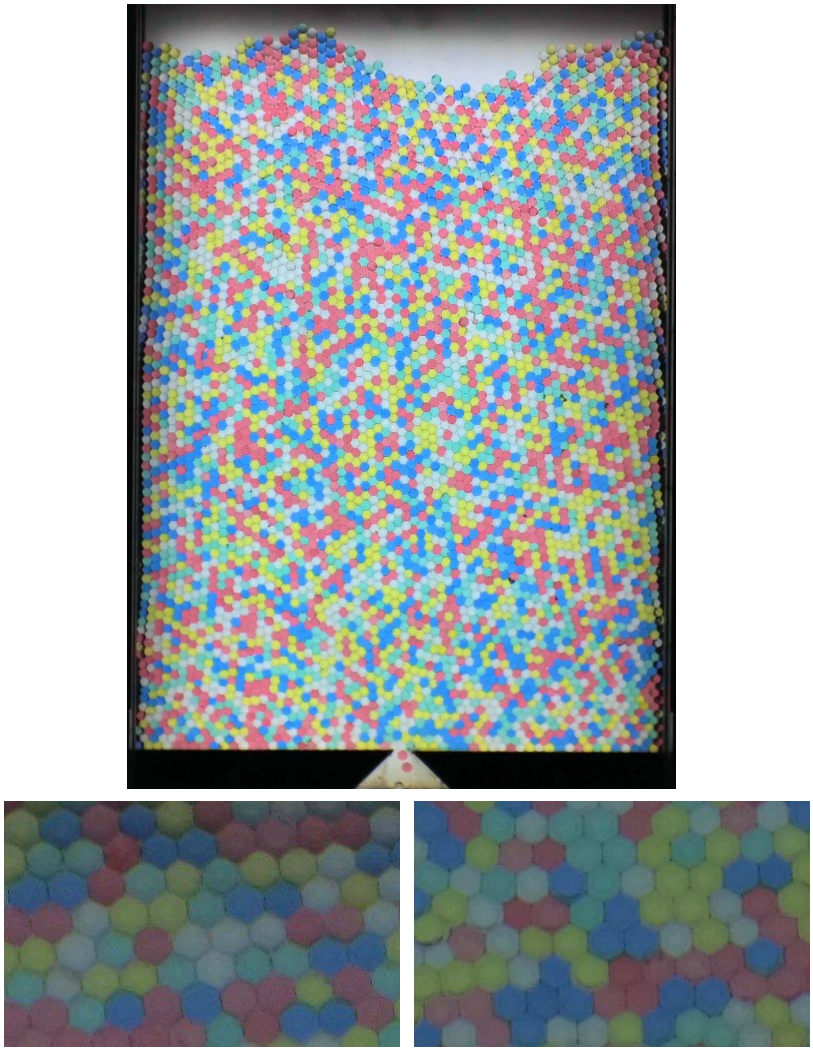

Figure 2.1: Image of the 2D silo filled with 6.5mm HGS particles, snapshot during discharge (33s after initiation). Grains with different colors are equivalent. Colors are only used to trace individual grains to monitor flow processes. The bottom images show expanded details of regions 1cm below the upper layer (left) and 1 cm above the bottom (right). The orifice width is 12mm. The image is reproduced from [71].

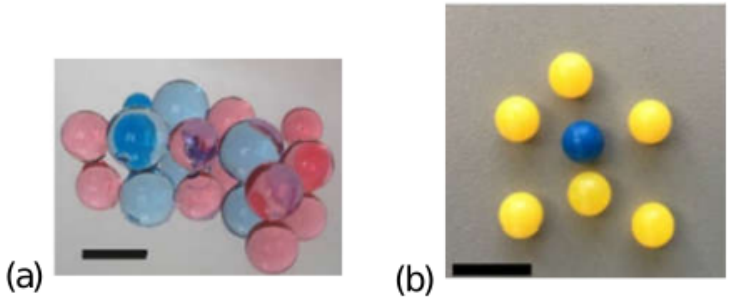

Figure 2.2: (a) Hydrogel spheres after swelling in salty water for more than 24 hours, with final diameter $d \approx 6.5$mm. (b) Airsoft bullets with diameter $d = 6$mm.

Camera), and videos are taken with a frame rate of 60fps. Each frame of videos has a spatial resolution of 0.327mm/pixel. Below the orifice, the flowing-out particles are collected in a box placed on a balance. HGS grains are taken from the storage bath, then placed on tissue to remove the excess water on the particles' surface (in practicality, complete removal of water from the surface is not achievable), and poured into the silo from above, while the orifice is closed. After filling the silo to a certain height (on average 60 cm in our experiments), the orifice is opened and we measure at the same time the weight of the discharged material and record the video of the silo from the front side. Video and mass measurements can be synchronized better than 0.5s.

To describe the differences between the soft, low friction grains and hard frictional particles of comparable size (diameter of approximately 6 mm) and similar density, we have performed some other experiments with hard plastic ammunition (Airsoft bullets, ASB, shown in Fig 2.2(b)) for comparison. The friction coefficient of ASB is approximately 0.3. The deformation of ASB is too small in collisions during discharge. So it can be assumed that the deformation of ASB can be neglected.

The experiments in this study are listed in Table 2.1. Free flow means uninterrupted discharge where the flow rate is either constant or decreases with decreasing filling height. Fluctuating flow means randomly varying flow rates. Intermittent flow is characterized by phases where flow is completely interrupted. There is no clear distinction between intermittent and fluctuating flow. Based on empirical observations, we establish a threshold time beyond which it becomes difficult to perceive with the naked eye whether a particle is flowing out when it blocks the orifice.

Material	Orifice D	D/d	Character of discharge
ASB	34 mm	5.7	free flow
HGS	18 mm	2.77	free flow
HGS	15 mm	2.30	free flow
HGS	12 mm	1.85	fluctuating flow, $h_c \approx 4$ cm
HGS	11 mm	1.69	intermittent flow, $h_c \approx 11$ cm
HGS	10 mm	1.55	intermittent flow, $h_c \approx 23$ cm

Table 2.1: Materials, orifice sizes, and the character of discharge. D/d is the ratio of orifice width (the gap between the upper edge of the two sliders, see Fig 2.1) and particle diameters. In cases where the system clogs permanently, h_c is the average remaining height.

2.2 Results and analysis

2.2.1 Flow inside the silo

The structure of the flow field is visualized by averaging subsequent images in the recorded videos. Fig 2.3 shows averaged flow fields of superimposing 1000 frames of ASB and HGS individually. In the case of ASB, there is a pronounced flow along the trigonal lattice planes, ray-like lines. Two stagnant zones are identified by their stationary hexagonal lattices. However, in the case of HGS, the flow is slower in the corners, but there is no stagnant zone. From another perspective, it can be observed that the local packing fraction changes considerably after the start of flows when the silo is filled with HGS. In the silo filled with hard grains, the local packing fraction changes only in the sheared regions near the edges of the flowing zone and in the area directly above the orifice.

Fig 2.4 shows the space-time plot of consistent vertical cuts along the central vertical symmetry axis of the silo and the orifice. As shown in Fig 2.4(a) about the case of ASB, the positions of all

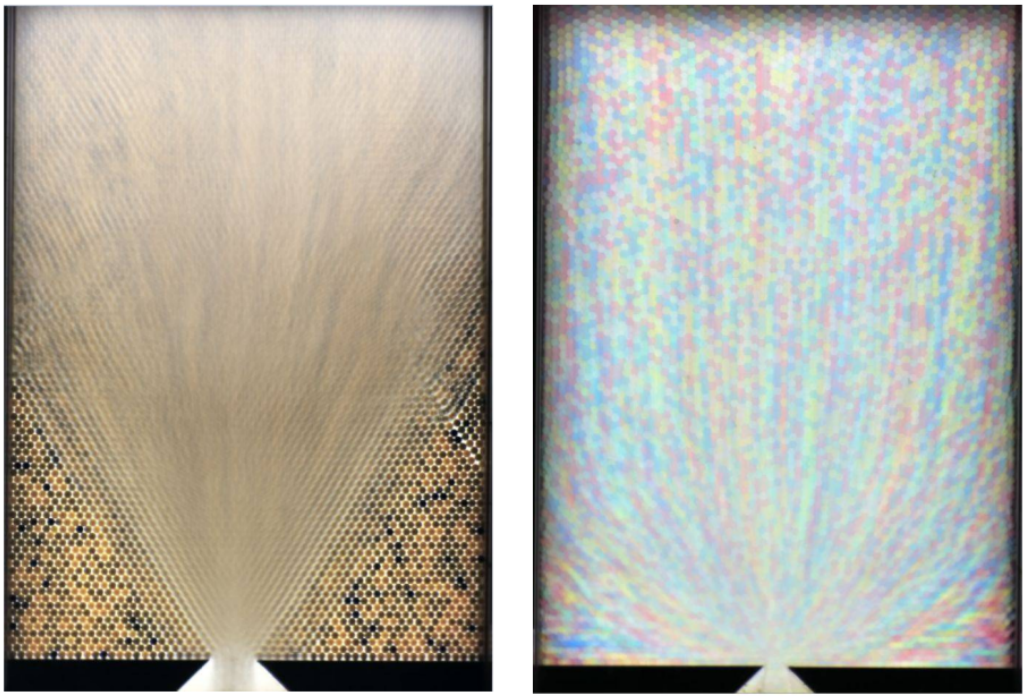

Figure 2.3: Superimposed 1000 images ($\approx$ 16s) of the 2D silo filled with (a) 6mm ASB and (b) 6.5mm HGS particles during the discharge. The orifice size is 34mm for the ASB, and 18 mm for the HGS. The image is reproduced from [71].

grains stacked along this direction start to move down immediately after the orifice is opened, shown in Fig 2.4 at time zero. Fig 2.4(b)-(d) shows the cases of soft, low-friction grains. The flow initially starts near the orifice, while the positions of the upper grains remain unchanged. The front of the flowing material rises at a speed of approximately 10cm/s. After some amount of material has flown out, in our experiments roughly 150g or 1000 spheres, the silo has sufficiently diluted and the filling height has reached 50cm (the upper edge of the frames). Then, the HGS spheres move down synchronously along the central axis. The downward flow accelerates within 10cm above the orifice, where the flow rate is lower at the sides.

2.2.2 Outflow rate and fluctuation

In this part, we will discuss the differences in the outflow rate and fluctuation between hard and soft grains. Fig 2.5 shows the outflow rate changing with the time of ASB (orifice size = 34mm, in Fig 2.5(a)) and HGS (orifice size = 18mm, 10mm, in Fig 2.5(b)-(c)). When the silo contains hard grains, the outflow rate decelerates as the silo approaches near-empty conditions; otherwise, the outflow rate remains relatively consistent. The stagnant zones gradually diminish from the top until they reach the static angle of repose. The stagnant zones erode from the top until the static angle of repose is reached. For smaller orifice sizes, the same features are found, but smaller orifice sizes lead to persistent clogs that prevent further flow. When the silo with a large orifice is filled with HGS (shown in Fig 2.5(b)), the situation is similar to hard grains at the beginning after opening the orifice. When the orifice is approximately 3 times of particle diameter wide, there is still continuous outflow. But later the outflow rate becomes dependent on the pressure. This becomes more evident with smaller orifice size at 10mm as shown in Fig

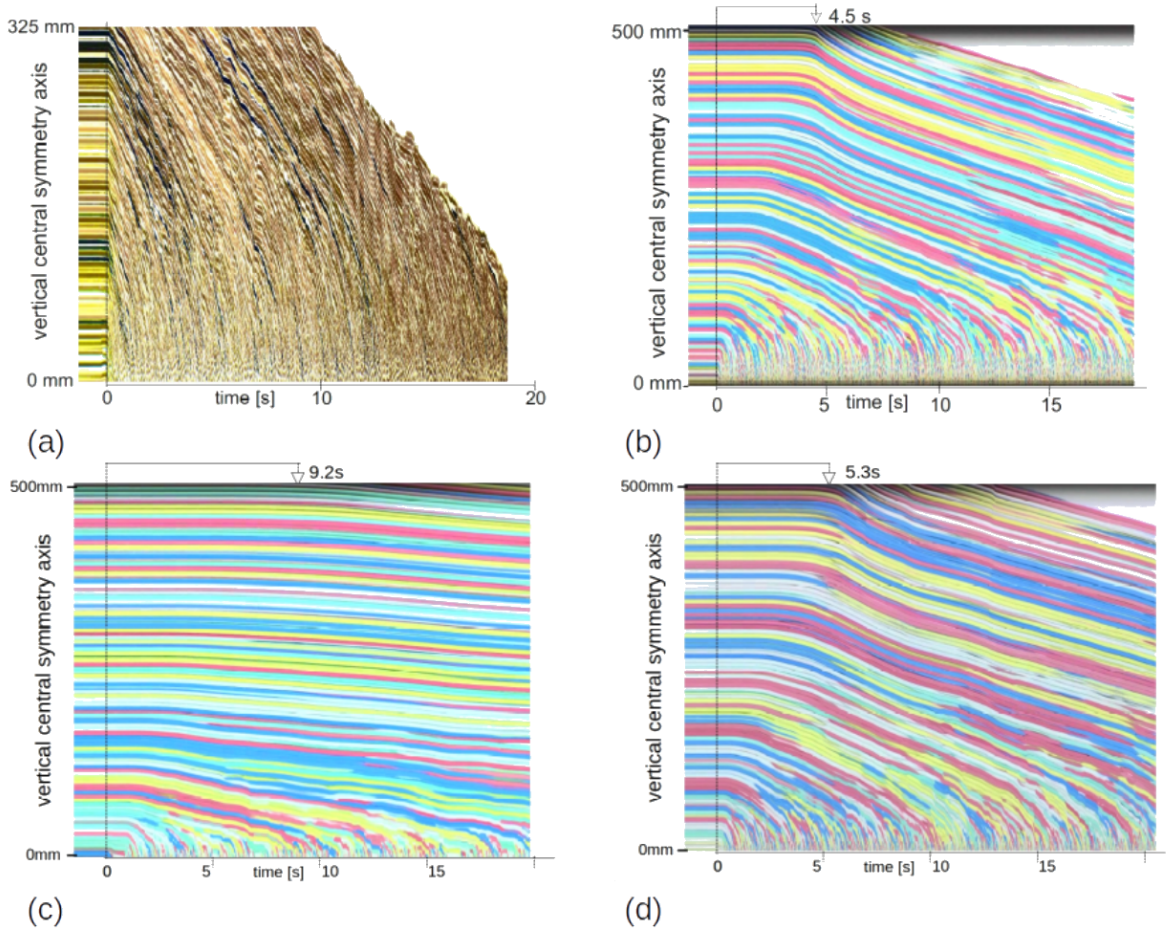

Figure 2.4: Space-time plots of a vertical cut at the central symmetry axis of the silo, (a) ASB, 34mm orifice width, (b) HGS, 18mm orifice width, (c) HGS, 11mm orifice width, (d) HGS, 15mm orifice width. In the hard particle system, the flow reaches the upper edge of the selected region within approximately 100ms. In the soft material, it takes 4.5s after the orifice was opened for the flow to reach the upper region shown in the plot. This is even more pronounced at lower orifice widths because of the lower flow rates. The image of (a) and (b) is reproduced from [71].

2.5(c). The outflow starts to fluctuate. Not only does the initial flow rate respective to 18 mm orifice size reduce by one order of magnitude shown in Fig 2.5(b), but the discharge curve also shows plateaus where the outflow stops for several seconds.

The details from the same data as in Fig 2.5 are shown in Fig 2.6. The discharge rate of hard grains (Fig 2.5(a)) is linear of time changing. Small platforms in the curves are artifacts of the measurement technique, resulting from the time resolution of recording of the balance: the balance is set to update its value every 0.214s, while the computer samples this data every 0.1s, thus every data from the balance is regularly read out twice. The 18mm orifice curve (Fig 2.5(b)) is straight and smooth regardless of the artifact of reading data.

Fig 2.7 illustrates the variation in outflow rates depending on the remaining filling height, as demonstrated in Fig 2.5-2.6 during discharges, provides evidence that the primary determinant of the outflow rate is the pressure at the bottom of the container. To smoothen these data, we averaged them over the period when the filling height dropped by 5cm. The surface of the flowing granular bed is v-shaped instead of flat, we calculate the mean height from the same volume in the silo during discharge. The arrows in the figure indicate where the tip of v has

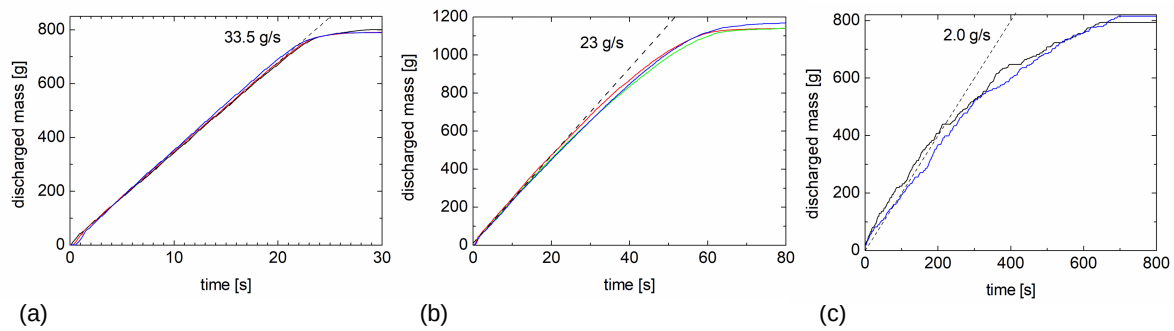

Figure 2.5: Discharged mass (a) in the ASB-filled silo with 34mm orifice width, $D/d = 5.7$, (b) in the HGS-filled silo with 18mm orifice width, $D/d = 2.77$, and (c) in the HGS-filled silo with 10mm orifice width, $D/d = 1.55$. Apart from the very different time scales caused by the different orifice widths, it is evident that the flow of the hard ASB grains is practically constant until the very bottom of the silo is reached. In the HGS-filled silo of the 18mm orifice, the discharge slows down with a sinking fill level. This is even more pronounced in the 10mm orifice silo where strong flow rate fluctuations occur even when the silo is still well-filled. Different colors distinguish individual runs of the experiment. The image is reproduced from [71].

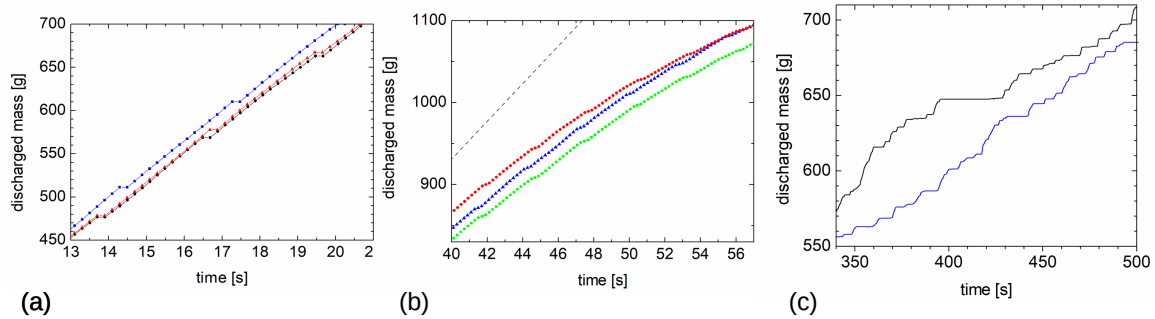

Figure 2.6: Zoomed-in details of the three graphs shown in Fig 2.5(a)-(c). All graphs show periods ending approximately 100g before the discharge stops (empty silos in (a) and (b), the permanent clog in (c)). The small step-like undulations in graphs (a,b) are a beating artifact of the sampling frequency of the balance (4.66 Hz) and the poll frequency of the computer (10 Hz). Note the different scales of time axes. The image is reproduced from [71].

reached the orifice and the granular bed splits into two parts on the left and right side, from which particles slide down. It can be seen that all outflow rates are strongly dependent on filling levels. For narrow orifices, the outflow rates sensitively depend on the different situations of the samples. For instance, despite drying the HGS surfaces with tissue before introducing them into the silo, fluctuations in moisture on the HGS surfaces could potentially impact the cohesion of spheres through capillary bridges, thereby potentially influencing the magnitude of the outflow rate.

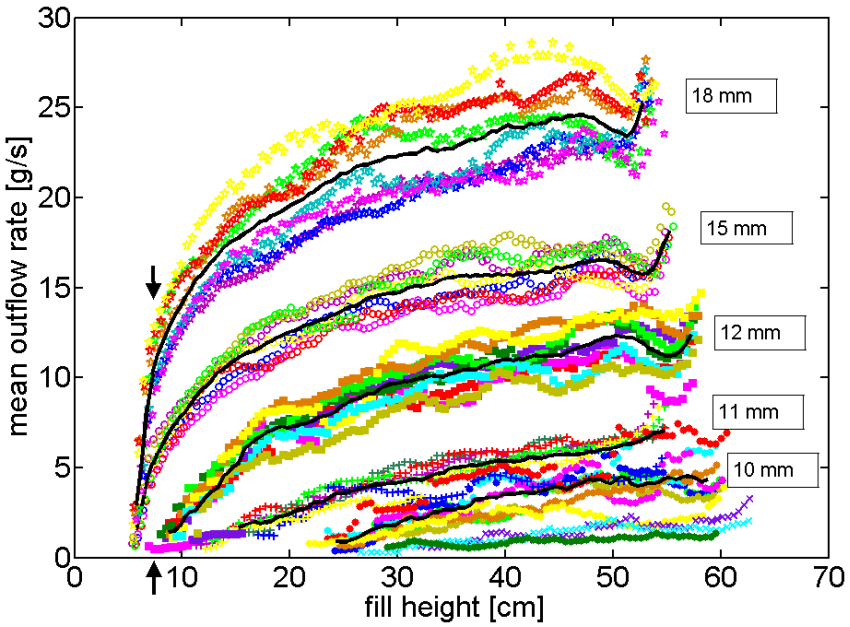

Figure 2.7: Mean outflow rates of HGS for different orifice sizes as a function of the instantaneous fill level. All rates are averaged over a 5cm height difference. The solid curves represent the averages of curves belonging to one set of experiments at fixed orifice sizes. Arrows indicate where the tip of the v-shaped surface of the granular bed reaches the outlet. The image is reproduced from [71].

Next, we analyze the temporal fluctuations of the outflow. To be mentioned, Kirsten Harth, one of the co-authors from this published paper [71], contributed Fig 2.8 and 2.9 in the parts of temporal fluctuations and non-permanent congestion. The variations in the outflow rate can be characterized by the Fourier transform of the discharge rates, obtained from balance data. We set the scanning window at a low-frequency range below 0.6Hz, ensuring that artifacts from the balance at 2/3Hz are omitted from the observed frequency range. Fig 2.8 shows four different frequency spectra. All spectra are normalized with the corresponding maximum Fourier amplitude A_{max} at zero frequency and clipped the low-frequency part of the spectrum at $0.1A_{max}$. At 15mm orifice (Fig 2.8(a)), we can see slight fluctuations with amplitudes of around $0.04A_{max}$, at orifice 12mm (Fig 2.8(b)), the fluctuation becomes more pronounced as the discharge progresses towards the end of discharge. However, at the 11mm orifice, the fluctuation is with the amplitude of $0.1A_{max}$, even at the beginning of the discharge. In the case of the smallest orifice of 10mm in our measurements (Fig 2.8(d)), the amplitude of fluctuations reaches more than $0.4A_{max}$, and some interruptions extend over the full width of the scanning window longer than 15s.

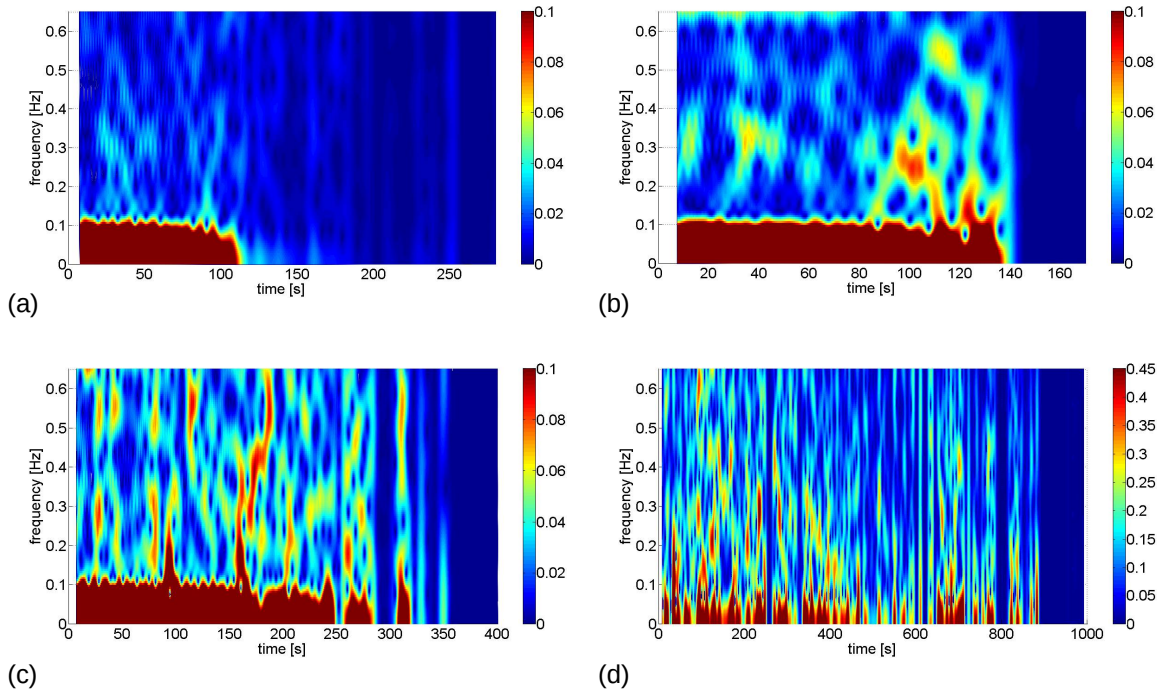

Figure 2.8: Windowed Fourier Transforms (Hamming window width 15s) of the HGS outflow rates for different orifice sizes, (a) 15mm, (b) 12mm, (c) 11mm, and (d) 10mm. The peaks are scaled with the maximum Fourier amplitude $A_{\max}$ and clipped at $0.1A_{\max}$. Note the different color scales on the right hand in each group figure. The image is reproduced from [71].

2.2.3 Non-permanent congestions

Fig 2.9 is constructed as space-time plots by horizontally cutting below the orifice in the video frames for ASB at 34 mm orifice and HGS at 10 mm orifice. ASB particles pass the orifice continuously. The final phase of ASB discharge in Fig 2.9(b) shows that the outflow rate is not reduced compared with Fig 2.9(a). Instead, particles do not jump through the gap completely, only pass the lateral sides of the orifice. However, the way of the passage of soft, low-friction grains through a small orifice becomes different. Its outflow rate changes and fluctuates after some interruptions. In Fig 2.9(c), it is shown that the orifice is temporarily blocked. The length of the figure represents the time length, indicating the block can last for seconds and dissolve spontaneously.

The phenomenon of spontaneous non-permanent cloggings has been described for active matter like pedestrians and animals or thermal systems like colloids [72]. In the case of a soft granular system, there are transient clogs, with the majority of these temporary clogs formed by arches of 4 particles in the present 2D geometry. In Fig 2.9(c)-(d), the orifice is locked by a pair of particles that have partially occupied the bottleneck, exhibiting a bell-shaped signature in the space-time plot. Particles blocking the orifice experience continuous compression within the bottleneck until they suddenly drop down.

Fig 2.10 presents the distribution and cumulative distribution of the 'clog duration' for a 10mm orifice silo filled with HGS. We assess the temporal gap in mass variation. The number n of

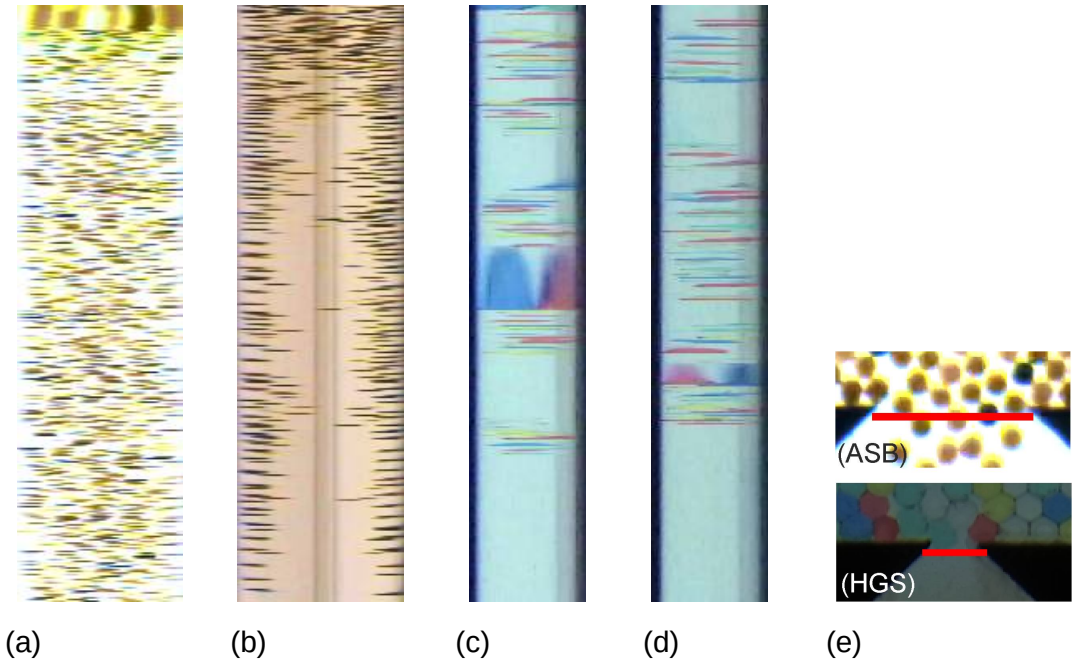

Figure 2.9: Space-time plots of cross sections directly below the outlet, time runs from top to bottom, each plot covers a time interval of 6s. The discharges started at time t_0. (a) ASB, $\rho = 5.7$, $(t_0 - 0.3\text{s})$ to $(t_0 + 5.7\text{s})$, (b) ASB, $\rho = 5.7$, $(t_0 + 23\text{s})$ to $(t_0 + 29\text{s})$, (c) HGS at $\rho = 1.55$, t_0 to $(t_0 + 6\text{s})$, (d) HGS at $\rho = 1.55$, $(t_0 + 480\text{s})$ to $(t_0 + 486\text{s})$. The cuts (a,b) are 36mm wide, and those in (c,d) are 12.5mm wide. e) shows the positions of the cross sections at the orifice. The image is reproduced from [71].

'clog duration' (up to about 3s) follows approximately a power law $n(\tau_t) \propto \tau_t^{\alpha}$ with exponent $\alpha = -1.85$. The graphs do not indicate that the system can be declared clogged, so we suggest the term 'congestion' to describe the phase of stopping outflow and then getting self-dissolving spontaneously. In Fig 2.10(a), the red scattered plot is for the time when the outflow mass is up to the first 400g of granular material, and the blue scattered plot is for the discharge after the first 400g of granular material have flown out. From this, the duration of congestions tends to be longer at lower filling heights, but the exponent is practically identical. Congestions lasting longer than 10s can also be supported by the cumulative distribution $N(\tau_t)$ of intervals longer than τ_t (see in Fig 2.10). In the power law $N(\tau_t) \propto \tau_t^{\beta}$, the exponent $\beta = -0.85$ is consistent with $\beta = \alpha + 1$. If $\beta \geq -1$, $N(\tau_t)$ would diverge when the distribution follows this power law for all τ_t. However, the exponent $\beta^{'} \approx -1.8$ (see solid line in Fig 2.10(b)) is below -1, so there always exists a mean congestion duration in the part of curve fitted in solid line, but there doesn't exist a finite limit for the 'clog duration' under the power law.

We take an HGS-filled silo with 10 mm orifice as an example and plot the space-time cut along the vertical central axis of the silo in Fig 2.11. As depicted in the figure, within 35 seconds, the flow stops after 3.5s, resulting in a zero outflow rate for the subsequent 21 seconds. Then the flow starts again. In the vertical cross-section, it is evident that the upper particles continue to move down when the outflow rate is zero, while the particles surrounding the orifice remain stationary. It is clearly shown that the HGS material entity never attains an equilibrium configuration within the silo, even in the presence of an arch above the orifice blocking the discharge. When the particles near the orifice form a stable arch, the structure within the granular bed undergoes further rearrangement. The distributions of particles and the force network could persist even when the flow halts. They can occur at any point and ultimately alleviate the congested state.

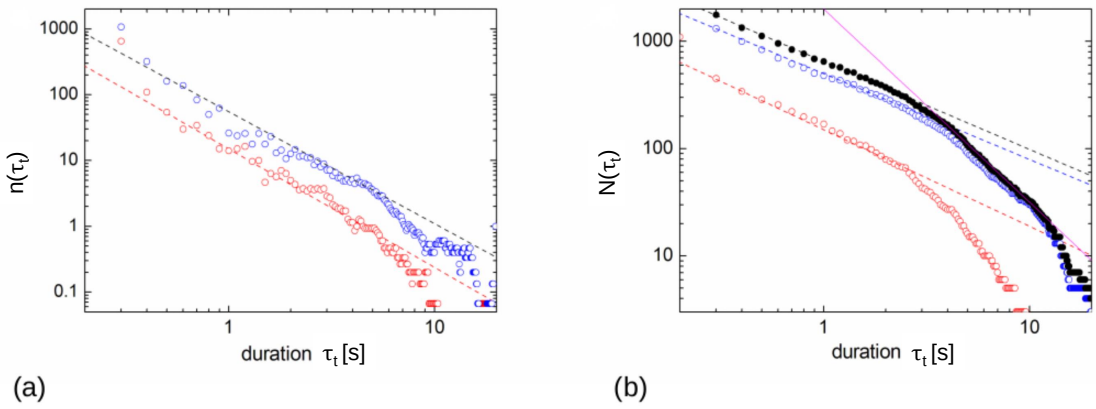

Figure 2.10: (a) Number $n(\tau_t)$ of plateaus of durations $(\tau_t - 0.1\text{s}) \ldots (\tau_t + 0.1\text{s})$ in the discharged mass curves, averaged over 12 discharges, 10mm orifice width. Red circles: clogs during the discharge of the first 400g (approximately 1/3 of the silo content), blue circles: clogs during the remaining discharge. (b) Cumulative plots of the same data, number of clogs $N(\tau_t)$ of plateaus with duration longer than τ_t. Solid circles represent the sum of both data sets: the dashed lines reflect power laws $N(\tau_t) \propto \tau_t^{\beta}$, the solid line marks $N(\tau_t) \propto \tau_t^{\beta'}$. The image is reproduced from [71].

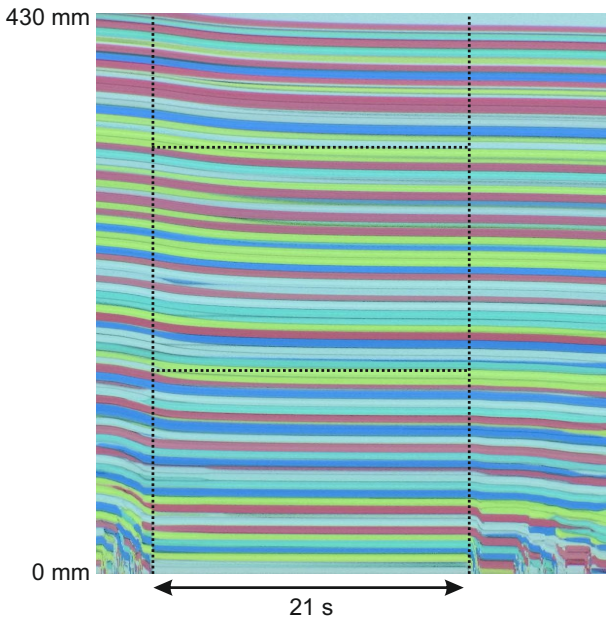

Figure 2.11: Rearrangement of the inner packing structure in the silo with 10mm orifice shown in a space-time plot. The interruption indicated by vertical dashed lines, lasts for 21s. While the particles at the bottom are immobile, one can see that the HGS spheres in the upper layers still move down. For better visibility of the downshifts, two dashed horizontal lines mark fixed heights. The image is reproduced from [71].

2.3 Discussion

In this chapter of the thesis, we analyzed the intermittent flow of soft, low-friction HGS spheres in a quasi-2D silo with a narrow orifice. The outflow rate, fluctuation, and packing reorganization were also discussed in this chapter. We also discussed the stability of the 'clogging' structure and the duration of congestions.

We find that fluctuations in a relatively broad range are related to the slow propagation of the packing fraction. Local flow in upper regions is with considerable retardation (see in Fig 2.4), so the inhomogeneous density or flow divergence is not compensated rapidly. This causes large fluctuations in the packing fraction and in the force networks, especially when the orifice is narrow, less than two particles wide. Then, the system can build up considerable pressure near the orifice when the flow suddenly stops, and the pressure gets relieved when the flow restarts.

One consequence is that the stress builds up after the orifice gets clogged, and the internal rearrangements of grains during 'clogging' can help to restart the outflow from the silo without external force. This is a qualitatively new observation, similar to other cases of intermittent flow found in hard particles in vibrated containers [73–75], in silos with oscillating bottom [76], or flocks of animals passing a gate [77]. It is supposed that the clogs dissolve by particles passing through packing gaps of the arch above the orifice. We will present this study in chapter 4.

On the other hand, a theoretical study [78] predicts that there is self-organization in a 2D hopper filled with frictionless disks when clogs occur, leading to intermittent flow. In experiments with hard particles, it is hard to observe because the systems quickly reach overall equilibrium and flow continues. Alternatively, in our experiments involving soft, frictionless particles, we observe that the structures within silos rearrange and 'clogs' can spontaneously dissolve. This leads us to speculate that friction may influence silo discharge, which will be discussed in the following chapter.

3 Silo discharge of mixtures of soft particles and hard grains

In the last chapter, we worked with pure monodispersed hydrogel spheres ensembles. The viscoelastic properties of HGS are supposed to be a significant feature that causes peculiar discharging characteristics through narrow orifices. But it remains unexplained whether the elastic modulus of the particles (of the order of dozens kPa), the low friction coefficient (of the order of 10^{-2}), or a combination of both factors causes this peculiar feature of discharge.

From the perspective of clogging, which is a fundamental challenge in the storage of grains within silos and hoppers, particles can form stable arches in 2D silos or domes in 3D silos above the orifice and block further outflow. Through large enough orifices, hard grains flow at constant rates given by geometrical and physical parameters, which can be derived from theoretical models [21, 61–63]. When the orifice size is smaller than about five-particle diameters [79, 80], hard spheres tend to form clogs and block further outflow until the clogs are destroyed by shaking the container, or by applying air flushes. Besides, homogeneous granular ensembles are often idealized. People usually deal with materials that vary in terms of size, shape, friction, elasticity, or other properties.

Thus it motivates us to study mixtures of soft and hard particles and their silo discharge behavior, such as flow rates and clogging. When small portions of hard particles are mixed with soft particles, the ensembles differ in frictional properties. This chapter describes an experimental study with the help of a numerical analysis of the mixture of soft and hard particles (10% hard particles in the mixture). It also discusses the silo discharge of this mixture in 3 aspects: (1) the effect of doping on silo discharge characteristics; (2) the concentration x_{ASB} of hard grains in the composition of the blocking arches; (3) the outflow rate during the discharge of the mixtures, the different flow rates between mixed and pure ensembles.

3.1 Introduction of the experiments

The quasi-2D setup (80cm height, 40cm width but only 34cm width are visible in the captured images, slightly more than 6mm depth) with one layer of particles between two vertical glass plates is used as in the last chapter, see in detail the section of describing the experimental setup of chapter 2.

The material to fill the silo is a mixture of soft, low-friction hydrogel spheres (HGS) and hard frictional plastic airsoft bullets (ASB). The concentration of ASB plastic grains is low, typically 5% or 10%. We define the aspect ratio D/d as the value of the orifice size D divided by the particle diameter d. In this study, this ratio is in the range of $1.7 < D/d < 2.2$. Note that a pure sample of ASB grains would immediately clog at such small orifices. At large orifice sizes ($D/d > 3$), the dynamics of the mixtures in our case is practically identical to the pure hydrogel samples.

The hydrogel spheres and airsoft bullets applied in this study are the same as we used in chapter 2 (also see the part of the experimental setup). To be mentioned, these two types of particles have nearly the same density of approximately $1020\text{kg}\cdot\text{m}^{-3}$. The friction coefficient of the ASB grains is 0.3. They are incompressible and can be considered rigid. The mass of HGS particles after swelling in salted water is about 0.15g. The final diameter is about 6.5mm, and the elastic modulus is in the range of approximately 50kPa to 100kPa.

3.2 Experimental results

3.2.1 Avalanches and clogging probabilities

The mean number of grains flowing out during an avalanche is directly related to the probability that a particle becomes one of the components for blocking structures around the orifice. The statistics of the avalanche size distribution [81] for hard grain samples can be described as follows, see equation 3.1. It is postulated that the probability P remains constant upon the formation of a clog after the Sth particle falls out. Then, the probability P_S of the clog blocking an avalanche of size S is

$$P_S = (1-P)^{S-1}P = Pe^{[-\frac{S-1}{S_0}]} \tag{3.1}$$

with $S_0 = -1/ln(1-P)$ (if only one particle passes through the orifice and then gets clogged, the probability P would be 1). The mean avalanche size $\langle S\rangle$(see equation 3.2) can be counted as follow:

$$\langle S\rangle = \sum_{S=1}^{\infty} SP_S = \frac{1}{P} \tag{3.2}$$

$\langle S\rangle$ is a characteristic parameter used to describe silo discharge statistics. In practical situations (i. e. $\langle S\rangle \gg 1$), $\langle S\rangle$ and S_0 can be considered equal. In experiments, it is usually used to evaluate the cumulative probability $\Pi(S)$ of avalanches having particles more than S (following in equation 3.3):

$$\Pi(S) = (1-P)^S \tag{3.3}$$

S is how many particles have passed the orifice with probability $(1-P)$. The avalanche statistics is found by a fit into the exponential relation $\Pi(S) = e^{-\frac{S}{S_0}}$. One can assign different clogging probabilities P_{ASB} and P_{HGS} to the corresponding components.

Fig 3.1 shows the discharge mass curve of a mixture of hard and soft spheres in a silo with a narrow orifice. Plateaus in the curve either represent non-permanent clogging dissolved or clogs destroyed by air flushing (marked with arrows). In our experiments, with an aspect ratio D/d of around 2, the clogs are formed by very few grains, four on average. Thus, the experiments provide favorable conditions to observe the statistics on the particle scope level around the orifice. On the other hand, the soft hydrogel material guarantees the formation of comparably large avalanches for reasonable statistics at these small aspect ratios D/d. To be mentioned, some plateaus in Fig 3.1 include non-permanent clogs or congestion which dissolve spontaneously (and also found in a previous study [71]). Yet, there is no distinct criterion capable of distinguishing between the end of an avalanche and the beginning of non-permanent congestion. In this study, we introduce an *ad hoc* criterion to extract different avalanches: a clog lasting for at least one second. However, the arbitrary selection of a threshold may influence the statistics considerably [72]. Fig 3.2 shows the distribution of the cumulative probability of avalanche size S. The avalanche counted is followed by clogging lasting one second for non-permanent congestions and long clogs destroyed by air flush (the *ad hoc* criterion). Technically, from Fig 3.2 we can see that the component of HGS or a small amount of ASB affects the avalanche sizes. The more ASBs were introduced, the smaller the avalanche sizes. Strangely, 95% HGS + 5% ASB samples, only in this case, the probability of avalanche sizes is also influenced by the orifice size. Additionally, in the cases of an orifice around 13mm, the probability of avalanche sizes in the range of $0 \sim 100$ is similar for the samples of pure HGS and 95% HGS.

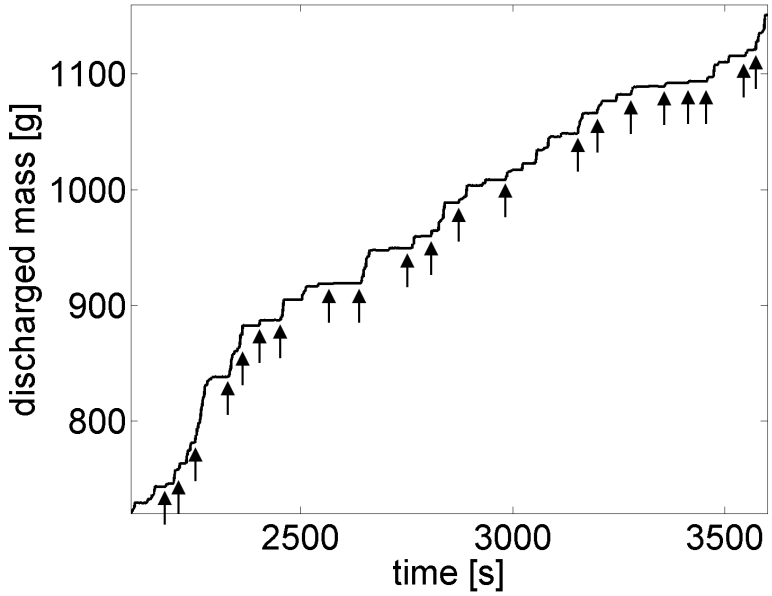

Figure 3.1: A partly measured time dependence $m(t)$ of the mass of granular material discharged from a quasi-2D silo. The mixture contained 10% rigid air soft balls with 90 % hydrogel spheres, both with 6mm diameter. The orifice size was 11mm. Some clogs (plateaus) dissolved spontaneously, and clogs labeled by arrows were destroyed by an air flush through the orifice. The image is reproduced from [82].

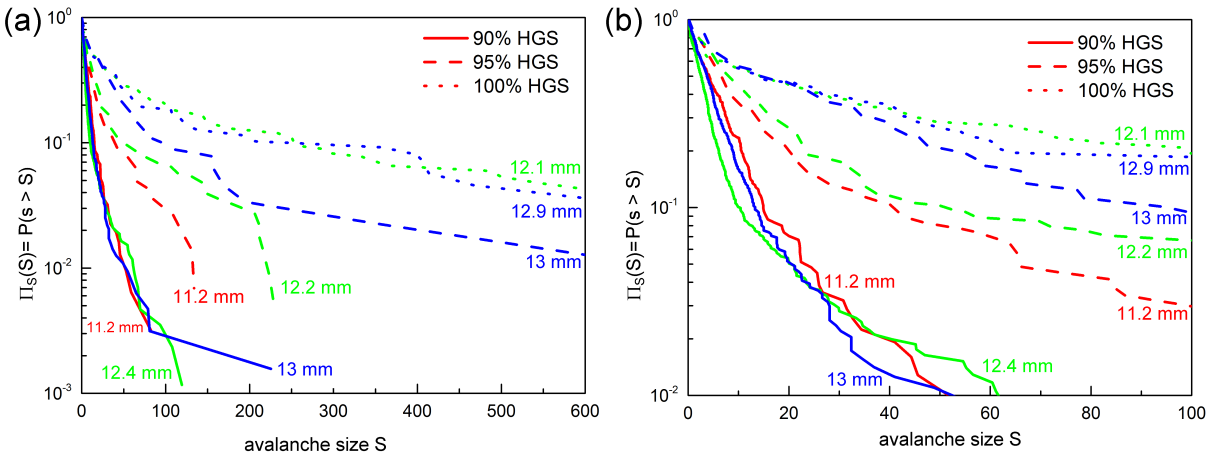

Figure 3.2: Cumulative probability of $\Pi(S)$ of avalanche sizes larger than S. Note that the mass of each sphere is about 0.15g. The number of particles of avalanches can be calculated from the differences in the outflown mass. Avalanche size (a) in the range of $0 \sim 600$ (b) in the range of $0 \sim 100$, these two subfigures are from the same dataset. The solid line represents 90% HGS + 10% ASB, the dashed line represents 95% HGS + 5% ASB, and the dotted line represents 100% HGS. Different orifice sizes are marked with different colors in each figure. The red color is for the orifice of 11.2mm, the green line is for the orifice of around 12mm, and the blue line is for the orifice of around 13mm.

3.2.2 Pressure characteristics

In the last chapter, it was concluded that the low-frictional hydrogel shows close hydrostatic characteristics of the pressure p at the bottom of a quasi-2D silo filled up to height h [69]. On the other hand, hard frictional grains display pressure saturation at the bottom of silos when a certain height is reached [15, 69]. Fig 3.3 shows that the pressure characteristics of the pure hydrogel sample are significantly changed by an additional small amount x_{ASB} (10%) of ASB spheres. The data is recorded by measuring the normal force on a 4cm horizontal bar with a load cell which is used to replace part of the bottom container border. The weight of the material at the upper layers is partially transferred to the container walls. The packing fraction ϕ of the

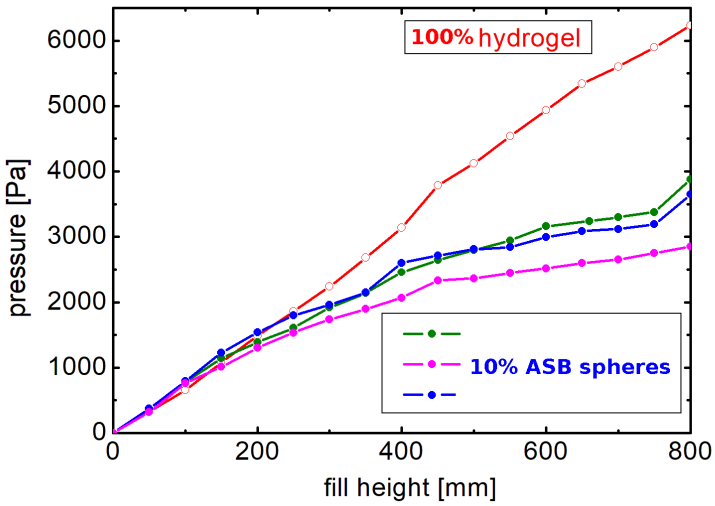

Figure 3.3: Pressure at the bottom of the container at the position of the outlet for 100% hydrogel system (open circles), and three independent measurements of a mixture with 10% ASB spheres (filled circles). The image is reproduced from [82].

silo with hydrogel particles increases toward the bottom. The densest packing of spheres with diameter $d = 6.5$ mm in a quasi-2D hexagonal lattice within a layer of thickness $d = 6.5$ mm is $\phi_{max} = \frac{\pi r^2}{3r^2 \tan 60^\circ} = \frac{\pi}{\sqrt{27}} \approx 0.604$. This is the mean packing fraction of pure hydrogel spheres since they form a nearly defect-free hexagonal lattice at the depth of the granular bed. At the bottom, the packing fraction even reaches up to 0.65 where the hydrogels are squeezed and deformed. In the very top layers, it might drop down to around 0.5.

3.2.3 Flow rate and clog duration

This part collaborated with Bo Fan, one of the co-authors from the published paper [82], who studies at WIGNER Institute in the Caliper project. He was in charge of analyzing the flow rate, such as Fig 3.4, 3.5, and 3.8. Fig 3.4(a) shows how the outflow rate is altered by changing the size of the orifice for a given mixture, similar to the case of 100% hydrogel particles where the orifice size is one of the determining factors to influence the outflow rate [21, 83]. First, we can see that with a 13mm orifice, the ensemble flows smoothly at the beginning until the filling level is lower than 20∼25cm. In the silo with a 12mm orifice, clogs occur after avalanches of the order of 100g (around 1000 particles). A small fraction of ASB particles influences the statistics of clogs no matter whether clogs are permanent or not, and also impacts the flow rate between

clogs. In Fig 3.4(b) for 3 cases with different amounts of ASB spheres, the orifice sizes D are ≈ 11.5 mm. Fig 3.4(c) is trimmed from Fig 3.4(b) by removing all clogs longer than 1s. The

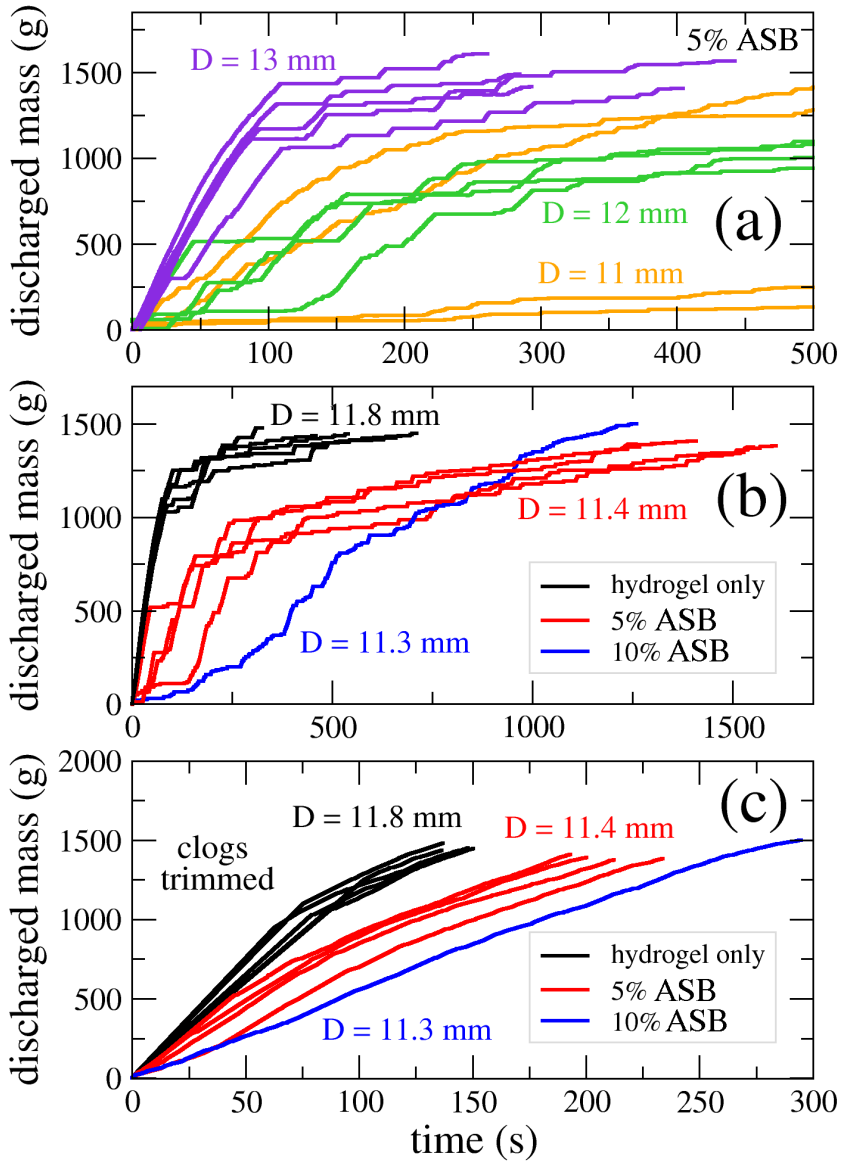

Figure 3.4: (a) Time dependence of the discharged mass for a sample containing 5% hard frictional spheres of airsoft bullets (ASB) for 3 values of the orifice width D. It is evident that the probability of clogging increases strongly with lower ratios of orifice width to particle diameter. (b) Time evolution of the discharged mass for 3 different samples: pure hydrogel, and mixtures containing 5% or 10% ASB spheres. The orifice size D is indicated in the figure. The horizontal sections correspond to the clogs. (c) Same data as panel (b) but with clogs longer than 1s trimmed. The flow rate is measured as the local slope of these trimmed curves. The image is reproduced from [82].

slope of Fig 3.4 at every moment gives the instantaneous discharge rate as a function of filing height h(the height is according to timeline) which is shown in Fig 3.5(a). For the sample of 5% ASB gains, the dependence of the flow rate is much lower, while for the sample of 10% ASB grains, the dependence has essentially vanished. Thus, adding a small amount of frictional hard beads to the hydrogel-particle ensemble exerts a significant influence on the discharge rate. When increasing the concentration of ASB grains (take as an example among our cases, 10% ASB spheres), the systems show the characteristics of height independence of the flow

rate in the dynamics of hard granular materials. The low friction coefficient of the hydrogel can play a role in the outflow rate [83, 84]. Fig 3.5(b) presents how the flow rate depends on the orifice size D in different components of mixture samples in the range of filling height 40 $\sim$ 45cm. The outflow rate decreases with orifice size and an increasing concentration of hard grains reduces the flow rate. As predicted by Beverloo's model in a quasi-2D silo, the flow rate is $Q = C\phi\rho_p H\sqrt{g}(D-kd)^{1.5}$, with grain diameter d, density ρ_p of grains, packing fraction ϕ, cell thickness $H \approx d$ and adjustable constants k and C. If the data in Fig 3.5 are fitted to Beverloo's equation, it can be found that $k \approx 1.4 \sim 1.6$ and C would be in the range from 3.6 for the 90% HGS sample to around 6 for the 100% HGS sample (see the fitting data in Fig 3.6). To be mentioned, the constant C partially relates to the silo geometry which can involve the instant filling height as presented in Fig 3.5(a). This is also evident in Fig 3.5(c) that the flow rate of 100% HGS samples changes with height during discharge at different orifice sizes.

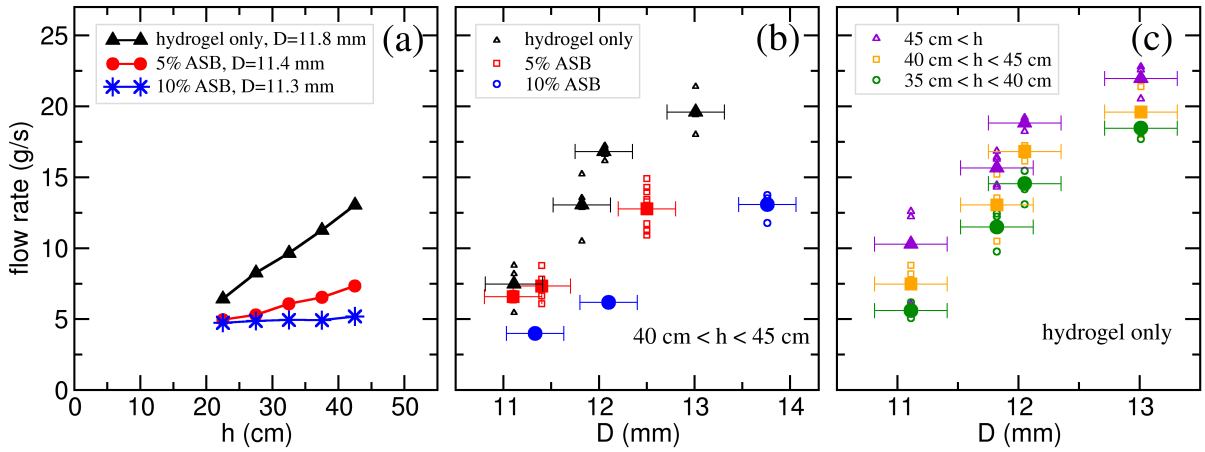

Figure 3.5: (a) Flow rate as a function of the bed height h for pure hydrogel and for mixtures with 5% and 10 % ASB spheres. (b) Flow rate as a function of the orifice size D for all 3 samples for a bed height of 40cm $< h <$ 45cm and for (c) pure hydrogel samples at various bed heights h. Small open symbols represent individual experiments, and largely filled symbols show averages of the respective data sets (on average 4 experiments). The image is reproduced from [82].

Then we want to see the influence of the number of ASB grains near the orifice on the flow rate, see Fig 3.7. The region considered to count ASB grains around the orifice is the area of a half circle with a radius of $5d$ above the orifice. When the filling height $h > 37.5cm$, the flow rate decreases with more than 3 hard grains in this region. For $h < 37.5cm$, the flow rate fluctuates instead of decreasing with more ASB grains in the region. It can be explained that when the silo is filled up to 40cm high, the pressure is approximately 3kPa, and the pressure can make the soft particles get deformed at the bottom, but when the filling height gets lower, the deformation would be less intense and it shows the characteristics of low friction and inelastic particles.

Non-permanent congestion also appears in the mixture system, as shown in Fig 3.1, similar to previous observations of pure hydrogel sphere ensembles [71]. The plateaus without arrows marked in Fig 3.1 demonstrate that the congestion at the orifice ends spontaneously without external interference by air flush. Fig 3.8(a) with a bent dashed line describes the delay of flow when the grains start to flow locally at the orifice. The particles still reorganize slowly in the upper regions during the congestion period of 1.75 seconds as shown in Fig 3.8(b) compared with the positions of particles immediately after the outflow stops which are re-plotted behind the white gap. Compared to the pure hydrogel samples in the previous study (see chapter 2), the addition of a few percent of hard grains could slightly extend the delay duration. Then we

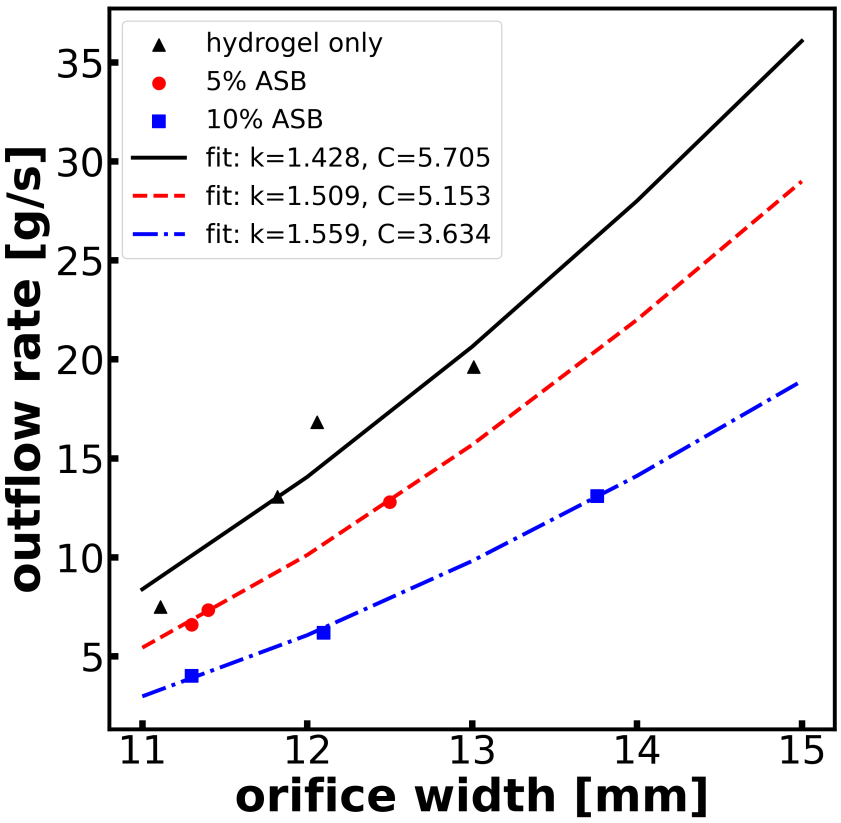

Figure 3.6: Averaged flow rate as a function of orifice size D for all 3 samples for a bed height of 40 cm $< h <$ 45 cm, fitting to the Beverloo's equation. The scattered data is taken from the averaged flow rates in Fig 3.5(b).

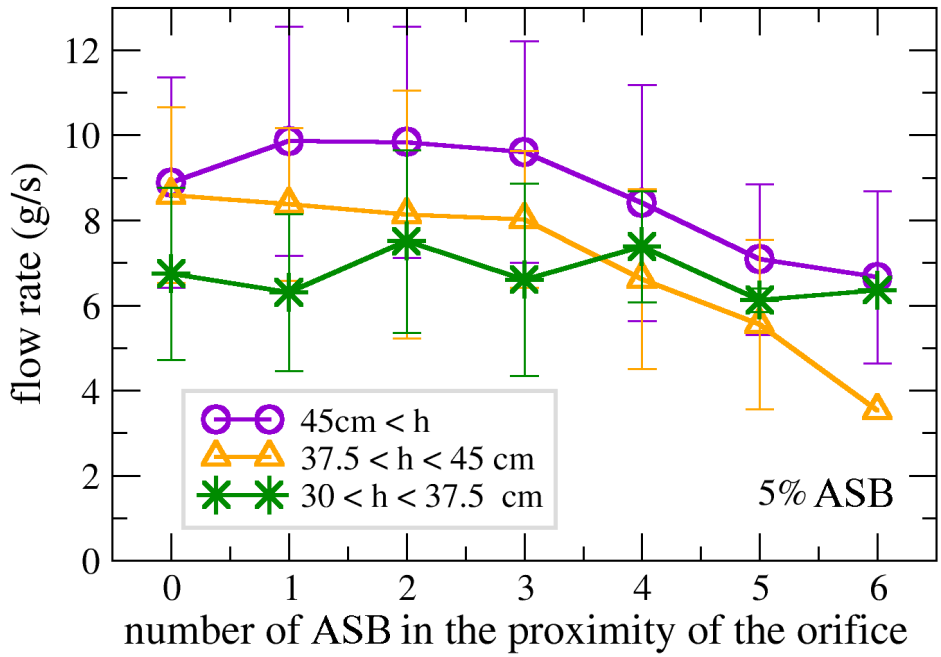

Figure 3.7: Flow rate as a function of the number of ASB grains in the proximity (5 particle diameters) of the orifice of 11.4mm. Data taken for 30cm$< h <$ 80cm. Data points represent 18 measurements on average, error bars stand for fluctuations in different measurements. The image is reproduced from [82].

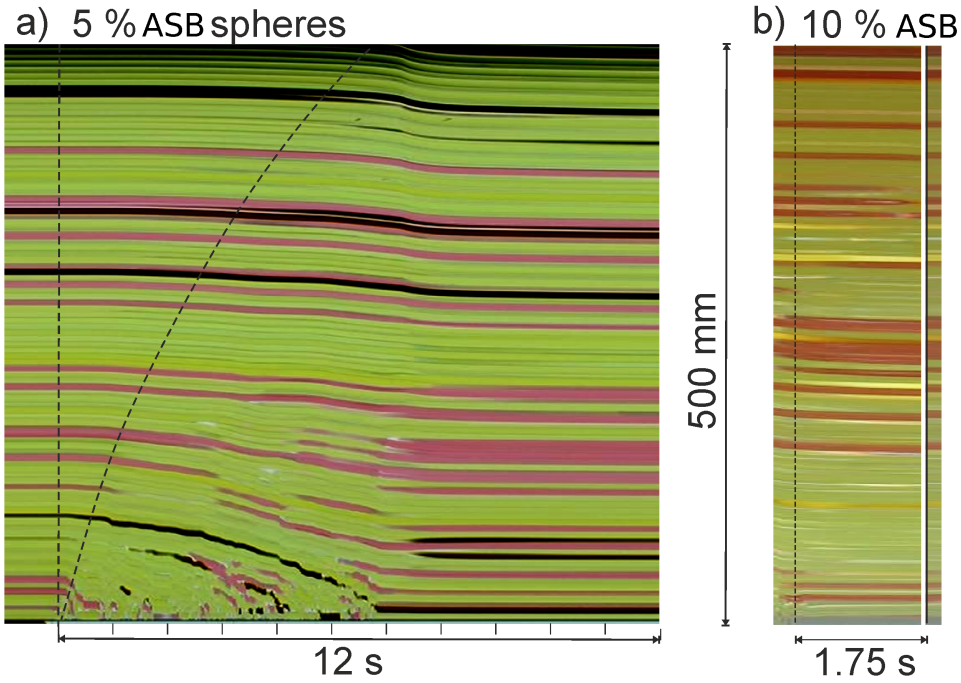

Figure 3.8: Space-time plots of a vertical cross-section of the silo in the central axis above the orifice ($D = 12$mm). (a) Mixture with 5% ASB spheres. The grains start to flow only locally at the orifice after it is opened (vertical dashed line). The reaction of the material in the upper part is delayed considerably (bent dashed line). (b) After the orifice at the bottom clogs (dashed line), the material (with 10% ASB spheres) in the upper part still reorganizes for several seconds. The state immediately after the outflow stopped is re-plotted behind the white gap, to visualize the changes during the clogged state. The image is reproduced from [82].

would analyze how the duration of clogs (all kinds of clogs, dissolved by external air flush or dissolving spontaneously) depends on the number of ASB spheres. As shown in Fig 3.9(a), the clog duration increases with the number of ASB spheres increasing. Hard frictional beads in the first and second layers affect the clog duration but the first layer gives more influence. In Fig 3.9(b), it is about the probability that the clog is longer than the time interval τ in the log-log scale. It can be seen that the clog duration in the pure hydrogel sample is very close to the clog duration in the situation that there are no ASB spheres in the first 2-layer shells for a mixture with 5% ASB spheres. However, the clog duration extends considerably in the mixture when ASB spheres show up in the first 2 layers above the orifice.

3.2.4 Arch structure analysis

A few types of clog structures are formed in the quasi-2D silo with narrow orifices. The most frequently encountered structure in all 3 orifice sizes of our experiments is the closely symmetric 4-particle arch. Also, nearly symmetric 2-particle clogs are encountered when the orifice width is two times of particle diameter. These typical structures are shown in Fig 3.10.

Fig 3.11 shows the statistics of clog structures grouped by the number of particles in the arches in three orifice-size (11mm, 12mm, 13mm) systems and two species components (5% ASB, 10% ASB) of mixtures. Here, we examine clogs lasting over 1.5s without distinguishing temporary congestion and permanent clogs that have to be destroyed by air flushes. Three-particle and five-particle arches are found more often in systems with larger orifices. Four-particle arches appear around 80% $\sim$ 90% among all arch structures. Therefore, we focus on the four-particle

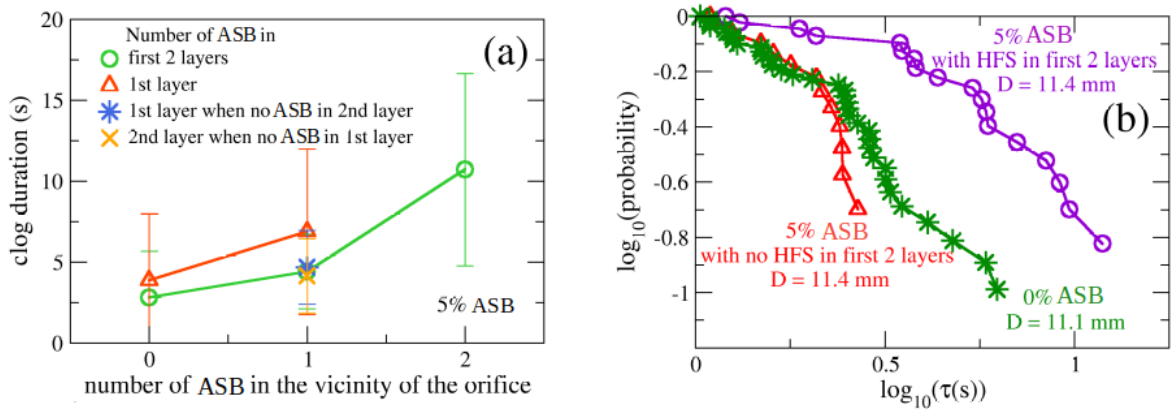

Figure 3.9: (a) Clog duration as a function of the number of high friction (ASB) spheres in the vicinity of the orifice of 11.4mm. The data sets correspond to cases when only the first layer or the first 2 layers are considered. Data points represent 13 clogs on average, error bars stand for the standard deviation. (b) Probability of non-permanent clogs longer than τ as a function of τ on a log-log scale. The image is reproduced from [82].

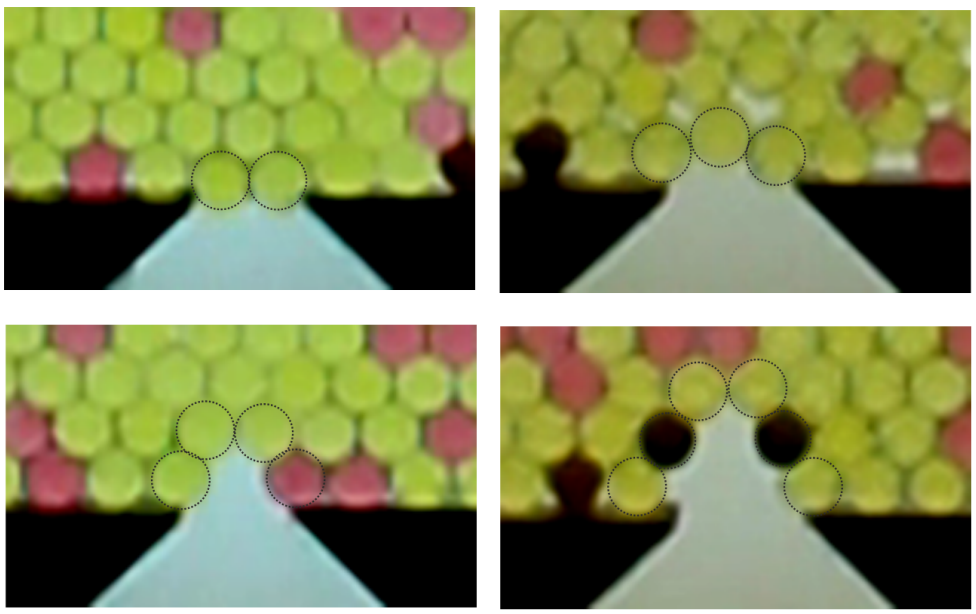

Figure 3.10: Typical structures of blocking arches. The 2- and 4-particle arches were taken from snapshots of clogged states of the 11mm orifice videos, and the 3- and 6-particle arches from 13mm orifice videos. The image is reproduced from [82].

arches in the following analysis.

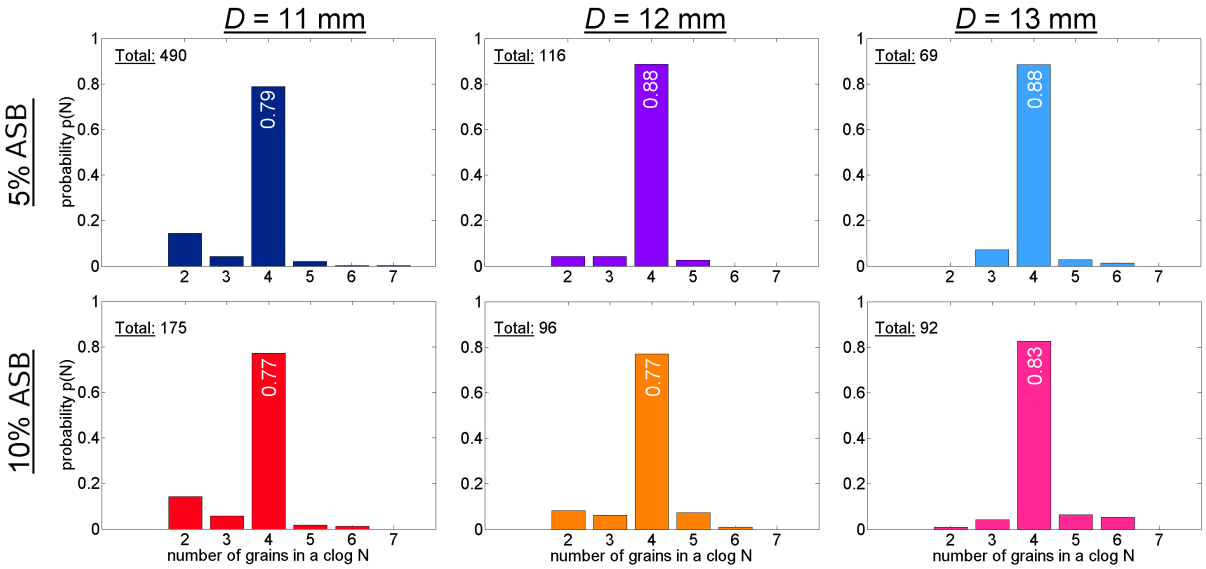

Figure 3.11: Number of particles forming the blocking arches at the orifice for two mixture compositions and three orifice sizes. It is seen that neither the composition of the mixtures nor the variation of the orifice width influences the dominance of 4-particle clogs. Clogs consisting of 2 particles are much less probable in the larger orifices. The image is reproduced from [82].

Moreover, Fig 3.12(a) shows the relative amount X_{ASB} of hard grains in the first layer of arch structures. White numbers are the total number of arches with respective types among all evaluated experiments. Horizontal dash lines marked crossing each bar indicate the percentage x_{ASB} of hard grains in the mixture. The result is that hard grains appear in the arches nearly two times more often than the concentration in the sample. In arches with non-4-particle structure of the arch, the relative amount of ASB grains is over-represented, yet the statistical error is larger because of the smaller number of non-4-particle arches.

To interpret that over-presentation, one can make a simple assumption that X_{ASB} and x_{ASB} are related by approximation as follows:

$$X_{ASB} = \frac{x_{ASB}P_{ASB}}{x_{ASB}P_{ASB} + (1 - x_{ASB})P_{HGS}} \tag{3.4}$$

From this equation 3.4, we can get a rough estimate of the ratio of arch component probabilities $\frac{P_{ASB}}{P_{HGS}}$ of hard and soft components of the mixture:

$$\frac{P_{ASB}}{P_{HGS}} = \frac{X_{ASB}(1 - x_{ASB})}{x_{ASB}(1 - X_{ASB})} \tag{3.5}$$

Taking the values of x_{ASB} and an approximated factor from the previous analysis (see in Fig 3.12(a)) of $X_{ASB} \approx 2x_{ASB}$, we can estimate $\frac{P_{ASB}}{P_{HGS}} \approx 2.2$. Hard grains, compared to hydrogel particles, are nearly twice as likely to get stuck in an arch structure, regardless of the orifice width D in our study. Fig 3.12(b) is to check how often ASB grains appear in the second layer of grains above the orifice. As expected, the occurrence of ASB spheres is not significantly enhanced compared to results in Fig 3.12(a) in all kinds of clogs, the slight deviation from x_{ASB} is within the statistical error.

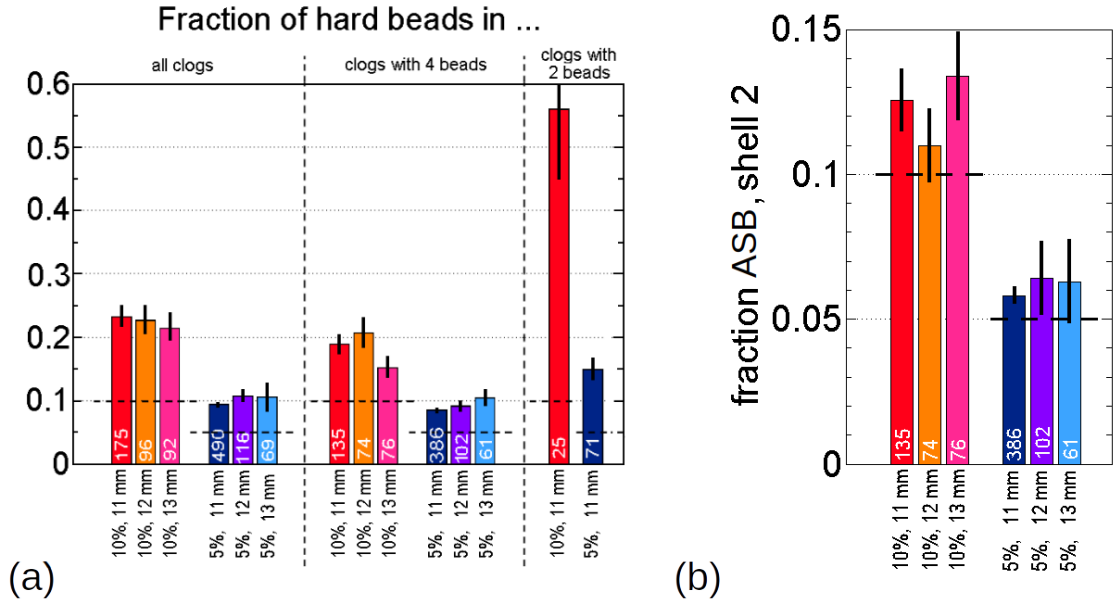

Figure 3.12: Statistics of the occurrence of ASB spheres in the blocking arches in the experiments. The white numbers indicate the number of events compiled in the column. a) Composition of the arch, viz. the first coordination shell above the orifice; fractions X_{ASB} of hard beads compared to the bulk concentrations x_{ASB} (dashed lines). The left section includes all clogs of at least 1.5s duration. In the middle, the statistics for 4-sphere arches are shown. On the right, data from 2-sphere arches are collected. b) Concentration of ASB spheres in the second coordination shell, averaged over all clogs. The image is reproduced from [82].

3.3 Numerical analysis

This section collaborated with Tivadar Pongó, one of the co-authors in the same published paper [82], who graduated from the University of Navarra in the CALIPER project. He was responsible for conducting DEM simulations and processing the numerical data from the simulations. The numerical simulations are carried out with the open-source Discrete Element Method granular simulation software LIGGGHTS [85]. For the calculation of the inter-particle force F_{ij}, a Hertz contact model was chosen [86], including normal and tangential components, which are both modeled as short-range spring dashpot interactions. The elastic and damping particle-particle interaction coefficients are well reproduced by several input parameters given in the contact model, i. e. Young's modulus Y, the restitution coefficient e_n, and the friction coefficient μ. The Coulomb friction constraint is applied. The tangential force is cut off when $F_{ij}^t < \mu F_{ij}^n$ is satisfied. When soft particles are densely packed, a multi-contact force model can capture the experimental response [87]. Nonetheless, we assumed the contacts between particles were mutually independent, employing the upper limit of Young's modulus for densely packed soft particles.

The numerical geometry is the same as the experimental setup, i. e. the width of the flat silo is 40cm, and the depth of the silo is 6.12mm, slightly larger than the particle diameter $d = 6$mm. The density is set as $\rho = 1000\text{kg} \cdot \text{m}^{-3}$. The mass of each particle is around 0.12g, slightly lighter than it measured in the experiments. The contact coefficients such as Young's modulus and friction coefficient are also similar to the real airsoft bullet and hydrogel particle employed in the experiments. For the contact between soft low-friction spheres, Young's modulus was set as 100kPa, and the friction coefficient of hydrogel particles $\mu_{HGS-HGS}$ as 0.02, which are

consistent with the earlier study [88]. Young's modulus was set at 50MPa and friction coefficient 0.6 for the contact between hard frictional spheres. Besides, ball bouncing experiments led to a rough estimation of the restitution coefficient, for hydrogel spheres $e_n = 0.5$, and airsoft bullets $e_n = 0.3$. The friction with the walls was set equal to the particle-particle friction i. e. $\mu_{ASB-wall} = \mu_{ASB-ASB}$ and $\mu_{HGS-wall} = \mu_{HGS-HGS}$.

The used sets of orifice widths were $D = 11, 12, 13, 14$mm corresponding to aspect ratios of $D/d = 1.83, 2.0, 2.17, 2.33$. The simulation can replicate the clogging and intermittent flow observed in the experiments within the same flow geometry. A simple procedure is implemented to resolve clogs: the number of particles in the silo is compared every second with the number of particles in the silo at the previous second, in case the difference is found to be zero, if the center of a particle is located in the region of a half circle from the center of the orifice with a radius of 5mm, the particle in this vicinity of the orifice would be moved up with force of 0.0001N only in vertical direction for 0.1s, imitating air flush. Simulations for each case are run for 4 times with different random initial packing configurations.

3.3.1 Flow rate

Fig 3.13 displays systems containing only HGS, HGS with 5% ASB particles, and HGS with 10% ASB particles. Fig 3.13(b) is about the discharged mass with time changing, but removes the period when the flow rate is zero. As noticed, the addition of even a small number of ASB grains leads to a clear reduction of mass flow rate.

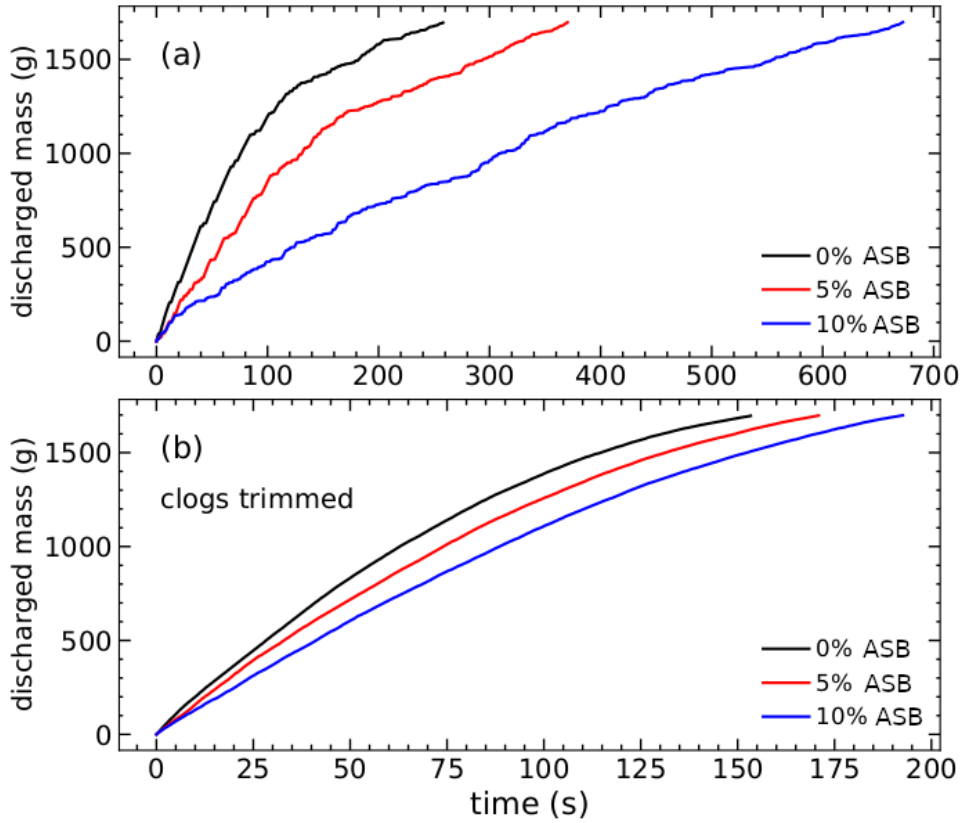

Figure 3.13: Discharge characteristics calculated numerically for $D = 11$mm, $\mu_{HGS-ASB} = 0.2$. The top graph shows the original data, the bottom graph presents the same data adjusted by trimming the phases of stopped outflow. The image is reproduced from [82].

Fig 3.14 summarizes the mass flow $\frac{dm}{dt}$ as a function of height h. The mean bed height $h(t)$

is obtained by sampling ten equally sized vertical slices and locating the highest particle h_k in each of them, and then the value of $h(t)$ is calculated as the average of that ten-slice set. We assume the friction coefficient between the two kinds of particles as $\mu_{HGS-ASB}$ and apply this parameter to varying compositions of systems in simulations. Take the case of one orifice size $D = 12$ mm, Fig 3.14(a)-(c) illustrate outcomes corresponding to $\mu_{HGS-ASB} = 2.5\mu_{HGS-HGS}$, $\mu_{HGS-ASB} = 10\mu_{HGS-HGS}$, $\mu_{HGS-ASB} = 15\mu_{HGS-HGS}$. First, the numerical model reproduces that the mass flow rates of mixtures, and pure HGS particles decrease with the filling height decreasing. Secondly, with the rise in the concentration of ASB particles, reflected by the impact of friction coefficient $\mu_{HGS-ASB}$ in the system, the flow rates tend to be constant, resembling a mass flow that is becoming less dependent on height.

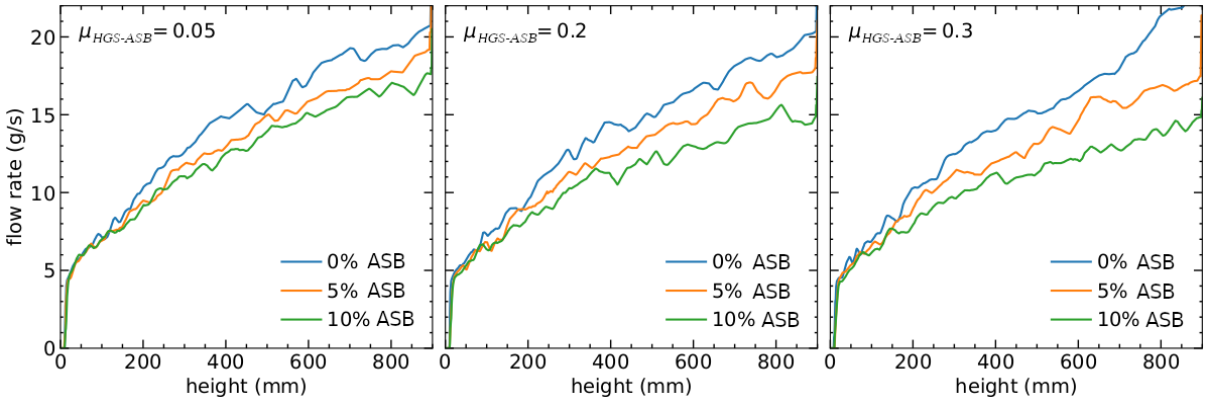

Figure 3.14: Numerically calculated flow rate as a function of bed height for different mixture ratios and an orifice size of $D = 12$ mm. The interspecies friction i.e. the friction between the ASB and the soft, low-friction particles, reflected in $\mu_{HGS-ASB}$, is different in the subfigures. The image is reproduced from [82].

In addition, Fig 3.15 is obtained by flow rates changing with different orifice sizes. The flow rates are averaged over various time intervals, each corresponding to different ranges of filling height. As expected, we find that the mass flow rate increases with increasing orifice size and the flow rate is linearly changing with orifice size, which is similar to the experimental results in the front section. The friction coefficient between particles of different types strongly influences the outflow rate, specifically, the flow rate is reduced with $\mu_{HGS-ASB}$ increasing.

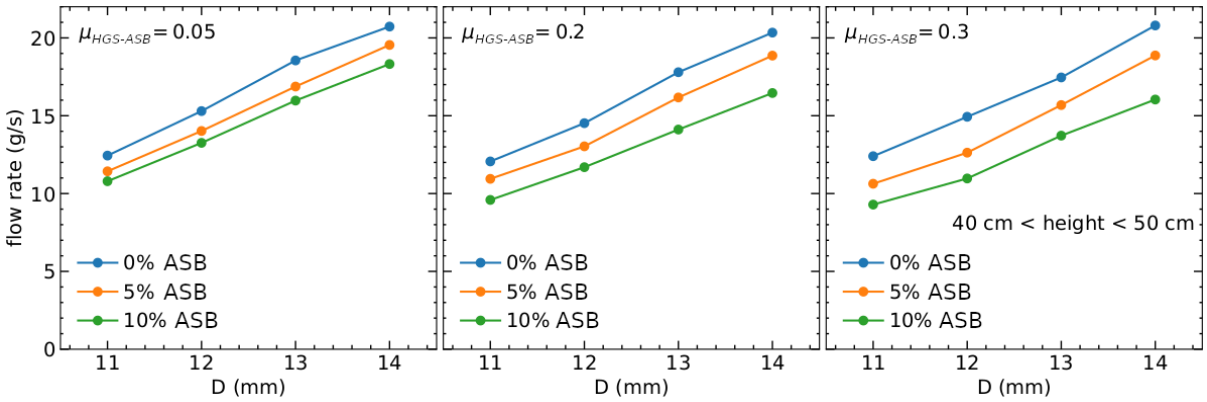

Figure 3.15: Average flow rate in a small range of bed height (40 cm $< h <$ 50 cm) as a function of orifice size. In these numerical simulations, the inter-species friction is increased from the left figure to the right $\mu_{HGS-ASB} = 0.05;\ 0.2;\ 0.3$. The image is reproduced from [82].

3.3.2 Structure of arches

Fig 3.16 presents the probability distribution $p(\delta t)$ with different compositions for comparison. δt is the statistical time interval between two consecutive particles passing through the orifice. Similar to the experimental trend of the clogging statistics. The distribution shows a well-defined peak at $t_d \approx 0.006$ s, correspondingly the most probable vertical velocity of particles crossing the orifice is $v_d \approx 0.5$ m·s^{-1}, significantly larger than the free fall value $\sqrt{2g\frac{D}{2}}$ (D is the orifice width). This indicates that the pressure gradient at the orifice in the up-down direction is an important factor of affecting the outflow velocity. Moreover, it also suggests two consecutive particles flow out within a vertical distance of $\frac{D}{2}$ on average.

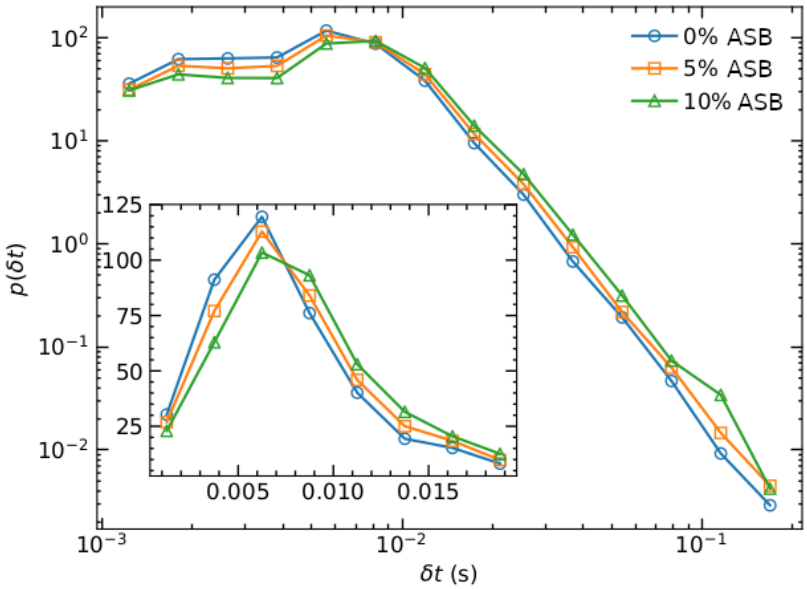

Figure 3.16: Probability density of the elapsed time between two particles passing in log-log representation. In these numerical simulations, the inter-species friction was $\mu_{HGS-ASB} = 0.2$, while the orifice size was $D = 12$ mm. The inset shows the same data but in a smaller region with linear axes. The image is reproduced from [82].

Then we practically define an infinite passing time over $\delta t = 1s$: when δt is above 1s, the system is considered permanently clogged in a stable blocking arch. Fig 3.17 presents the statistics of the occurrence of ASB spheres in the blocking arches. This shows the closest match to the experimental results for all clogs with an inter-species friction $\mu_{HGS-ASB}$. The fraction of ASB particles forming arches is higher than their bulk fraction, indicated by the horizontal dashed line. The increasing inter-species friction also enhances the occurrence of ASB spheres considering all clogging states. Moreover, if we select arches composed of only two particles, we find that in this case, the arches are always made up of two ASB spheres. Additionally, increasing the inter-species friction decreases the occurrence of ASB particles in arches. The increasing inter-species friction enables arches formed by a combination of one hard and one soft sphere to be as probable as those formed by two hard particles.

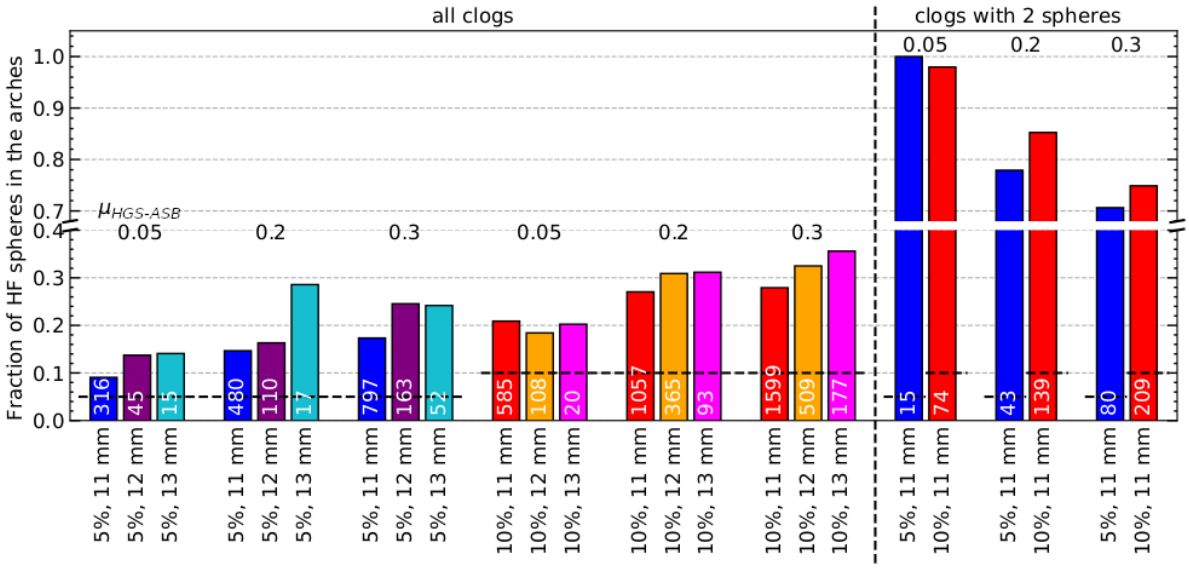

Figure 3.17: Statistics of the fraction of ASB spheres in the blocking arches in clogged states in numerical simulations. The bars represent the mean fraction of ASB spheres in the arches compared to the bulk concentration (dashed horizontal lines). At the right of the vertical dashed line, the clogs composed of only 2 spheres are considered, while on the left all occurrences are included. Under each bar, the percentage of ASB spheres in the silo and the orifice size are indicated. The inter-species friction $\mu_{HGS-ASB}$ is shown. The white numbers indicate the number of events compiled in the column. The image is reproduced from [82].

3.4 Discussion

In this chapter of the thesis, we discussed that an ensemble of soft, low-friction spheres with a small percentage of hard frictional grains has obvious consequences of flowing through a narrow orifice and clogging statistics in a quasi-2D silo.

The addition of a few percent of hard spheres restores the pressure-independent outflow characteristics predicted by Beverloo's equation. When increasing the concentration of ASB grains, the systems show the characteristics of height independence of the flow rate in the dynamics of hard granular materials, which can be explained by the lower importance of the elasticity of HGS particles on the discharge rate. However, at a large filling height of the silo, like 40cm height (pressure approximately 3kPa), the outflow rate is around 2.5 times larger for the pure hydrogel sample than for the 90% hydrogel mixture. It can be explained that the high pressure at the bottom can deform the soft grains and squeeze them out other than the low friction of hydrogel resulting in velocity differences in samples with different concentrations of hard particles.

On the other hand, the probability that a hard frictional particle is involved in the formation of the blocking arch is twice as large as the probability for soft hydrogel spheres in the mixture. This can be found both in experiments and simulations. Besides, in numerical simulations, the inter-species friction has an impact on the outflow rate.

For further investigations of granular flow dynamics, it would be interesting to investigate the evolution of the force chains and contact force network during the silo discharge.

4 The effect of an obstacle on silo discharge

In chapter 2, we find that soft grain ensembles exhibit quite different characteristics in silo discharge compared with hard particles. In that chapter, the temporary clogging or congestion can be dissolved spontaneously. One of the reasonable assumptions is that particles might pass through gaps of blocking arches above the orifice. An obstacle in front of the orifice can create that kind of gap.

Hard particles can form permanent clogs when the outlet of a silo is smaller than a certain size, which for spheres is approximately five times of sphere diameter [89, 90]. There are plenty of studies focusing on reducing the probability of clogging, such as expanding the orifice size [35], adjusting the number of outlets and distances between outlets [91, 92], or applying external vibration [93]. Another effective method of decreasing the probability of clogging is to place an obstacle inside the silo. The mechanics behind assume the reduction of pressure in the region of arch formation [57, 58]. The packing fraction at the orifice decreases when putting an obstacle in front of the outlet [94].

From another perspective, pedestrian motion in narrow passages at high population density shows some similarities with granular dynamics [95], such as intermittent dynamics when passing a bottleneck. Although all pedestrians have individual trajectories and destinations, their motion is principally influenced by repulsive interactions with other individuals at high population densities. This can lead to self-organized dynamics [96]. At very high density, pedestrians can organize in lanes, similar to segregation in granular media [97]. The behavior of pedestrians passing bottlenecks such as corridors or doors is in some respect analogous to granular flow in an hourglass [98]. Density is used as a critical parameter, closely related to pedestrian dynamics, but kinetic stress, i. e. the product of packing density and velocity fluctuations, is considered as another decisive factor leading to velocity changes towards the bottleneck [99]. If pedestrians stay in a confined, not too wide space, the density at a bottleneck will surprisingly reduce [100]. If there is an obstacle in front of the door, it can help alleviate the pressure in the area near the exit and decrease the probability of blocking the passage [101, 102]. However, an obstacle does not necessarily alter the pedestrian flow rate [103].

Soft granular materials combine the features of hard granular matter (such as clogging) and animate objects (such as deformability but incompressibility and high density of compaction). For hard granular material or pedestrians, an obstacle in front of the outlet has a more or less positive effect on outflow dynamics. So in this chapter, we explore the effect of an obstacle placed in front of a container outlet for soft, low-frictional hydrogel spheres and extract flow fields, local packing fraction, and the distribution of kinetic stress related to pressure in the vicinity of the outlet.

4.1 Experiments

The setup is the same as we used in chapter 2 and chapter 3. A setup sketch is shown in Fig 4.1. The obstacle is realized by a flat cylindrical magnet of 25mm diameter and 3mm thickness which is suspended inside the bin. It is held in place by a second magnet outside the bin. In this way, we avoid a suspension wire inside the silo but still keep the opportunity to change the obstacle position straightforwardly. The magnets are set above the center of the orifice. The height is defined by H labeled in Fig 4.1(b) describing the geometry near the obstacle with an outlet of the silo. D_0 is the diameter of the circular obstacle, d is the diameter of the spherical

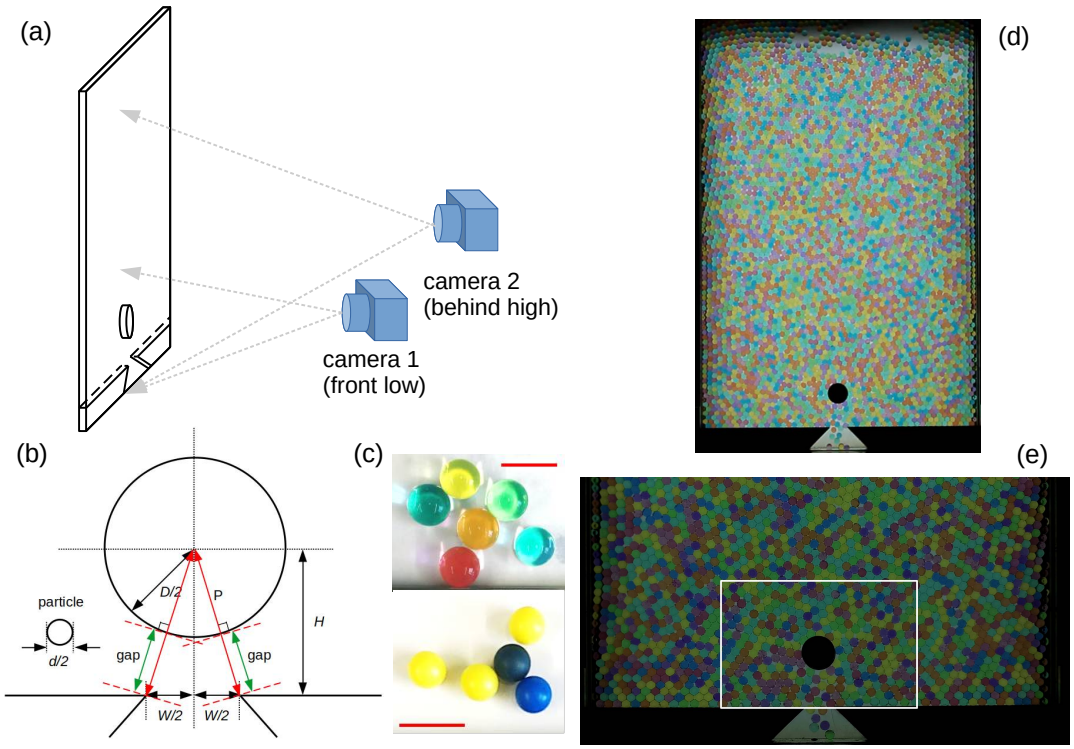

Figure 4.1: Sketch of the experimental setup. Two cameras in front of the setup capture the discharge process. Camera 2, sketched on the right, monitors the height change during the discharge with 60fps, and (d) shows one typical frame. Camera 1 is placed closer to the container and at a lower height to record a detailed view of the region near the outlet, (e) is a typical frame recorded with the faster camera 1. The white rectangle sketches the 768 $\times$ 512 pixel^2 area of interest, cropped from the original 1920 $\times$ 1080 pixel^2 frame. (b) sketches the geometry near the obstacle above the orifice. (c) shows the particles: the top ones are hydrogel spheres (HGS) with 7mm diameter, and below are the airsoft bullets (ASB) with 6mm diameter. Scale bars are 10mm. The image is reproduced from [104].

particles, and D is the width of the orifice in the silo. H is the height position of the obstacle. The width of the gaps between the obstacle and the edges of the orifice is given by

$$H' = \rho' d = \sqrt{H^2 + \left(\frac{D}{2}\right)^2} - \frac{D_0}{2}. \tag{4.1}$$

The process of silo discharge is recorded by two commercial cameras, see Fig 4.1(a). The front camera (*XiaoYi 4K+ Action*) focuses on the bottom area around the obstacle and captures videos with a frame rate of 120fps with a spatial resolution of 0.2mm per pixel. The second camera (*Canon EOS 600D*) is placed behind and above the front one and captures videos with a frame rate of 60fps to monitor the height changes in the silo during discharge. The white rectangle area will be the field of interest in our work.

The HGS particles used in this chapter are from a different manufacturer. The mean diameter of these HGS is 7mm, which varies by approximately 3%, and the elastic modulus of the particles is roughly 30kPa. In comparison, we used the same airsoft bullets(ASB) of $d = 6$mm diameter and a friction coefficient of approximately 0.3. The experimental parameters are listed in Tab 4.1.

4.2 Methods and results

The optimal way to extract the information on the outflow dynamics is to perform an instance segmentation of consecutive images of the particles in a silo, i. e. to find the shape of the region occupied by each particle. The positions of particles (their respective region centers) can then be tracked in time and assembled into trajectories, provided that the frame rate is sufficiently high and particles can only move in a short distance in two consecutive frames. Furthermore, the particle regions can provide additional information, e. g., the pressure field [105]. The Mask R-CNN artificial neural network is employed for instance segmentation in this study. This type of network is used in multiple applications where detection accuracy is required, especially for particles with complex shapes [106, 107]. For building up the training dataset, approximately 30 frames were manually annotated. Each frame contains 300 to 400 particles. Then the neural network of Mask R-CNN pre-trained on MS COCO image dataset [108] is trained by around 100 epochs on the augmented images.

As expected, even with a relatively small amount of training data, Mask R-CNN is good at detecting hard and soft round particles, shown in Fig. 4.2. This is due to the relative simplicity of the frames, where clear borders between the objects are present. The background is clean and the image contains only a low amount of visual noise.

4.2.1 Velocity

As all particles within every frame have been identified using a trained Mask R-CNN network, we utilize the *Python trackpy* package [109] to label and track all particles. From the trajectories of particles appearing in the image sequences, the displacement of each particle between successive frames can be determined. The time interval between the frames is the reciprocal $\frac{1}{f}$ of the frame rate f. The velocity of particle i at position $\vec{x}_i(t)$ is given by the equation of motion

$$\vec{v}_i(t) = \frac{d\vec{x}_i(t)}{dt} \tag{4.2}$$

Fig 4.3 shows trajectories of 12 selected particles as examples. White circle markers correspond to the initial positions of these particles. The colored lines are their paths toward the orifice of the silo. The main consequence of an obstacle in the global outflow dynamics is shown in Fig

Material	Orifice width W	ρ	ρ'	Height H
HGS	14 mm	2.0	0.9	17.5 mm
HGS	14 mm	2.0	2.3	27.5 mm
HGS	14 mm	2.0	3.7	37.5 mm
HGS	14 mm	2.0	-	-
HGS	21 mm	3.0	1.1	17.5 mm
HGS	21 mm	3.0	2.4	27.5 mm
HGS	21 mm	3.0	3.8	37.5 mm
HGS	21 mm	3.0	-	-
ASB	35 mm	5.8	4.8	37.5 mm
ASB	35 mm	5.8	-	-

Table 4.1: Experimental conditions: Materials, orifice widths W, ratio $\rho = W/d$, ratio $\rho' = H'/d$ and height H (H is the distance from the bottom edge of the obstacle to the orifice). Note: H' is the gap width

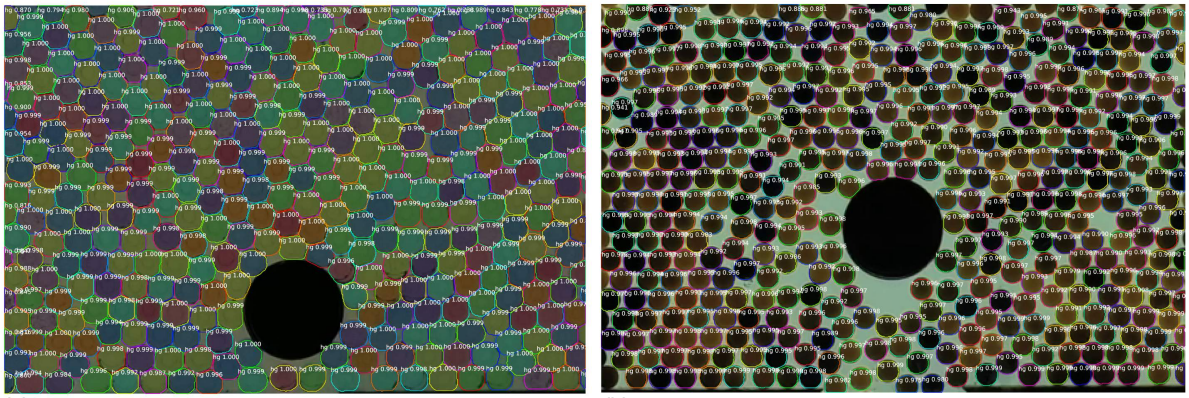

(a) (b)

Figure 4.2: Examples of automatic particle detection by our MASK R-CNN trained model: Detection of (a) all soft particles, and (b) all hard particles in typical frames, by the same network. The image is reproduced from [104].

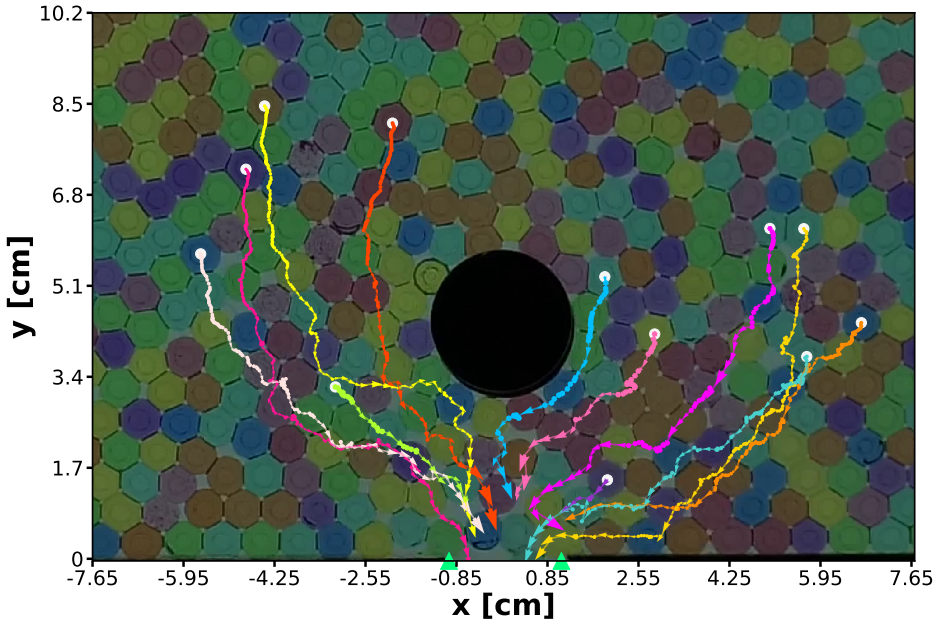

Figure 4.3: Trajectories of selected HGS particles. The image is reproduced from [104].

4.4. It compares the mass discharge rate of silos with two different orifice widths W and different heights H. All silos start with closely the same initial masses of about 1.5kg (60cm filling height). It is seen that placing an obstacle in front of the orifice has significant consequences when it is placed closer to the orifice. Two effects have to be considered: First, when the gap width ρ' becomes small enough, it forms a bottleneck for the discharge. Second, for the soft grains, a lower pressure near the orifice retards the discharge and leads to clogging at the orifice. When the obstacle is close enough, directly above the orifice, the pressure below the obstacle is reduced and the behavior of particles tends to be like rigid particles, thus discharging more slowly and clogging often. The silo does not empty in the end. This is indicated by Fig 4.4 at different plateau levels in the graph. Here, 100g material corresponds to an average filling height of 4cm. Note that the experiments are stopped when clogs last for more than 30s.

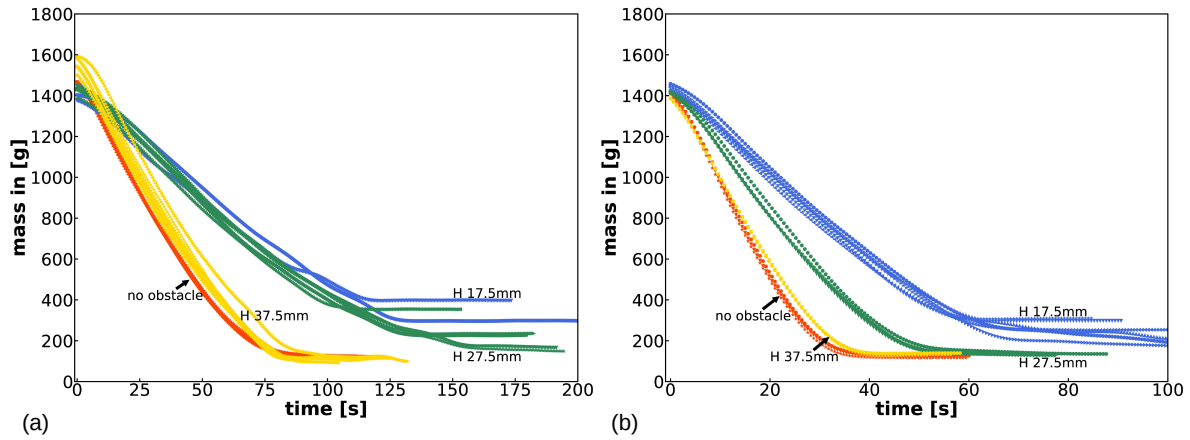

Figure 4.4: (a) HGS Mass remaining in the silo with (a) $W = 14$mm and (b) $W = 21$mm orifice widths. Some graphs reach plateaus when the silo discharge stops before it is emptied. Initially, the silos are filled to a height of approximately 60cm. The image is reproduced from [104].

At the lowest position, where $\rho^{'}$ is around 1 (or even lower than the original particle diameter), the outflow still goes on as long as the filling height is sufficient. The pressure squeezes the particles through the gaps even when $\rho^{'} < 1$. This is remarkable because when ρ is well below 2 in a silo without obstacles, clogging would be set much earlier at the bottom. In the presence of the obstacle near the orifice, when the silo is partially empty where the pressure at the bottom drops, particles get clogged at the lateral gaps, and the area below the orifice is then free of material, see Fig 4.5(a),(b). When the obstacle is placed further away from the orifice, and ρ' is comparable to or larger than ρ, it can be seen in Fig 4.5(c) that the nearly spherical appearance of HGS below the obstacle is exposed to small forces only, in contrast to the particles at orifice left and right sides of the outlet.

Fig 4.6(a) and (b) show the velocity field for soft HGS in the region near the orifices of different widths, in the case of the obstacle at a fixed height of $H = 37.5$mm ($\rho' \approx 3.7$). For comparison, Fig 4.6(c) shows the velocity field of an ensemble of hard ASB, with a much wider orifice width. We can observe triangular areas at both bottom corners, where the hard frictional ASB particles hardly move. Directly above the obstacle, particles slow down and almost come to rest. It is impossible to directly compare the hard and soft sphere experiments because of the different orifice sizes. When hard grains are observed with smaller orifice widths, there is no continuous flow because of frequent clogging. When soft grains are observed with larger orifice sizes, the packing fraction is no longer uniform. Empty holes are formed and propagate upward while particles are in free fall in these regions. The reduced flow rate for soft grains

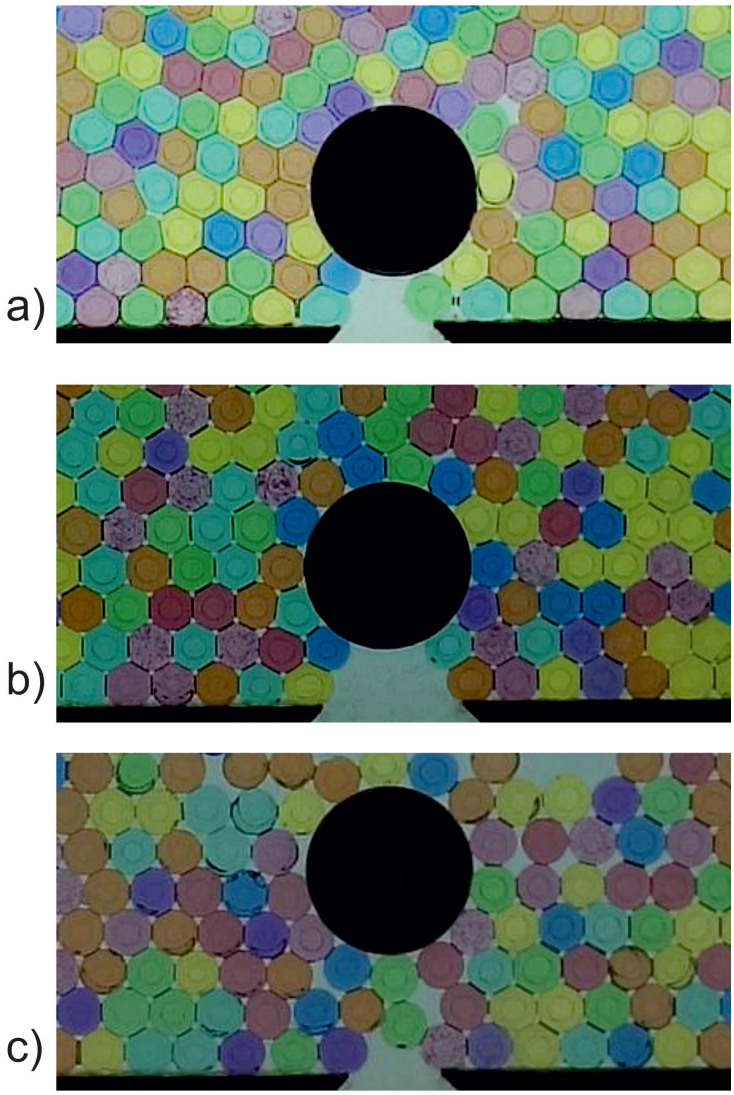

Figure 4.5: Long lasting (or possibly permanent) clogged states of HGS in presence of an obstacle above the orifice, (a) $D = 14$mm ($\rho = 2$), $H = 17.5$mm ($\rho' = 0.9$), (b) $D = 21$mm ($\rho = 3$), $D = 17.5$mm ($\rho' = 1.1$), and (c) $D = 14$mm ($\rho = 2$), $D = 27.5$mm ($\rho' = 2.3$). The image is reproduced from [104].

near the obstacle, compared to hard grains, can be attributed to the narrower orifice that acts as a bottleneck for the outflow. Since the orifice width D is much larger for ASB, the bottleneck effect is much less pronounced.

Fig 4.7 shows the velocity field in the silo with orifice $D = 2d = 14$mm and the obstacle at different heights above the orifice. Compared with the case of no obstacle shown in Fig 4.7(d), the velocities near the orifice are systematically lower with an obstacle. When the obstacle height reaches 37.5mm (Fig 4.7(c), $\rho' \approx 3.7$), the velocity directly above the orifice has practically reached the same value no matter if there is an obstacle present or not. With obstacles, the flow profile is broadened and extends more toward the side walls. Fig 4.8 presents the velocity map in the silo with orifice $D = 21$mm ($D = 3d$) and the obstacle placed at different heights. In general, when the orifice is wider (by one particle diameter, as shown in Fig 4.7), particles can flow out more smoothly, leading to a maximum velocity. Even at the lowest obstacle height of 17.5mm, the outflow through a larger orifice is faster because of the slightly larger gap width ρ' (compare Fig 4.7(a) and Fig 4.8(a)).

The mean vertical velocity of particles leaving the silo is plotted in Fig 4.9. It demonstrates

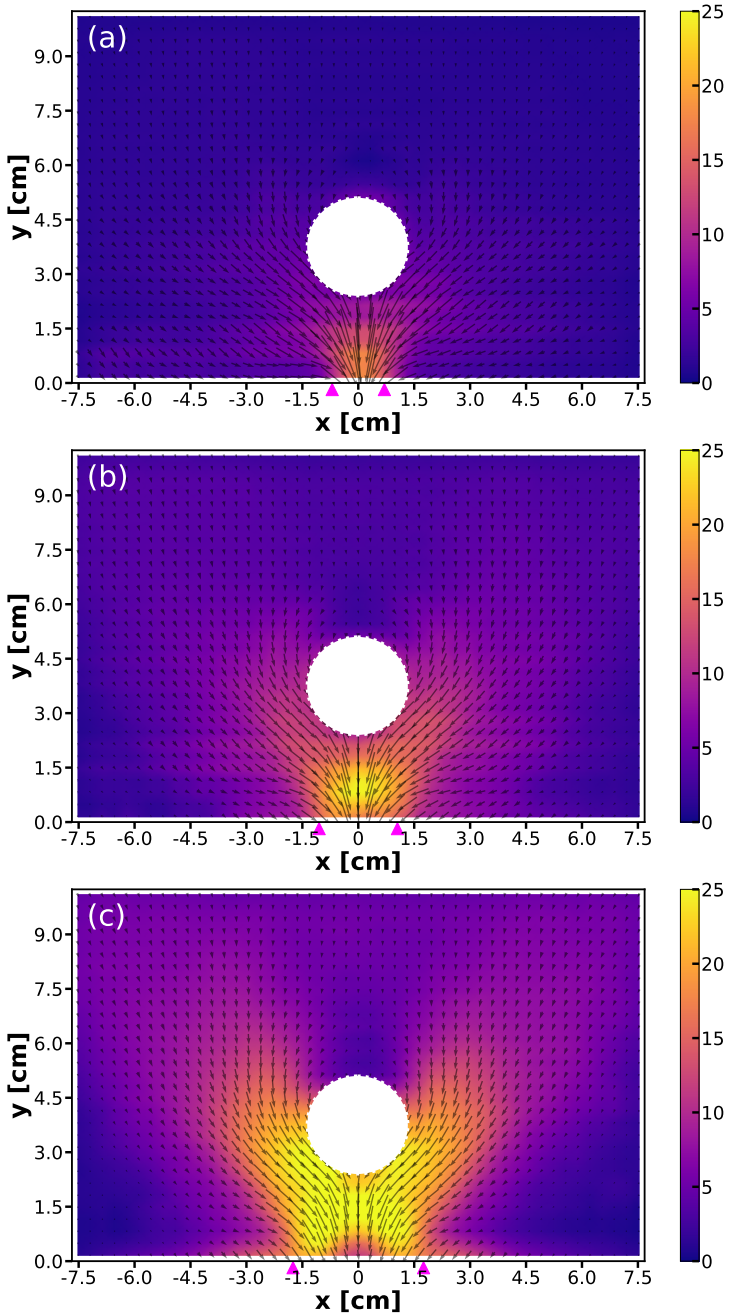

Figure 4.6: Velocity fields in a silo with an obstacle at height $H = 37.5$mm. (a) HGS, orifice width $W = 14$mm, (b) HGS, $D = 21$mm, (c) ASB $D = 35$mm ($D \approx 5.8d$). The velocity fields are averaged over a time when the silo empties from half to quarter filling. Color bars represent the velocity in units of cm/s. The image is reproduced from [104].

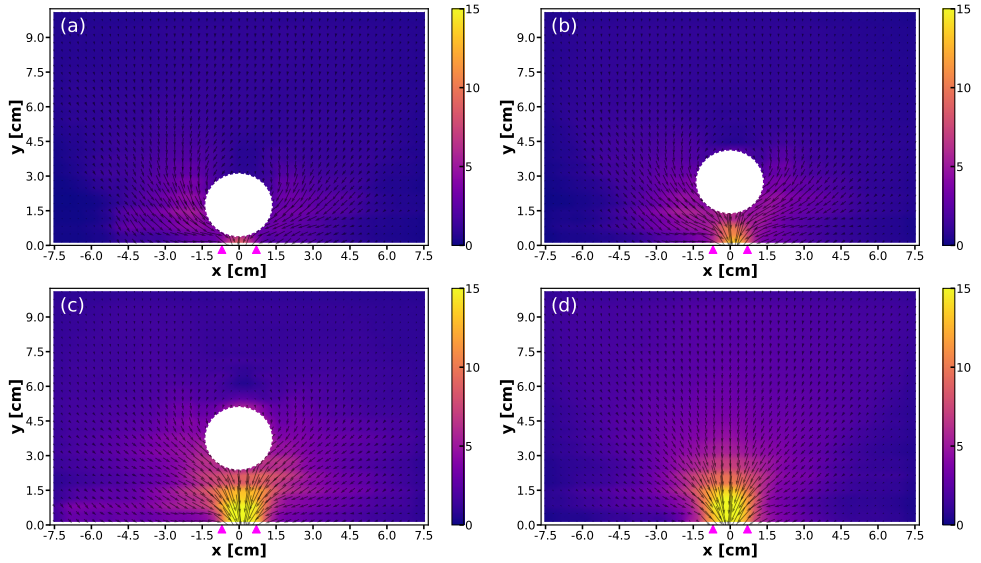

Figure 4.7: Velocity fields of HGS in the silo at $D = 14$mm orifice width with an obstacle at height of (a) $H = 17.5$mm, (b) $H = 27.5$mm and (c) $H = 37.5$mm. (d) shows the velocity field in the absence of an obstacle. The velocities are time averaged over time where the silo discharges from half-filled to quarter-filled. Color bars indicate the velocities (in units of cm/s). The image is reproduced from [104].

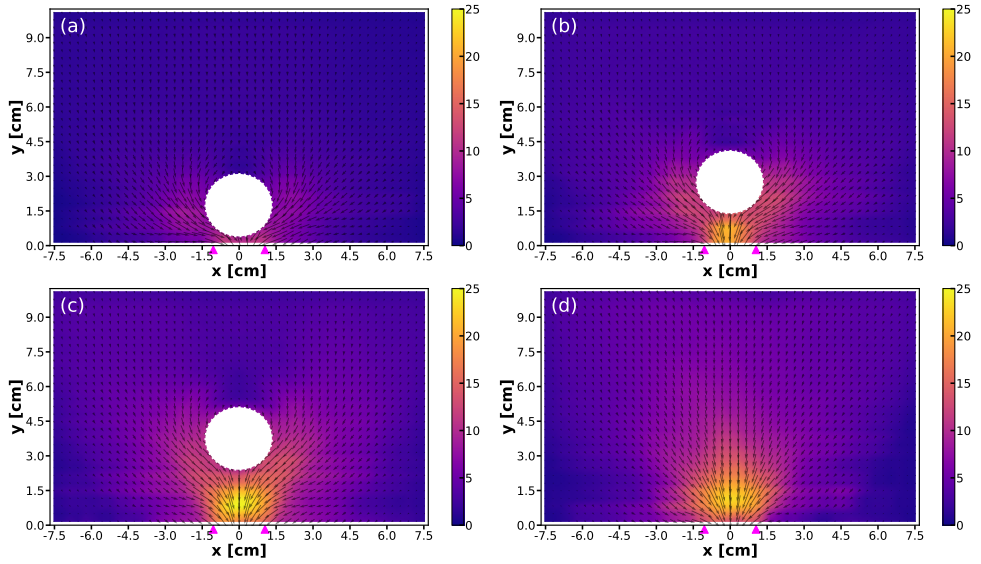

Figure 4.8: Velocity fields of HGS in the silo at $D = 21$mm orifice width with an obstacle at height of (a) $H = 17.5$mm, (b) $H = 27.5$mm and (c) $H = 37.5$mm. (d) shows the velocity field in the absence of an obstacle. The velocities are time averaged over time when the silo discharges from half-filled to quarter-filled. Color bars indicate the velocities (in units of cm/s). The image is reproduced from [104].

that the outflow rates are the same with different orifice sizes when the obstacle is in the highest position ($\rho' \approx 3.7$) above the orifice. In the case of lower positions of the obstacle, the outflow velocity of the soft grains is affected significantly, especially for the obstacle height of 27.5mm where the gap width ρ' of the two other orifice sizes is still larger than the orifice at the bottom. The primary cause for the reduced outflow velocity is a lower pressure on the spheres.

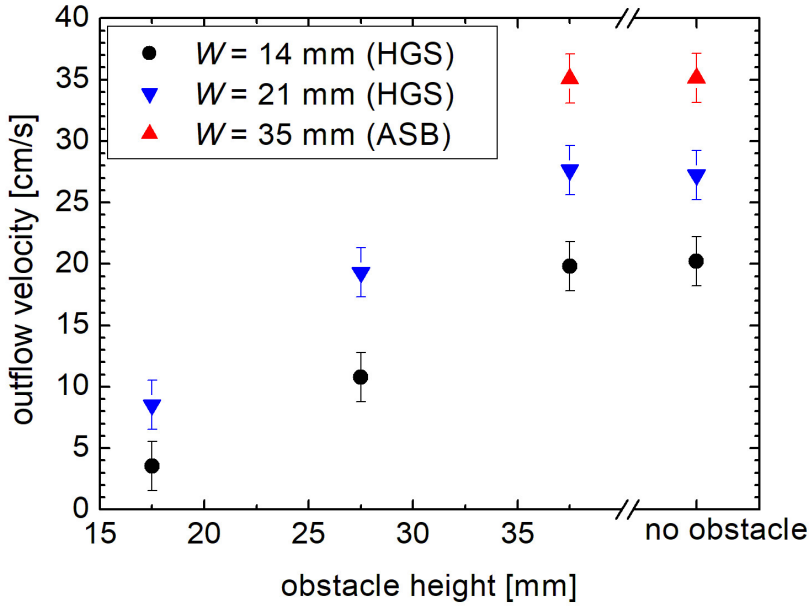

Figure 4.9: Time-averaged velocity of particles leaving the orifice in the center (±6mm). The rightmost symbols were measured in the absence of an obstacle. The image is reproduced from [104].

4.2.2 Escape time

The escape time map measures the expected time for a particle initially positioned in a location (x, y) to reach the orifice. We restrict the period between half and quarter filling of the container while the view captures focus in the region of the bottom of the silo (see white rectangle in Fig 4.1(e)). We distinguish 2 types of grains: those that reach the orifice in the evaluation period and others that do not. For the former ones, it is straightforward to construct an escape time map, because their initial position and the time until the particle exits the container can be directly measured. However, if only these particles were considered, the number of particles contributing to an average escape time decreases with increasing distance to the outlet, increasing the statistical error. Thus, we adopt a two-step procedure to calculate the full escape time map.

First, we augment the particle trajectories with additional information: We first retrieve information from each trajectory of particles: the time until the end of the trajectory, the distance to the midpoint of the orifice, the distance of the trajectory, and the time of the last point of the trajectory. Then, we sort out particles that reach the orifice. Here, the escape time at each point for particles is immediately known by counting the frames of each trajectory. For the other particles that don't reach the orifice during that time, we calculate an expected evacuation time based on the statistics of the previous data: we define a small range of distances for searching particles reaching the orifice that is close to the ending points (x_e, y_e) of these particles not reaching the orifice. The extended time is averaged from those particles reaching the orifice,

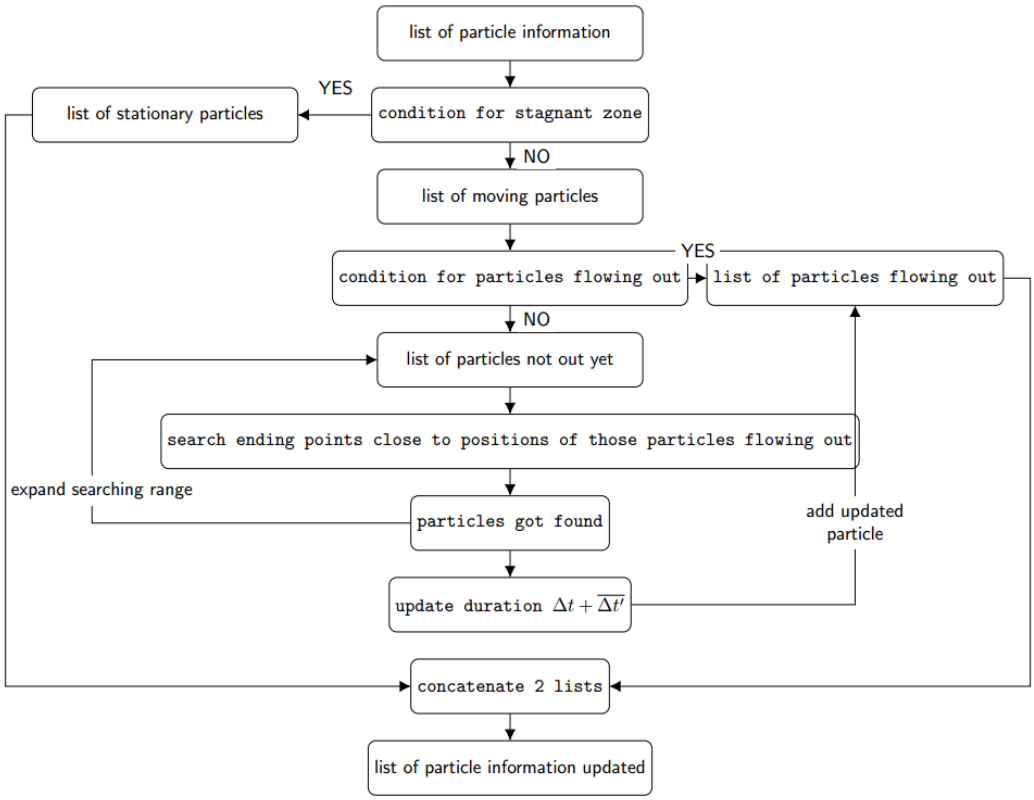

Figure 4.10: Flowchart for the calculation of the escape time. The image is reproduced from [104].

giving a value $t_e(x_e, y_e)$. To obtain the completed time for those particles not reaching the exit, we add t_e to the duration of trajectories of those particles not reaching the exit. The flowchart of this calculation is shown in Fig 4.10.

The spatial distribution of escape times can be a decisive parameter in silo discharge. Averaged escape times of particles in a given starting position are presented in Fig 4.11 for different orifice widths and materials at a fixed obstacle position. In Fig 4.11(c), the two bottom corners in red indicate the transition to the stagnant zones of hard particles. In all cases, the escape times of particles starting behind the obstacle are retarded concerning particles at the same height above the obstacle. To be noted, the retardation is much more pronounced for the hard grains (see in Fig 4.11(c)) than for the soft grains (see in Fig 4.11(a),(b)).

Fig 4.12 and Fig 4.13 visualize the influence of the obstacle position. Compared to the situation without an obstacle shown in subfigure (d), the obstacle in the highest position (c) supports a faster escape of particles at the two sides, by blocking the central downflow. It thus leads to smaller escape time gradients along the width of the silo. It can be speculated that this effect of smoothing out the distribution of the escape time by a relative distance from the obstacle could be beneficial for the escape dynamics: even if the average escape time does not decrease in the presence of the obstacle, there are no particular 'danger zones' from which they would not escape in time, even if their initial distance to the orifice is similar to the others. However, placing the obstacle near the orifice leads to an overall increase in the escape time (note the different scales in Fig 4.12 and Fig 4.13).

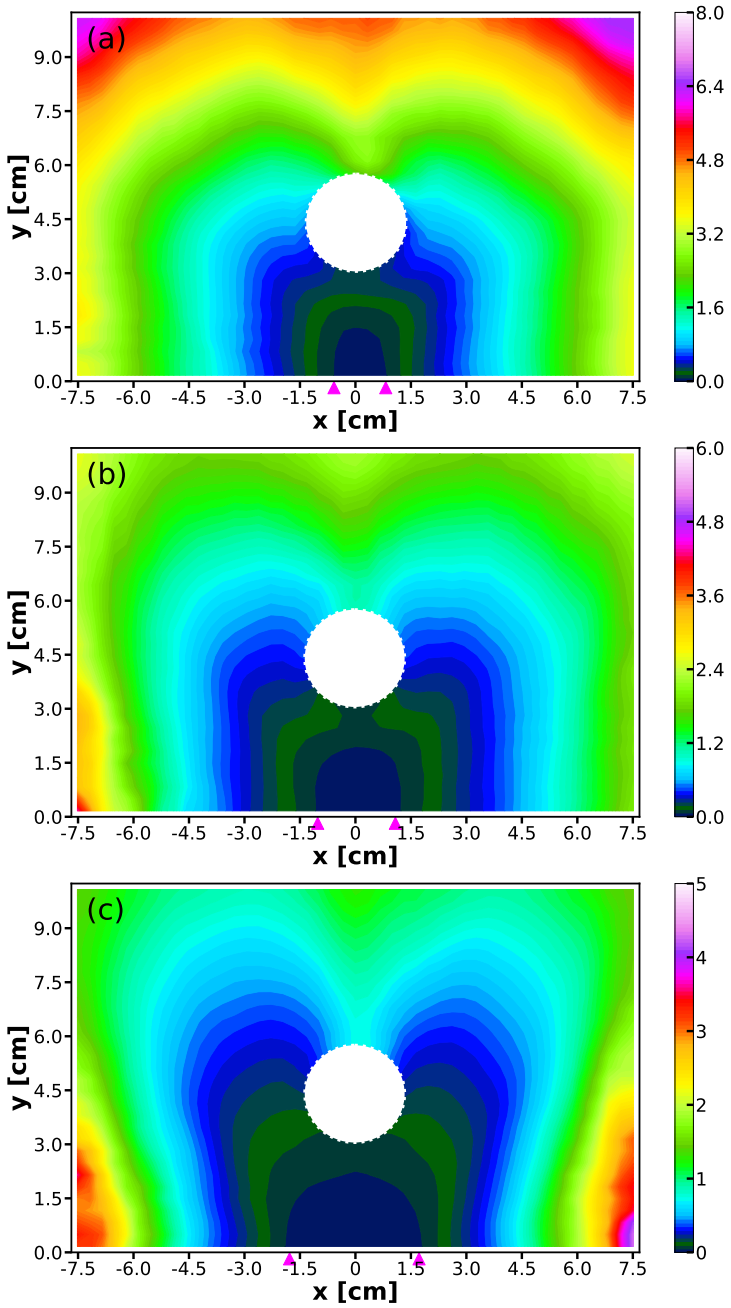

Figure 4.11: Distribution of escape times in a silo with an obstacle at a height of 37.5 mm. (a) HGS with $D = 14$mm, (b) HGS with $D = 21$mm, (c) ASB with $D = 35$mm. Escape times were averaged over the period where the silo emptied from half to quarter filling. The color bars give time in seconds. The image is reproduced from [104].

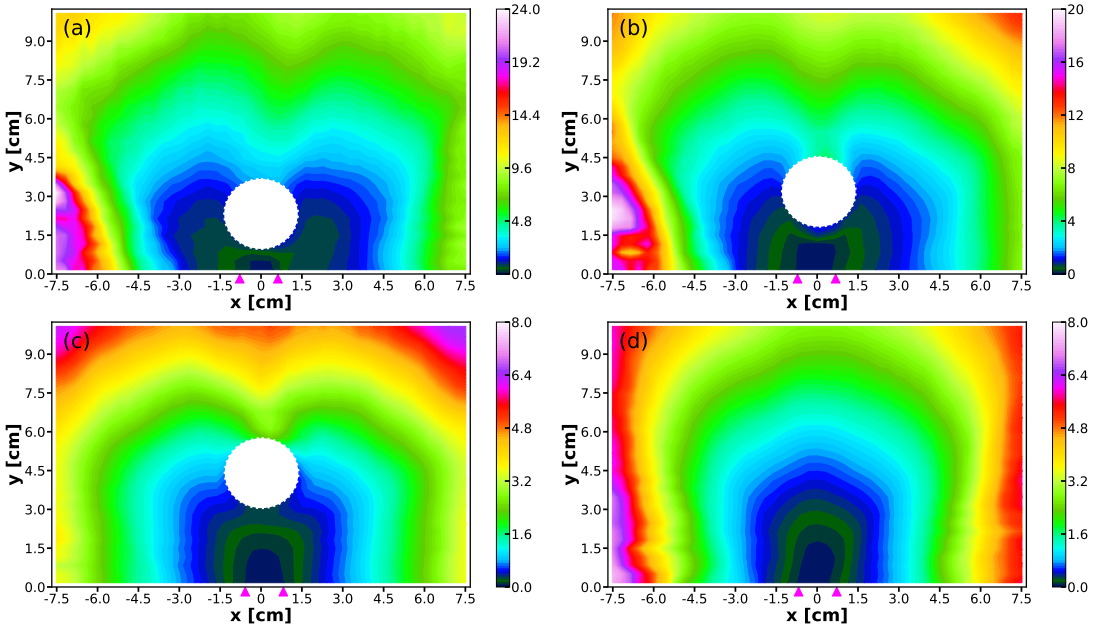

Figure 4.12: Distribution of escape times of HGS in the silo of $D = 14$mm orifice width with an obstacle at heights of (a) $H = 17.5$mm, (b) 27.5mm, and (c) 37.5mm. (d) shows the escape times when the obstacle is absent. The escape times are averaged over the period where the silo was emptied from one-half to one-quarter. The color bar gives the time in seconds. The image is reproduced from [104].

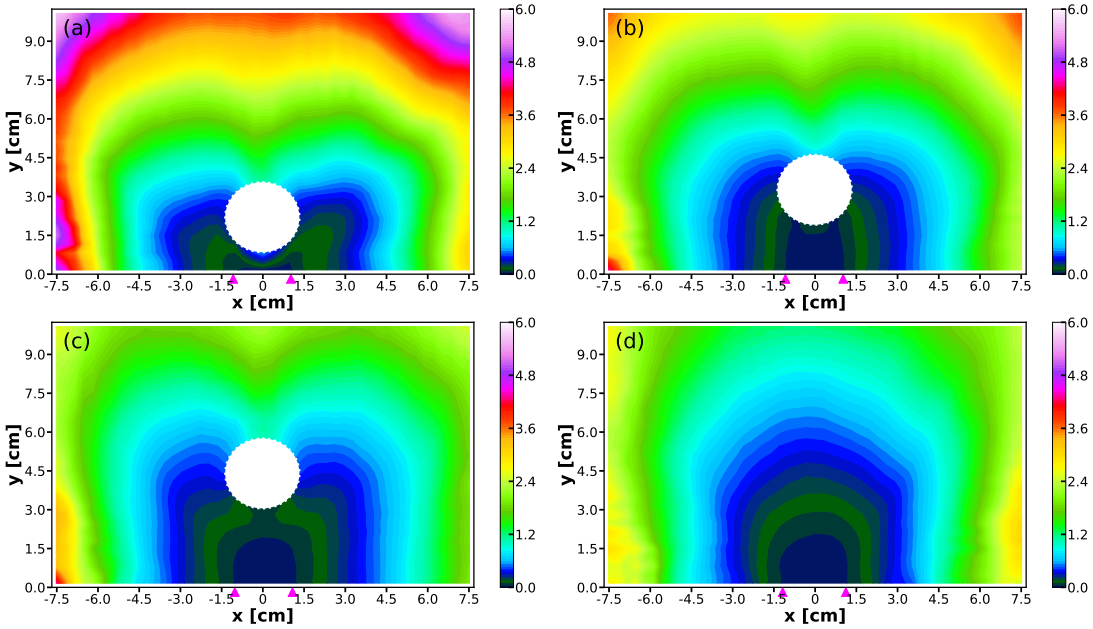

Figure 4.13: Distribution of escape times of HGS in the silo of $D = 21$mm orifice width with an obstacle at heights of (a) $H = 17.5$mm, (b) 27.5mm, and (c) 37.5mm. (d) shows the escape times when the obstacle is absent. The escape times are averaged over the period where the silo was emptied from one-half to one-quarter. The color bar gives the time in seconds. The image is reproduced from [104].

4.2.3 Local packing fraction

The method of Voronoi diagrams [110] has been adopted to quantify the local packing fraction of soft particles. In our case, we have determined the centers of each particle in each frame shown in Fig 4.14(a) as seeds. Voronoi cells are calculated correspondingly as shown in Fig 4.14(b). Since the depth of the silo is fixed, given by the diameter d of particles, the Voronoi cell volume is defined as the area of a Voronoi cell A_V multiplied by the silo depth W. The volume of each particle is $\frac{\pi d^3}{6}$. Then, the local 3D packing fraction in the cell is given by

$$\phi = \frac{6A_V}{\pi d^2}. \tag{4.3}$$

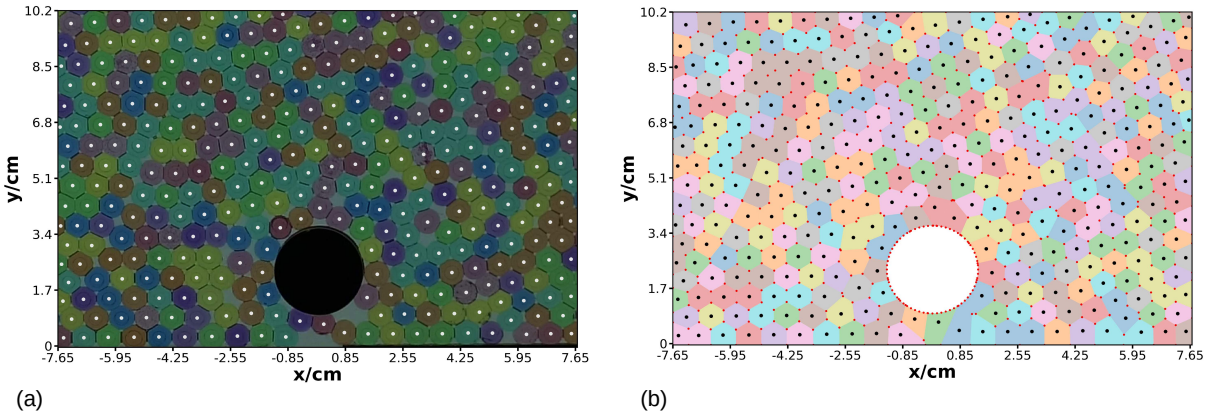

Figure 4.14: (a) location of centers of each particle in one frame randomly selected. (b) Voronoi cell for each particle in the corresponding frame. The image is reproduced from [104].

Local packing fractions are shown in Fig 4.15 for a fixed obstacle height of 37.5mm. In all these plots, the packing fraction appears to be reduced in the first bottom layer. Indeed, the packing fraction at the borders decreases continuously toward the walls because the first layer leaves gaps at the bottom, see Fig 4.16. Also because our bottom boundary is flat and the Voronoi cells at the bottom are mostly pentagons instead of hexagons, enlarging the areas of Voronoi cells is unavoidable even if the particles at the bottom suffer a lot of deformation. Because the soft spheres can be deformed to a more or less hexagonal cross-section in the cell plane, their local packing can be much more efficient than that of the ASB. This causes the denser packing in Fig 4.15(a), (b). Towards the opening of the silo, a crescent-shaped zone of reduced packing fraction is seen in all figures.

Figs 4.16 and 4.17 present the local packing fractions in the silos with 14mm and 21mm orifice width, respectively. The packing of the region directly above the orifice is nearly identical whether there is an obstacle at a height of $H = 37.5$mm or there isn't an obstacle. However, when the obstacle is placed at lower heights, it influences the packing fraction above the orifice. Together with the reduced pressure above the orifice, this leads to lower discharge rates(seen in Fig 4.3 and 4.4). Note that the packing fraction in the whole container increases systematically when the obstacle is placed very close to the orifice.

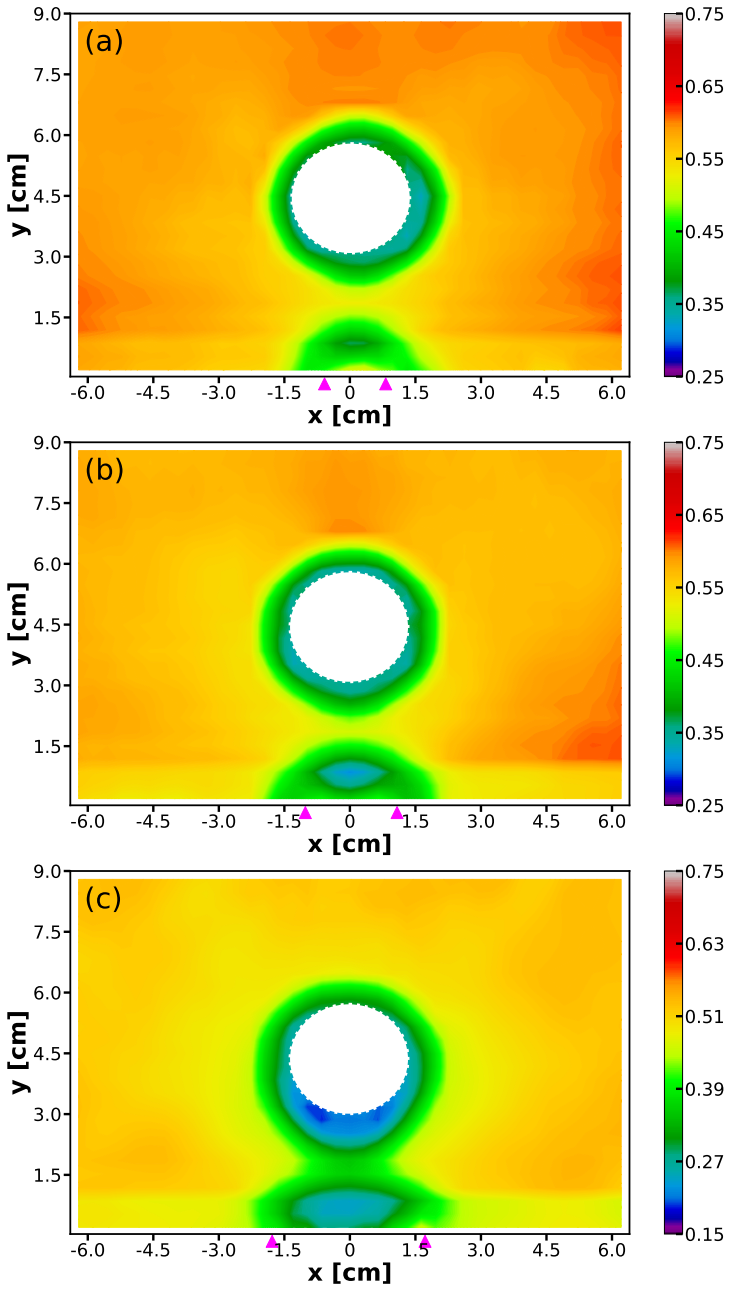

Figure 4.15: Local 3D packing fractions of HGS for (a) $D = 14$mm and (b) $D = 21$mm. (c) local packing fraction of ASB at $W = 35$mm. The obstacle is at height $H = 37.5$mm. Data is time averaged over a period from half-filled to quarter-filled silo. The image is reproduced from [104].

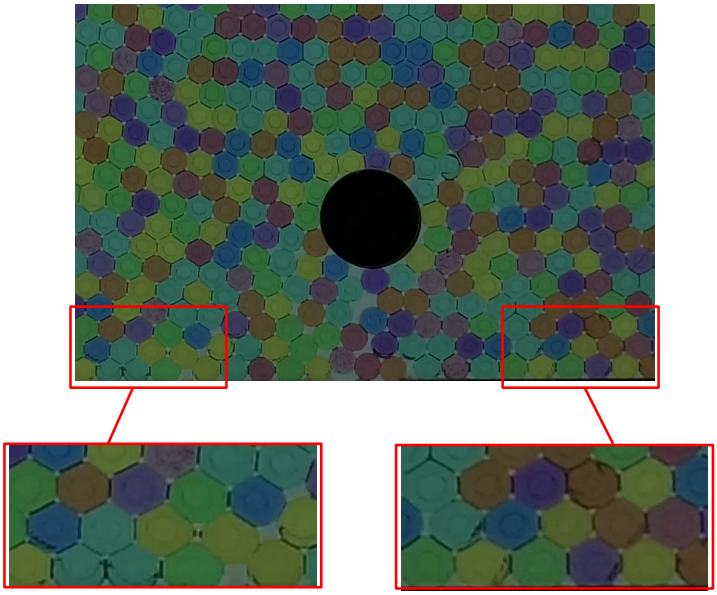

Figure 4.16: Zoomed bottom layer of HGS for $D = 14$mm and $H = 37.5$mm. The image is reproduced from [104].

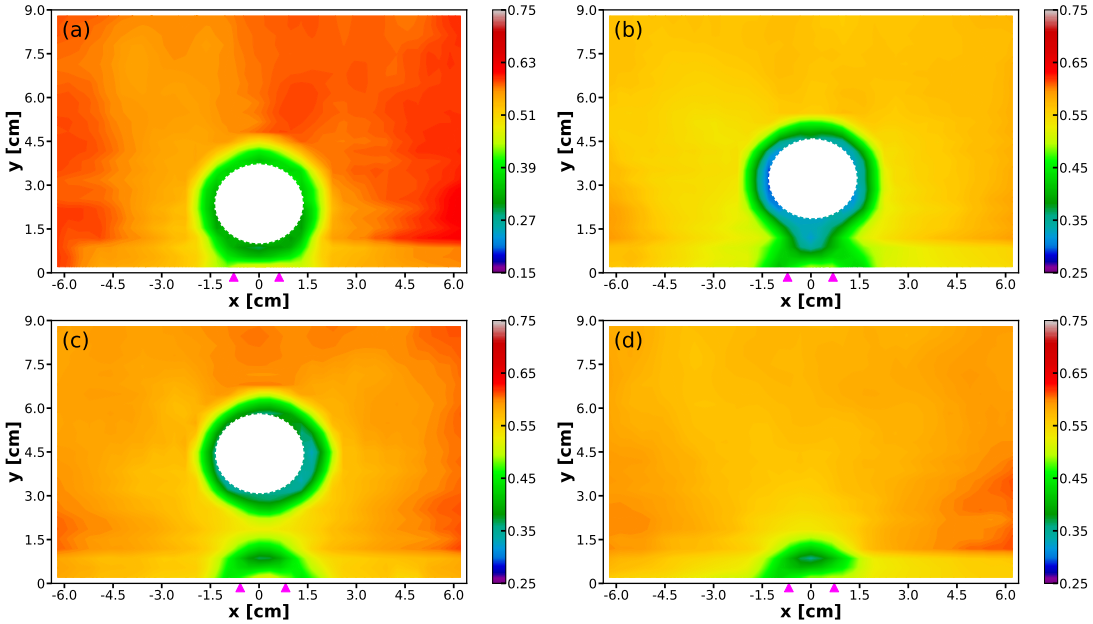

Figure 4.17: Local packing fractions of HGS in the silo of $D = 14$mm orifice with the obstacles at heights (a) 17.5mm (b) 27.5mm and (c) 37.5mm, (d) shows the situation without obstacle. Packing is averaged over a discharge period from the half-filled to the quarter-filled silo. The image is reproduced from [104].

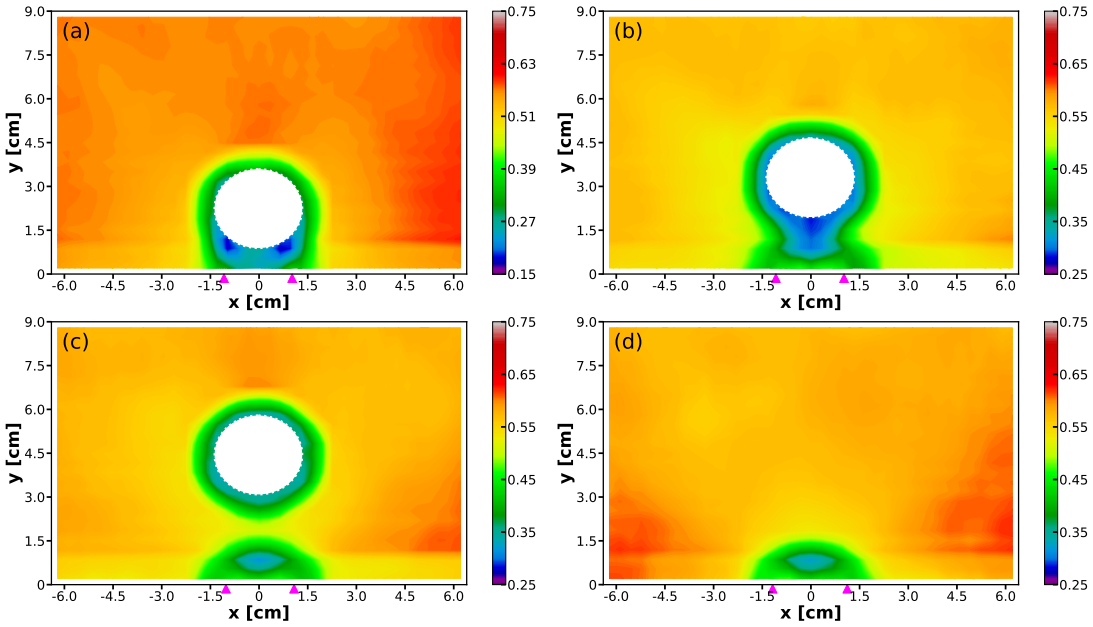

Figure 4.18: Local packing fractions of HGS in the silo of $D = 21$mm orifice with the obstacles at heights (a) 17.5mm (b) 27.5mm and (c) 37.5mm, (d) shows the situation without obstacle. Packing is averaged over a discharge period from the half-filled to the quarter-filled silo. The image is reproduced from [104].

4.2.4 Kinetic stress

The decrease of the local packing fraction near the orifice with the presence of the obstacle leads to the question of whether an obstacle induces a reduction in the magnitude of pressure at the bottom and stress between the particles. With the present setup, we are unable to measure the pressure directly. But we can observe a clear pressure reduction below the obstacle: the particle shapes are rather spherical, indicating little or no external stress.

Previous studies [111–113] use the kinetic stress as a meaningful measurement of the transient "crowd pressure" in the dense flow, which can be directly extracted from the particle trajectories and packing fractions. It is attributed to the stress tensor related to the local averaged fluctuation in the velocity and the local packing fraction. We deal with the dense flow in our experiments, but we can't get enough information from the experiments of instant stresses on each particle. Thus, traditional transient kinetic stress is not practical in our case. Instead, a time-averaged kinetic stress $\overline{\sigma_k}$ at position $\mathbf{x}$ was computed by

$$\overline{\sigma_k}(\mathbf{x}) = \overline{\phi(\mathbf{x},\mathbf{t})} \cdot \overline{[\mathbf{v}(\mathbf{x},t) - \mathbf{U}(\mathbf{x})]^2} \tag{4.4}$$

where the second factor represents the variance of the velocity, and $\mathbf{U}(\mathbf{x})$ is the local time-averaged velocity. Time averaging is performed over a period where the flow can be considered quasi-stationary. Since the first factor is constant in time, averaging over several frames was simply used to minimize the statistical error. In our case, fluctuations of the particle velocities can reflect collisions between particles especially near the orifice because of less density. However, in denser regions, the fluctuations usually result from dynamic rearrangements in the packing.

In Fig 4.19, immediately below the obstacle, the kinetic stress of soft particles is not as strong as for the hard grains. The lower kinetic stress is in the regions towards the bottom corners due to the lack of particle motion. The kinetic stress is lowered for both types of material directly above the obstacle where the flow is nearly stopped.

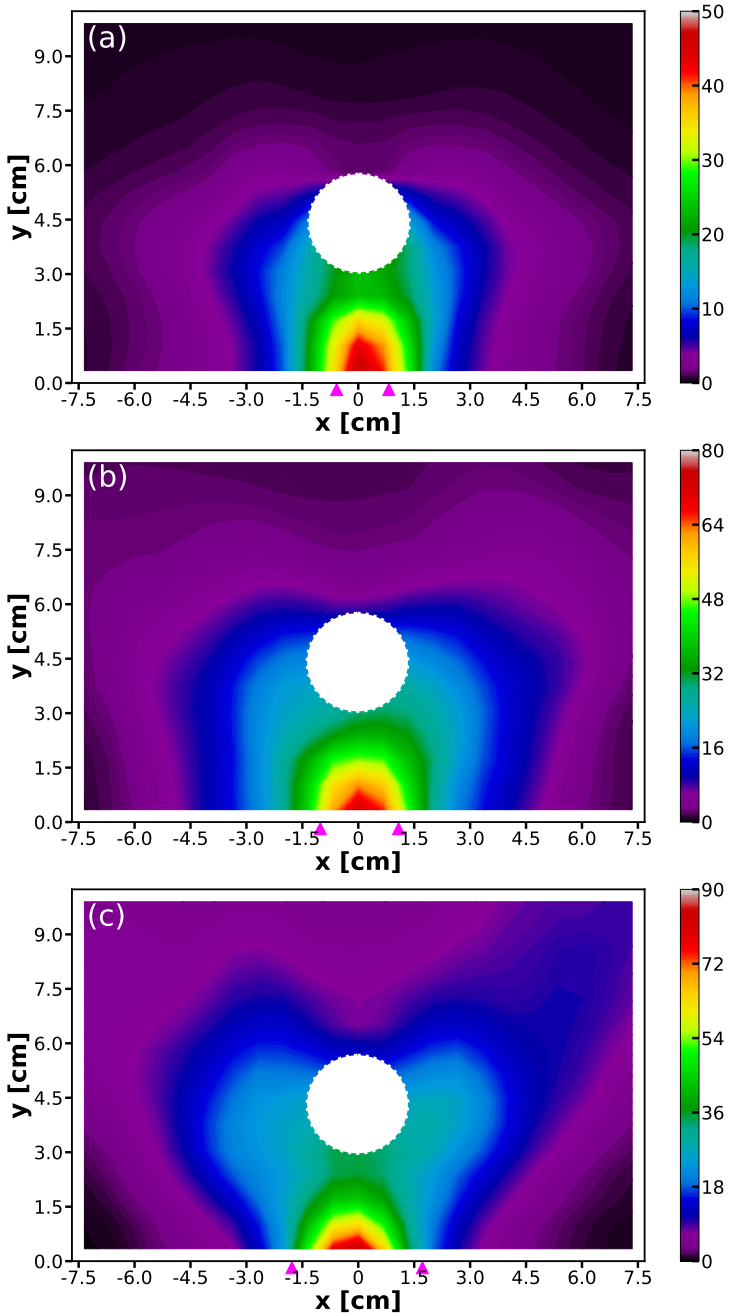

Figure 4.19: Kinetic stress of HGS in the silo with the obstacle at height 37.5mm for (a) $D = 14$mm and (b) $D = 21$mm orifice width. (c) Same for ASB at $D = 35$mm orifice width. Data are averaged over the discharge from one-half to one-quarter filling. Color bars give the kinetic stress in $(\text{cm/s})^2$. The image is reproduced from [104].

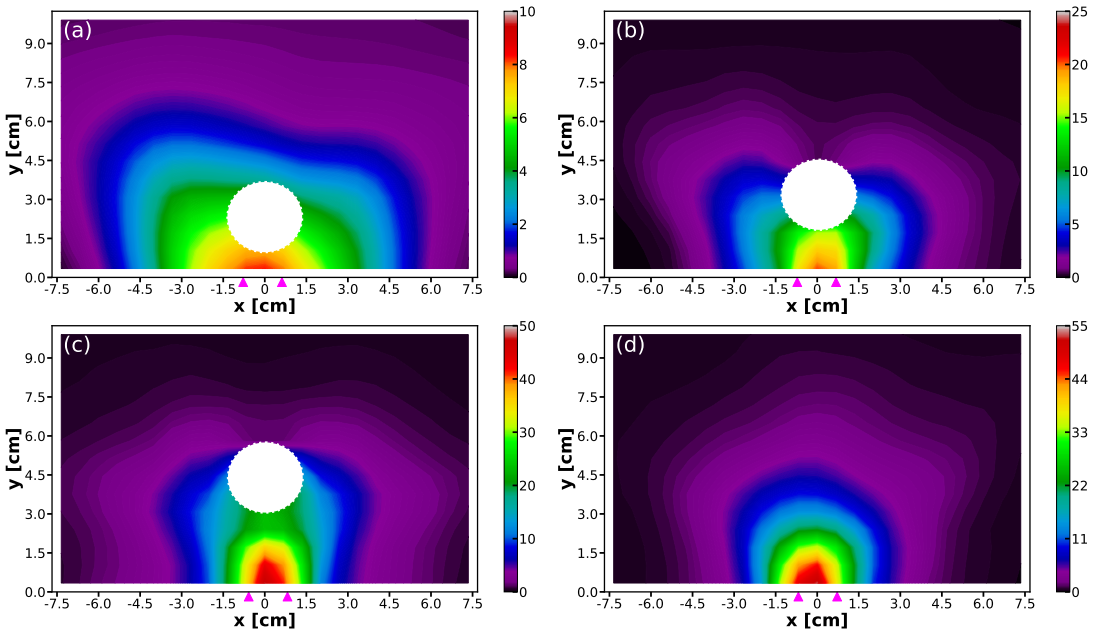

Figure 4.20: Kinetic stress distribution of HGS in a silo with fixed $D = 14$mm orifice width and an obstacle at heights (a) $H = 17.5$mm, (b) HGS and $H = 27.5$mm, and (c) HGS and $H = 37.5$mm. (d) shows the situation without obstacles. The kinetic stress is time averaged over the discharge from the half-filled to the quarter-filled silo, units are $(\text{cm/s})^2$. The image is reproduced from [104].

In all cases analyzed in the study, the kinetic stress is largest in the vicinity of the orifice. Packing densities are very low here, and velocity fluctuations resulting from the actual outflow velocities of individual particles are affected by collisions and by their dynamics upon leaving more dense regions. The magnitude of kinetic stress increases with increasing discharge rate when the obstacle is placed in a higher position(see Fig 4.20(c) and Fig 4.21(c)) or when the orifice size is increased (see Fig 4.19(a) and (b)). The local packing fraction is lowest there (Fig 4.15). Thus, the data reflect mainly the second factor of velocity fluctuations in Equation 4.4. Also in Fig 4.20 and 4.21, the gradient of the kinetic stress distribution resembles that of the distribution of escape time but points in the opposite direction.

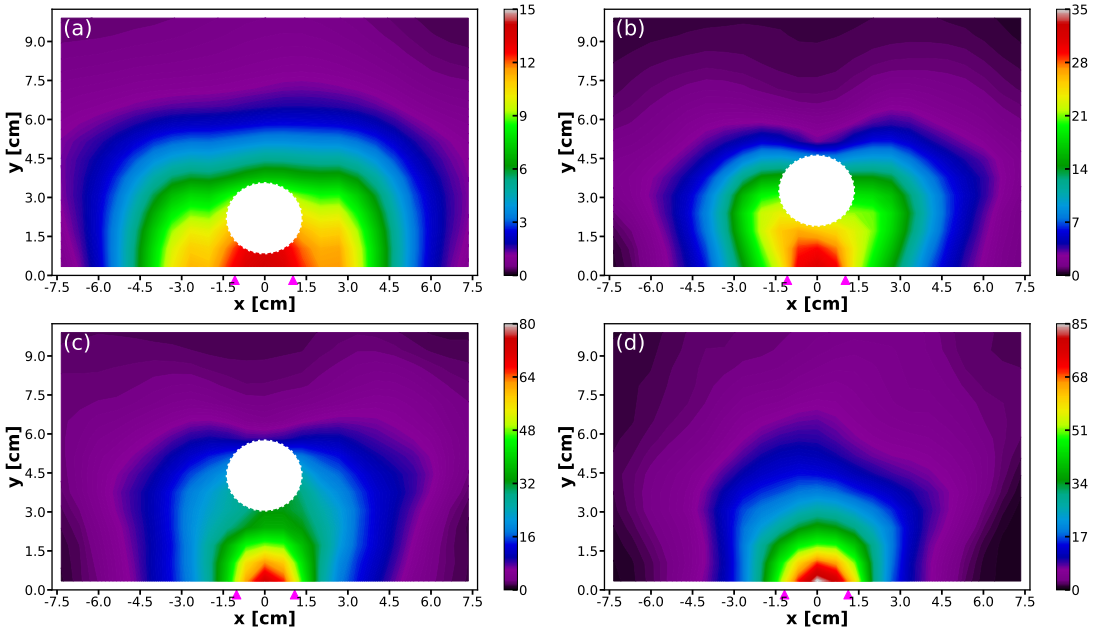

Figure 4.21: Kinetic stress distribution of HGS in a silo with fixed $D = 21$mm orifice width and an obstacle at heights (a) $H = 17.5$mm, (b) HGS and $H = 27.5$mm, and (c) HGS and $H = 37.5$mm. (d) shows the situation without obstacles. The kinetic stress is time averaged over the discharge from the half-filled to the quarter-filled silo, units are $(\text{cm/s})^2$. The image is reproduced from [104].

4.3 Discussions

In this chapter of the thesis, we discussed the effect of an obstacle in front of the orifice on the silo discharge of elastic frictionless spheres. It has been systematically analyzed regarding principle effects on velocities, escape times, granular packing fractions, and kinetic stresses. First, no 'faster-is-slower' effect of obstacles is observed in this study. In contrast, an obstacle slows down the velocities of particles to flow out because the pressure surrounding the obstacle near the orifice is reduced compared with the bottom orifice region without the obstacle. When the obstacle is close enough to the orifice, it reduces the discharge rate of the particles. Besides, the obstacle can induce clogging where it would not occur in the absence of an obstacle. 2 effects can lead to clogging when the obstacle is present: first, when the gaps between the obstacle borders and the edges of the orifice become smaller than the orifice width, clogs can form in these gaps, blocking the outflow completely. However, if just one of the gaps is blocked, the clog may resolve when the outflow continues going through the opposite gap. Thus, in these cases, one can always find long-persistent but non-permanent clogs (lasting at least several seconds or even longer). Second, if the gap between the obstacle and outlet edge is larger than the orifice width D and $D = 2d$, clogs are found at the orifice even though they might not be expected without an obstacle. The obstacle screens the particles below, at least partially, which can be seen in Fig 4.5. HGS particles below the obstacle appear nearly circular while they are squeezed to near hexagons in the regions above the obstacle. This reflects the idea in previous chapters that the discharge of soft elastic grains is pressure-dependent. Interestingly, one minor effect is observed that the particles at corners possibly flow out because the escape time in the region at corners near the bottom deduces when the center of an obstacle is placed at about 4 times the diameter of the particle higher than the orifice.

5 Detection of the shear zones in soft grain beds with an MRI method

The behavior resulting from the shear stress of granular matter is different from the liquid. The shear in Newtonian fluids is uniformly distributed. However, granular matter develops shear bands. The geometry of shear bands depends on the granular properties. Thus, it would be interesting to characterize the grain displacements inside a sheared granular bed because it tends to reduce the packing fraction in shear zones, which is described by Reynolds [114]. To obtain the complete displacement profile by locating the positions of the particles when shearing the sample, a tomographic imaging method plus a method of labeling particles in the sample can be applied. For transparent material, one can use optical fluorescence, which is affordable and simpler, imaging with a laser sheet [115, 116]. The material has to be submersed in a refractive index matching fluid, and this may influence the bulk shear characteristics. Another imaging technique is X-ray Computed Tomography (CT). Scanners are available with different spatial resolutions from micrometer sizes to centimeters [68, 117, 118]. Even if one chooses tracers with the same size as the background material, because of different X-ray absorption, one usually has to deal with tracers of different densities and sedimentation may become an issue. A possible solution can be finding hollow particles as tracers with the same weight and outer diameter in a granular bed. An alternative method is Magnetic Resonance Imaging (MRI). MRI is a non-invasive tomographic imaging technique. It allows tracers for nuclear magnetization detection in a granular bed with the same physical properties. This can be achieved either by solid particles immersed in MRI-visible fluid or by doping an amount of MRI-visible tracers as in the following experiments of this chapter. Since soft grains in our study are moisture-containing liquids, we applied an MRI technique to detect the inner structure of a granular bed. To be mentioned, real-time imaging tomography is impossible because MRI takes time to receive signals during scanning and reconstructing the tomogram.

In this chapter, we start the rheology study of soft grains by analyzing displacements of grains in the shear cell and introduce an MRI technique [119–121] to detect the geometry of shear zones of soft granular materials. The time to record one tomogram is about one minute. During the data acquisition, the granular ensemble has to be at rest. Thus, the sample is sheared step by step, and MRI tomographs are recorded at each step in the static sample. The shear rate can be considered to be almost zero, based on the inertial number I introduced in Chapter 1. The flow regime can be thought of as quasi-static flow.

5.1 Introduction of MRI technology

In this section, we first introduce the principle of MRI technology. Protons and neutrons in atomic nuclei have their spins. The magnetization of nuclei is from the spin of nuclei and the spin of nuclei is from the superposition of angular momentum of protons and neutrons in the nuclei. The nucleus ^1H is studied in the greatest number of MRI papers because the nucleus ^1H has only one proton with high natural abundance and high resonance frequency. The tomography for ^1H is mostly done in the phase of liquid. However, the liquid material is magnetically neutral because of the random orientations of the protons in the material. When the liquid material is exposed to an external magnetic field B_0, the protons precess around the field. The precession

frequency f can be described by the Larmor equation,

$$f = \frac{\gamma B_0}{2\pi} \tag{5.1}$$

γ is the gyromagnetic ratio which is one of the properties of a specific nucleus or element. The frequency of spins depends on the strength of the external magnetic field. In a macroscopic body, consider a small enough volume element with volume V containing a large number of protons, magnetization M is introduced to describe the local magnetic moment per unit volume. For a clear description of macroscopic magnetization, if the liquid material is of two million spins, about 999999 with high energy precess opposite to the field direction, about 1000001 with low energy precess towards the field. So the macroscopic magnetization M is normally towards the direction of the external magnetic field and can be modeled by the Bloch equation,

$$M_x = |M| sin\alpha cos(2\pi ft) \tag{5.2}$$
$$M_y = |M| sin\alpha sin(2\pi ft) \tag{5.3}$$
$$M_z = |M| cos\alpha \tag{5.4}$$

α is the angle between the magnetization and the direction of the external magnetic field. The parallel or "longitudinal" component of the magnetization is $\vec{M}_{\parallel} = M_z\vec{z}$ and the transverse component $\vec{M}_{\perp} = M_x\vec{x} + M_y\vec{y}$.

The magnetization can be disrupted by using an external radio frequency(RF) pulse. Then the protons, which absorb the energy, are knocked down into an alternate plane and precess together in phase, which changes the longitudinal magnetization. The knocking-down angle depends on the strength and duration of the RF pulse. After the temporary excitation, the protons recover to their original state of orientation with the magnetic field.

Specifically, the spin echo sequence includes two RF pulses: a $\frac{\pi}{2}$-pulse followed by a π-pulse. First, the magnetization of a sample is flipped immediately by the first pulse and the longitudinal magnetization $M_{\parallel}$ is eliminated, and the transverse magnetization $M_{\perp}$ is generated with the protons' precession synchronizing. After the first pulse, the longitudinal magnetization increases, and the transverse magnetization decreases, the component magnetization vector would involve a spiral curve. During this recovery process, an electrical signal is induced which is called Free Induction Decay (FID). The time when the subsequent regrowth of $M_{\parallel}$ reaches 63% $(M_{\parallel})_0$, which is the longitudinal magnetization before the RF pulse or the initial magnetization, is T_1 and this process is called T_1 relaxation. At the same time, the transverse magnetization decays from maximum after the RF pulse because the spins become dephased given variable local fields, which are combined with the applied field and the fields of their neighbors. The time when the decreasing of $M_{\perp}$ approaches 37% $(M_{\perp})_{max}$, which is the maximum transverse magnetization after the RF pulse, is T_2 and this process is called T_2 relaxation. T_1 is longer than T_2 and T_1, T_2 depend upon material and environment.

So far, we only give a $\frac{\pi}{2}$-pulse once and receive the FID signal which decays rapidly. The external magnetic field can often be inhomogeneous. So the protons do not precess at the same frequency and after the RF pulse, they produce additional suppression of the FID signal, which is called T_2^* effect. The decay time T_2^* represents a combination of external field-induced and thermodynamic effects. To refocus the precessions, a second RF signal of a π- pulse is followed at time τ. The spins are flipped by angle π to the opposite way instantly. After another time τ, an echo signal would be received. The duration from the decayed signal till the consecutive echo signal received is called the echo time defined by $T_E = 2\tau$. Multiple π-pulse after a single $\frac{\pi}{2}$-pulse would be applied until the signal dies out. The spin-echo RF sequence is repeated after

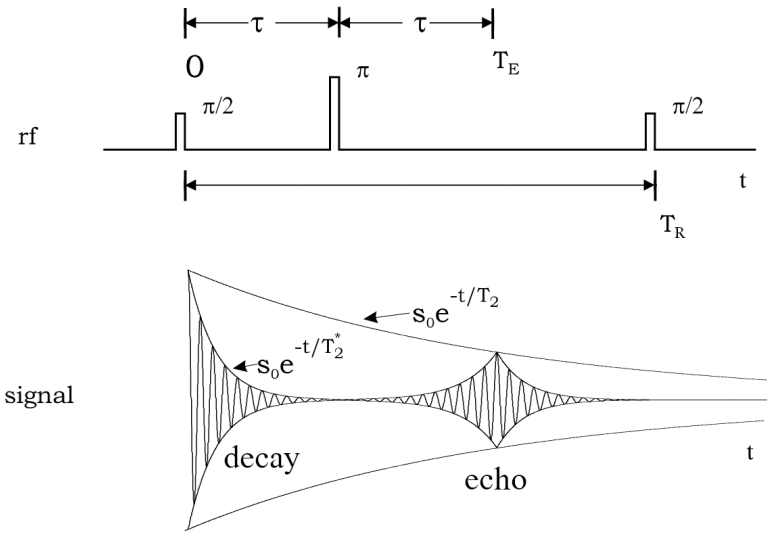

Figure 5.1: A sketch map of spin-echo RF. A $\frac{\pi}{2}$-pulse is applied at t=0 and a π-pulse at t=τ to invert the phase from the result of different spins. The spins rephase then, producing an echo. The signal strength is limited by the T_2 envelope at the echo time T_E=2τ. After multiple π-pulses until the signal dies out, another excitation from the second $\frac{\pi}{2}$-pulse is applied at repeated time T_R.

time T_R for another excitation from the $\frac{\pi}{2}$-pulse in the last spin-echo RF. The time T_R is called repetition time. However, this is a way to measure the T_2 relaxation time and T_2^* decay time. The progress is sketched in Fig 5.1.

Next, to obtain reconstructed tomography from the signals, the fundamentals are field gradients to locate spins at a certain position by their frequencies. A linear gradient in the magnetic field, denoted as $\vec{G}'$, modifies the local Larmor frequency f_L (see Eq. 5.1) to:

$$f_L = \frac{\gamma}{2\pi}(B_0 + \vec{G}' \cdot \vec{r}) \tag{5.5}$$

The frequencies along one coordinate can be used to infer the locations of spins. To obtain a 3D resolution of the tomography, the position information is encoded sequentially with three orthogonal gradients. In summary, magnetic field gradients can detect locations of spins and produce gradient echoes in the signal. References [121–127] contain more information on orthogonal field gradients for 3D imaging and reconstruction.

$CuSO_4$ solution has been achieved as MRI-visible fluid helping reduce the longitudinal relaxation time T_1 substantially [128], which can produce a strong MRI signal further because the FID signal can be reproduced more times in the same time set. In our MRI scanning, the repetition time T_R is set to 7.5ms, and the echo time T_E is set to 3.2ms. The recording of a single tomography lasts around 1$\sim$2min.

5.2 Experiments

In this section, we calibrate the shear zone in the bulk of soft particles. As we discussed in the Introduction chapter about different geometries for shear of granular materials, two basic geometries are generally studied: linear shear cells and rotating shear cells. The linear shear shear limits the displacement of granular materials and is applicable for oscillatory shear [129]. In continuous shear experiments, plate-plate or cone-plate geometries in closed rotating plates

are suitable for the shear rate dependence of the material [130, 131]. To investigate shear zones in transient and asymptotic states, a split-bottom cylinder shear cell, which has been proved reasonable [29, 30, 132], is used in the scanning. The dimension of this shear cell should be fitted to be placed in the MRI scanner. Fig 5.2 is a sketch of the shear cell in our experiments. The diameter of the outer plate (as a fixed bottom plate in Fig 5.2) is 150mm and the cell can be filled up to 80mm. It is manufactured from acrylic glass which is invisible for MRI. The inner disk can be rotated by hand from the top through the rod that connects to the bottom disk. The rotation speed can not be specifically controlled. It is of the order of $\approx 30^\circ/s$ and not faster than it. The shear rate is considered almost zero to be in the regime of quasi-static flow which is justified by the inertia number I (see Equation 1.2).

The rotation angle is measured by a goniometer fixed on the top sealed cover of the shear cell. In addition, two holes are drilled at the edge of the inner disk and filled with marker liquid to serve as MRI-visible tracers to retrieve the position and rotation state of the container from the MRI tomograms. The inner diameter of the container is $D_0 = 2R_0 = 150$mm and the diameter of the rotating plate is $D_s = 2R_s = 95$mm.

The MRI scanner used is a 3 Tesla Siemens MAGNETOM Skyra in the STIMULATE Forschungscampus Magdeburg with a 70cm bore inside and a short magnet. The tomograms have a voxel resolution of $0.75 \times 0.75 \times 0.7\text{mm}^3$. Recording a single tomogram takes about 1 minute since the setup is static during the recording. The acquisition time τ is in the range of a few milliseconds(ms), which is very short compared to the transversal relaxation time $T_2 > 1$s of pure water. T_1 of water is about 3s.

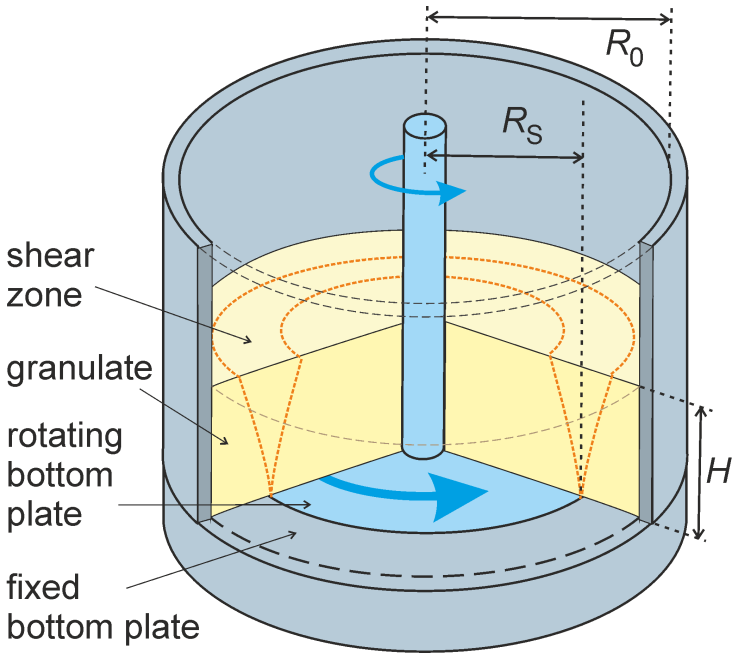

Figure 5.2: Sketch of the experimental setup: Grey parts are fixed in the MRI scanner, while the bottom disk and central rod sketched in light blue can be rotated about a vertical axis by well-defined steps. The granular material in the outer parts remains static and fixed to the outer container, while in the axial part, it rotates with the bottom disk. The bottom surface was roughened to prevent the first layer from sliding relative to the borders. The dashed lines sketch the boundaries of the shear zone. The image is reproduced from [133].

The soft, low-frictional material used in this chapter is hydrogel spheres. Two sizes of hydrogel spheres are used, small ones (mean diameter 2.5mm, mean weight 8mg) and large ones (mean

diameter 6.5mm, mean weight 180mg). The dry powder of the small HGS was received from *JRM Chemical, Cleveland, USA* in a polydisperse mixture with diameters from a few micrometers to about 0.5mm. The dry grains were sieved to obtain a narrow size distribution between 0.3mm and 0.355mm. After swelling in distilled water, the grains reached diameters between 2mm and 3mm. In the case of large ones, the dry particles were obtained from *Happy Store, Nanjing, China*, which is the same material as that used in Chapter 2. They were swollen in NaCl solution. The final diameter of hydrogel is around 6.5mm under a 3.8g/L salt concentration. The diameter of particles after swelling is with a variance of about 5%.

The swollen hydrogel spheres contain water and can emit a ^{1}H MR signal during MRI scanning. However, because of the fast repeating rate of scans, the recovery of the nuclear magnetization between subsequent scans is small and the signal is weak due to long T_1. Since we want to keep the experiment time short and strengthen the signals and brightness of tomograms, we use specially prepared tracers. The tracers are hydrogel articles that are swollen with an 8mMol aqueous solution $CuSO_4$ and the same NaCl concentration to control the same swollen size. The copper sulfate reduces the longitudinal relaxation time T_1 of nuclear magnetization by a value of 10% [128]. On average, our ensembles consist of approximately 30% doped hydrogel spheres (mean diameter 6.5mm), and 50% doped hydrogel spheres (mean diameter 2.5mm), each used individually. After particles were put into the shear cell, the samples were stirred to some extent to achieve a good distribution.

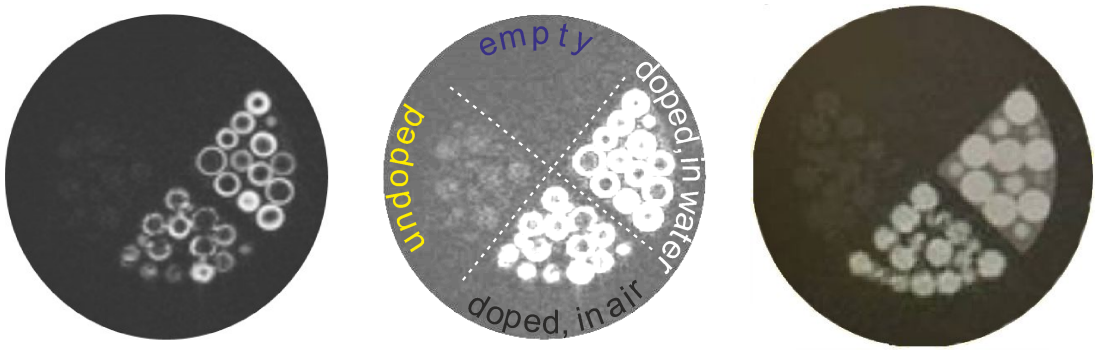

Figure 5.3: Left: Horizontal slice of the tomogram of a four-compartment cylindrical plastic container (50 mm inner diameter) with large (6.5 mm) hydrogel spheres. The top sector is empty. The left sector contains non-doped spheres, swollen in NaCl solution. The bottom sector contains spheres doped with copper sulfate, and the right sector is filled with the same spheres submerged in distilled water. Middle: strongly contrast-enhanced image of the same slice, which also shows the signal from non-doped HGS (in the left sector). Right: Same sample but doped in $CuSO_4$ for 5 months. The $CuSO_4$ doped spheres are now completely visible, they appear as solid spheres in the tomograms, not as shells. The image is reproduced from [133].

Fig 5.3 shows a slice of a test tomogram recorded with large hydrogel grains. The view is a horizontal cross-section of a cylindrical container with 4 compartments. The sector on the left is filled with 6.5mm HGS swollen in NaCl solution. The NMR signal is very weak because T_1 is much larger than the repeating rate of the scans (7.5ms per scan) so the nuclear magnetization does not recover between the scans. After the image gets contrast-enhanced, its weak signal is seen. In the bottom sector of the figure, 6.5mm HGS swollen in copper sulfate can be captured by the NMR receiver. The outer shells(about 1-2mm) of spheres in the bottom sector are visible while the inside of spheres remain invisible in the tomograms. The selected slice cuts the hydrogel spheres at different cross sections, therefore the rings seen in the slice have different diameters.

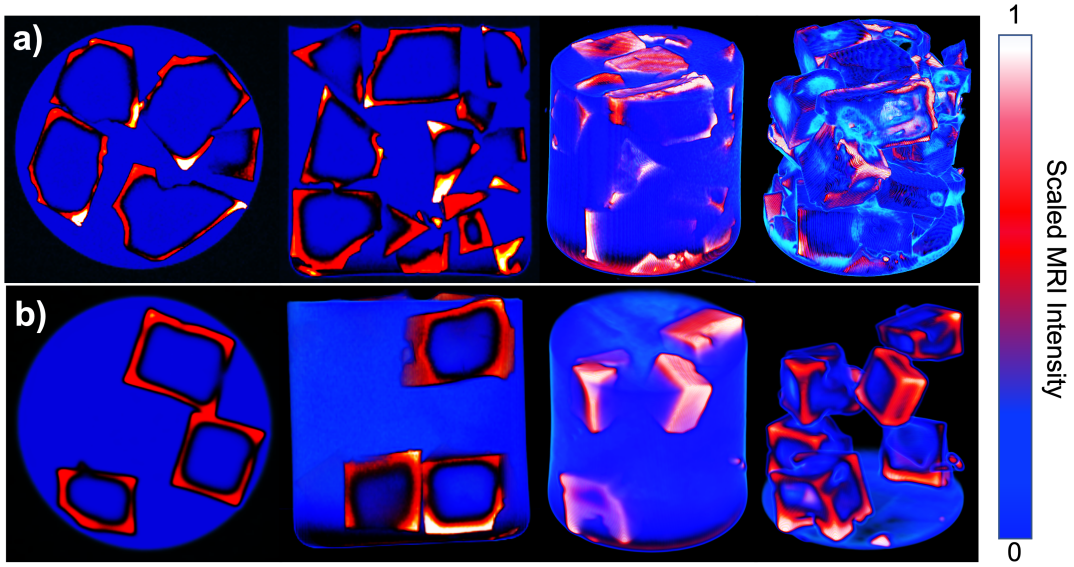

Figure 5.4: Nearly cube-shaped hydrogel blocks freshly swelled in 8 mM copper sulfate solution. (a) all hydrogel blocks labeled with $CuSO_4$, (b) only 30% of the blocks labeled. From left to right we show a central 2D horizontal slice, a 2D central vertical slice, a 3D rendering, and a 3D rendering with water outside the cubes removed. Red to white regions label thin surface regions of the particles. Blue regions (low NMR signal) are further inside the blocks or non-doped liquid around them. The container is a cylinder of 100 mm diameter, filled to a height of ≈ 95 mm. MRI intensities are scaled by the maximum value. The image is reproduced from [133].

This shell-type pattern of single spheres remained even after one week. Note that, since HGS in the bottom compartment were surrounded by air, the spheres appear to have broken, rocky, and uneven surfaces that are artifacts because the air has a different magnetic susceptibility from the water, resulting in the inhomogeneous magnetic field at the surfaces of the spheres. In the right sector, the same doped spheres were submersed in distilled water without the kind of artifacts shown in the bottom sector because the magnetic susceptibility of the spheres is nearly identical to that of the surrounding water resulting in a homogeneous field. Each grain can be identified in the tomography. The copper sulfate diffuses inside after several weeks. As seen in the right image in Fig 5.3, the same sample is doped in copper sulfate for several months, the signals reflected in MRI show the spheres that are now fully marked with copper sulfate.

Before we describe our shear experiments with hydrogel spheres, we want to demonstrate this detection method which $CuSO_4$ slowly diffuses into hydrogel particle cores during the swelling process. We scanned centimeter-sized irregular but nearly cube-shaped hydrogel blocks (*GB-740, Educational Innovation, Bethel CT, USA*). The swelling process took 24 hours and the MRI scans were performed after swelling for 5 days. The 2D cross sections of tomograms in Fig 5.4 confirm that $CuSO_4$ decorates the zones only at the surface of blocks, in a similar way as the spherical hydrogel in Fig 5.3. This makes the individual blocks visible in the tomograms. If the complete hydrogel material would be NMR visible, blocks lying side by side would hardly be distinguished. When we decreased the share of doped particles in the packing, from 100% (Fig 5.3(a)) to 30% (Fig 5.3(b)), we could track the doped blocks by segmenting the doped cubes which are visible through edges. So this detection method can be extended to any shape of hydrogel particles.

5.3 Results

5.3.1 PTV and PIV analysis

Particle tracking velocimetry(PTV) and particle image velocimetry(PIV) are methods for volumetric velocity measurements by imaging the motion of particles. PTV tracks the motion of individual particles, while PIV measures the mean displacement of clusters of particles in the interrogation window. PIV is a well-established technique and has well-developed software for solutions. It invokes statistical methods to track the displacements of particles. The basic approach is to divide the entire field-to-view into smaller regions which are called interrogation areas. Fourier Transform would help to find the most correlated parts by cross-correlating the interrogation areas at two consecutive time steps, the displacement information between two subsequent images. The accuracy of PIV is impacted by the size of the interrogation region. PTV is the alternative method beginning with the recognition of particles and the estimation of their centroids. The simplest method for the detection of individual particles from the image intensity distribution is to set a threshold for binarization in a binarized image. This is very suitable for low-density flows where the edge of each particle can be identified. However, in dense granular flows, particles tend to overlap resulting in no sharp edges and particles move randomly creating a non-homogeneous distribution of the intensity matrix of brightness in particle images. Of course, there are also many other methods for particle detection, such as Hough Circle Transform, particle-mask correlation, watershed segmentation, etc. However, for the PTV method, no matter what way to detect the individual particles, the disadvantages always arise from the particle centroid uncertainties and the linear approximation of particle trajectories, though it can extract velocity information and trajectories of each particle and more information, such as deformation, contacting points and so on, of each particle from images with desirable resolution.

We have applied both methods in processing MR images from the experiments. The method of PTV was applied for large grains of 6.5mm diameter. Fig 5.5 was constructed from horizontal slices of tomograms at a 20mm height layer of the shear cell. After filling the container with HGS, the first tomogram was taken and then the inner rotating disk was rotated roughly by 30°, and another tomogram was recorded. We assumed that the ratio of the angular displacement of a tracer (prepared by doping in $CuSO_4$) $\frac{r\theta\pi/180^\circ}{r\theta_0\pi/180^\circ} = \frac{\theta}{\theta_0}$ ($\theta_0 \approx 30^\circ$ where 30° is the angle for each rotation) at a given radius r and height h is equal to the ratio of angular velocities $\frac{\omega}{\omega_0}$ (ω_0 is the angular velocity of the rotating axis) because of quasi-static shear flow.

Fig 5.5(a) and (b) show the overlay of two different slices in pseudocolor: the green color plane of one slice is replaced by the green color plane of the same slice in the second tomogram, while red and blue color planes remain unchanged. White spots in Fig 5.5 are for tracers that have not changed their positions, dark grey spots represent the background of non-doped spheres and green or magenta spots are particles that have been displaced. The tracers in the 0° appear in the color of magenta and those in the 27° appear in green. In Fig 5.5(a), the outer grains stay at their original positions while the grains in the center have rotated with the bottom disk. The arrows in Fig 5.5 represent the displacement. The slices shown are located at $h = 10$mm above the bottom which is in the middle of the granular bed. Fig 5.5(b) is the result of digitally rotating the second tomogram backward, so the tracers in white stand for particles rotating with the bottom inner plate. The tracers in green and magenta color moved as the bottom disk moved. Fig 5.5(c) and (d) are the overlays with tomograms recorded at 210° and 240° rotation angles. Fig 5.5 confirms that all tracers located at similar heights and radii are displaced by approximately the same angle.

The PIV method is used for small grains of 2-3mm diameter. For small grains, the PTV

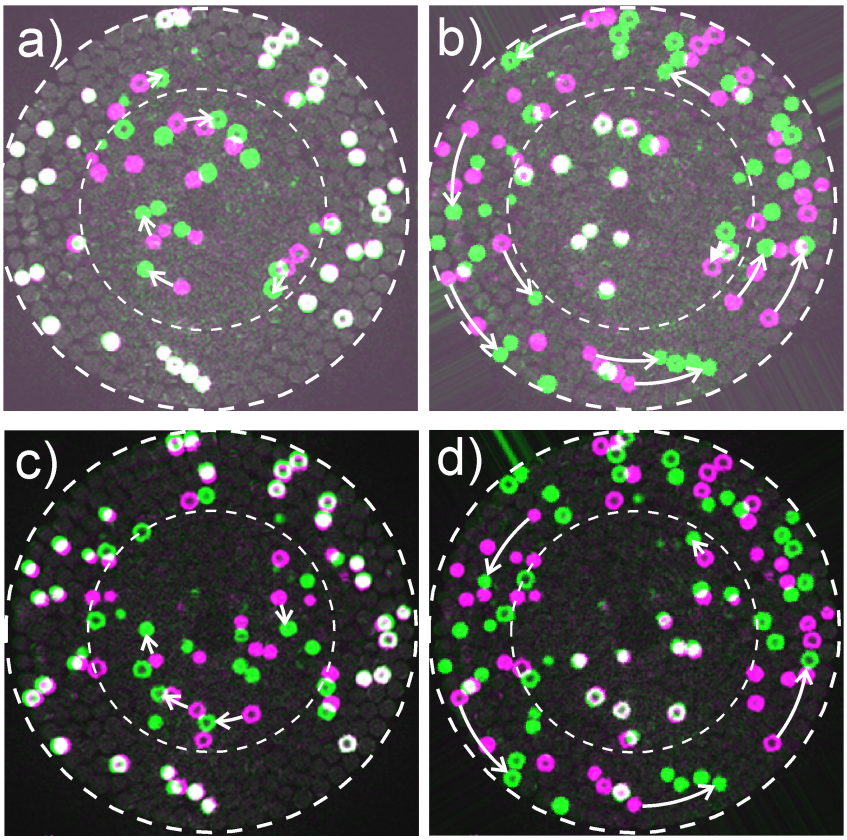

Figure 5.5: Displacement of large HGS during $\approx 30^\circ$ rotations of the bottom plate. A horizontal slice at 10 mm height within a 20 mm high granular layer was selected. The dashed lines mark the inner of the container wall and the border of the rotating bottom disk. (a) shows in white the immobile tracers, in magenta the tracer positions after filling in the shear cell, and in green the displaced positions after rotation of the plate. Arrows indicate examples of selected displacements of individual tracers. (b) shows the differences in the frame of the rotating disk (disk rotation compensated by appropriate digital rotation of the slice), white tracers moved with the disk, magenta and green are tracers in the 0° and 27° tomograms. (c),(d) respectively present the same operations with the same slice between the 210° and 240° rotations of the bottom plate.

method in principle can also be used but much smaller shear steps (of the order of 5°) are needed for a correct mapping of such small individual grains. Even though PIV can be less accurate compared with the PTV method, PIV can be still useful for small grains in one small moving step of 10° rotations. The mean displacements of the ring zones (h,r) (and $h = 2\pi r$) can be calculated by cross-correlation of voxels and averaging over the whole ring zone.

5.3.2 Flow profiles

As the PTV and PIV methods in the last section, stationary shear zones have been determined. The angles corresponding to displacements at a specific height and radius are scaled by the rotation angle of the bottom disk. It can be extrapolated to the effect of a continuous rotation. So it can be assumed that the ratio of rotation angles to the rotation angle of markers fixed at the rotating bottom disk is equal to the ratio of rotation speeds in a given (h,r) zone to the rotation frequency ω_0 of the bottom disk. In Fig 5.6(a), the top figure is for a bed height $H \approx 20\text{mm}(\frac{H}{R_s} = 0.42)$, the middle figure for $H \approx 40\text{mm}(\frac{H}{R_s} = 0.84)$ and the bottom figure for $H \approx 50\text{mm}(\frac{H}{R_s} = 1.05)$. The first layer of grains above the bottom disk rotates with the disk

in all cases. In the shallow granular bed ($H \approx 20$mm), the shear gradient is almost horizontal everywhere, with a slight widening of the shear zone towards the top. With increasing bed height, the shear zone bends inwards. For the largest bed height studied in our MRI experiments, the shear gradient is nearly vertical everywhere but is confined to the first layer of HGS at the bottom.

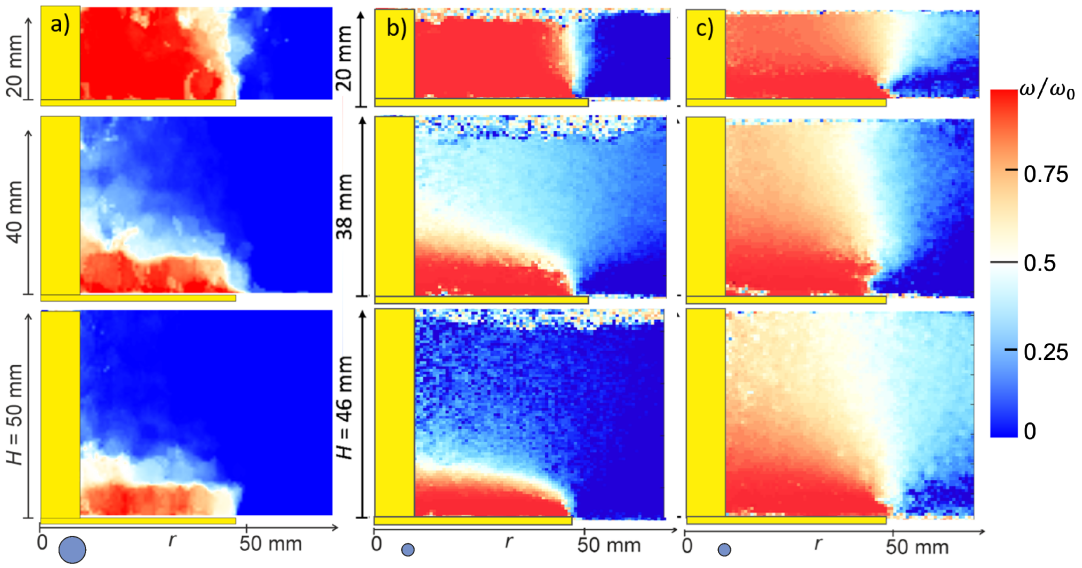

Figure 5.6: Flow profiles, a) for large HGS (without immersion fluid), b) for small HGS (without immersion fluid), and c) for small HGS (grains immersed in water) in beds of different heights. Grey circles sketch the typical bead sizes. The angular velocity $\omega(r,h)$ was normalized by the bottom disk angular velocity ω_0. The shear zone where the angular velocity ranges between 0 and ω_0 is visible as a bright band separating the grains at rest (outside) and co-rotating with the disk (center). The yellow bars in each figure show the positions of the central rod and the rotating inner plate. The image is reproduced from [133].

For small grains, we set two situations: One is called a drained environment in which the voids between spheres are surrounded almost completely by air. Some excess water attached to spheres is still there but in small quantities. The shear zones constructed in this situation are shown in Fig 5.6(b); the other one is called the submersed environment in which the voids between HGS are filled with water, the shear zones in this situation are shown in Fig 5.6(c). As shown in Fig 5.6(b), at low filling height, the shear zone reaches the top surface and is almost vertical. Above a certain filling height e. g. 46mm or 50mm, the shear zone closes. These results are qualitatively similar to the results with rigid, frictional grains in earlier studies. In Fig 5.6(c), the shear zone is much broader for all filling heights. With increasing bed height, the shear zone does not close like the dome above the disk. Even when the bed height H is comparable to the disk radius, the top layers react to the bottom rotation. This is somehow counter-intuitive since a reduced effective weight leads to lower vertical contact forces so that the transmission of shear forces in the vertical direction is reduced.

5.4 discussion

In this chapter of the thesis, we characterized the shear profiles for soft particle ensembles and introduced the method of Magnetic Resonance Imaging for detecting the shear profiles. The

displacement of particles is determined from differences in tomograms after stepwise rotation of the bottom disk in a split-bottom container. The tracers for MRI detection can be separated in the constructed tomograms and the tracers are also HGS with the same physical properties as the other non-marked part of particles in the ensembles. In addition, $CuSO_4$ solution as a tracer substantially reduces the recording time of the spectra.

Since there is little difference in the shear profiles of different particle sizes, shown in Fig 5.6(a) and (b), liquid capillary bridges, forming at the contact between HGS, do not influence the shear behavior. In drained and submerged environments, the shear profiles for HGS exhibit considerable differences. Since the effect of capillary forces has been excluded, the differences can be attributed to the shear of water between the particle voids. The system of low-frictional HGS immersed within water behaves more liquid-like, i. e. the shear zone tends to spread across the cell. Shear forces on a macroscopic scale can be used to calibrate particle-particle contacts. Moreover, for low-frictional HGS, the internal friction with liquid may have a comparable influence as the particle-particle contact. The internal friction between different phases can result in the distinct shear profile of HGS immersed in water. It is suggested to measure the dependence of this frictional force on shear rates in the following work.

6 Summary

In conclusion, this thesis has investigated the statistical dynamics of soft grains in different flow types, especially in silo discharge. The behavior of soft grains has been observed, which is not the same as the behavior of widely studied hard grains. The main results of the thesis are:

- The intermittent flow of pure soft hydrogel spheres passing through a narrow orifice of quasi-2D silo is pressure-dependent and when hydrogel spheres stop flowing out, the particles in the silo still rearrange their positions. This demonstrates that the systems, where the orifice size was very small around 2 particle diameters, do not reach the equilibrium even the particles stop flowing out of the silo.

- The mixtures of soft hydrogel and hard frictional spheres discharging from the quasi-2D silo recover to be pressure-independent. The statistics of the concentration of hard spheres in clogging structures and the results of the simulations, both support that the particle friction properties of the ensemble for discharge influence the discharging characteristics.

- The effect of an obstacle near the orifice on discharging soft grains from a quasi-2D silo doesn't show the phenomenon of 'slower is faster'. On the contrary, the obstacle makes the outflow rate of particles slow down the outflow rate of particles passing through the orifices. It can be explained by this: the obstacle alleviates the pressure in front of the orifice, and the discharge of the soft sphere depends on the pressure, which aligns with the earlier conclusion.

- An MRI method is introduced to detect the shear band of soft grains in a cyclic shear cell. $CuSO_4$ added by a very small amount of the NaCl solution for swelling the hydrogel spheres reduces the longitudinal relaxation time T_1 of the nuclear magnetization compared with that of pure water. This allows us to create reconstructed images with labeled particles in a short time.

- We investigated the shear zone geometry of soft grains submersed in water and drained ensembles. In the drained case, the shear zone reaches the top and is almost vertical at a low filling height. However, the shear zone closes when the shear cell is filled above a certain height. But in the immersed case, the shear zone is much broader for all cases of filling heights.

These systematic studies explore the dynamic characteristics of soft spherical particles. These soft particles are elastic and smooth. They reveal that friction is one of the essential properties to differentiate the dynamics of our soft particles from hard frictional particles. During the PhD study, the results were published in several international physical journals. The following papers were published about the topics treated in this thesis:

(1) K. Harth, J. Wang, T. Börzsönyi, et al. Intermittent flow and transient congestions of soft spheres passing narrow orifices. Soft Matter, 2020, 16(34): 8013-8023. [71]

(2) J. Wang, B. Fan, T. Pongó, et al. Silo discharge of mixtures of soft and rigid grains[J]. Soft Matter, 2021, 17(16): 4282-4295. [82]

(3) J. Wang, K. Harth, R. Stannarius, B. Fan, T. Börzsönyi. Discharge of soft and hard grains and their mixtures from 2D silos. EPJ Web Conf. Powders & Grains, 2021, 249. [134]

(4) Wang J, Harth K, Puzyrev D, et al. The effect of obstacles near a silo outlet on the discharge of soft spheres[J]. New Journal of Physics, 2022, 24(9): 093010. [104]

(5) J. Wang, Z. Farmani, J. A. Dijksman, et al. Characterization of shear zones in soft granular beds employing a novel magnetic resonance imaging technique. Granular Matter 24, 103 (2022). [133]

In the following work, it would be interesting to measure the drag force during discharge from a silo when there is an intruder inside, in order to check the interaction between soft particles because the frictional force becomes an important factor during discharge based on Chapter 3. In shear cells, it would also be significant to study the characteristics of shear bands when the ensembles suffer some different compressing force on the surface. It is thought-provoking to check the effect of particle contact force measured by the shear-rate-dependent torque in rheology experiments.

References

[1] B. S. Kerner. Experimental features of self-organization in traffic flow. *Physical Review Letters*, 81(17):3797–3800, 1998.

[2] S. Dorbolo, L. Maquet, M. Brandenbourger, F. Ludewig, G. Lumay, H. Caps, N. Vandewalle, S. Rondia, M. Mélard, et al. Influence of the gravity on the discharge of a silo. *Granular Matter*, 15(3):263–273, 2013.

[3] A. Guariguata, M. A. Pascall, M. W. Gilmer, A. K. Sum, E. D. Sloan, C. A. Koh, and D.T. Wu. Jamming of particles in a two-dimensional fluid-driven flow. *Physical Review E*, 86(6):061311, 2012.

[4] C. Conesa, K. Saleh, A. Thomas, P. Guigon, and N. Guillot. Characterization of flow properties of powder coatings used in the automotive industry. *KONA Powder and Particle Journal*, 22:94–106, 2004.

[5] A. E. Lobkovsky, A. V. Orpe, R. Molloy, A. Kudrolli, and D. H. Rothman. Erosion of a granular bed driven by laminar fluid flow. *Journal of Fluid Mechanics*, 605:47–58, 2008.

[6] A. B. Metzner, W. T. Houghton, R. A. Sailor, and J. L. White. A method for the measurement of normal stresses in simple shearing flow. *Transactions of the Society of Rheology*, 5(1):133–147, 1961.

[7] J. J. Bluemink, D. Lohse, A. Prosperetti, and L. van Wijngaarden. A sphere in a uniformly rotating or shearing flow. *Journal of Fluid Mechanics*, 600:201–233, 2008.

[8] H. M. Jaeger, S. R Nagel, and R. P. Behringer. Granular solids, liquids, and gases. *Reviews of Modern Physics*, 68(4):1259–1273, 1996.

[9] JN. Roux and G. Combe. Quasistatic rheology and the origins of strain. *Comptes Rendus Physique*, 3(2):131–140, 2002.

[10] I. Goldhirsch. Rapid granular flows. *Annual Review of Fluid Mechanics*, 35(1):267–293, 2003.

[11] O. Pouliquen and F. Chevoir. Dense flows of dry granular material. *Comptes Rendus Physique*, 3(2):163–175, 2002.

[12] M. Y. Hou, W. Chen, T. Zhang, K. Lu, and C. K. Chan. Global nature of dilute-to-dense transition of granular flows in a 2d channel. *Physical Review Letters*, 91(20):204–301, 2003.

[13] D. C. Huang, G. Sun, and K. G. Lu. Relationship between the flow rate and the packing fraction in the choke area of the two-dimensional granular flow. *Physical Review E*, 74(6):061306, 2006.

[14] A. Garcimartín, C. Mankoc, A. Janda, R. Arévalo, J. M. Pastor, I. Zuriguel, and D. Maza. Flow and jamming of granular matter through an orifice. In *Traffic and Granular Flow'07*, pages 471–486. Springer, 2009.

[15] H. A. Janssen. Versuche uber getreidedruck in silozellen. *Z. Ver. Deut. Ing.*, 39:1045–1049, 1895.

[16] M. Sperl. Experiments on corn pressure in silo cells–translation and comment of janssen's paper from 1895. *Granular Matter*, 8(2):59–65, 2006.

[17] B. Q. Kou, Y. X. Cao, J. D. Li, C. J. Xia, Z. F. Li, H. P. Dong, A. Zhang, J. Zhang, W. Kob, and Y. J. Wang. Granular materials flow like complex fluids. *Nature*, 551(7680):360–363, 2017.

[18] Y. X. Cao, J. D. Li, B. Q. Kou, C. J. Xia, Z. F. Li, R. C. Chen, H. L. Xie, T. Q. Xiao, W. Kob, L. Hong, et al. Structural and topological nature of plasticity in sheared granular materials. *Nature Communications*, 9(1):1–7, 2018.

[19] I. S. Aranson and L. S. Tsimring. Patterns and collective behavior in granular media: Theoretical concepts. *Reviews of Modern Physics*, 78(2):641–692, 2006.

[20] H. W. Zhu, Q. F. Shi, N. Zheng, and D. C. Huang. The effects of physical factors on the granular hopper flow. *SCIENTIA SINICA Physica, Mechanica & Astronomica*, 50(9):090005, 2020.

[21] W. A. Beverloo, H. A. Leniger, and J. van de Velde. The flow of granular solids through orifices. *Chemical Engineering Science*, 15(3):260–269, 1961.

[22] R. L. Brown and J. C. Richards. *Principles of powder mechanics: essays on the packing and flow of powders and bulk solids*. Elsevier, 2016.

[23] Y. Forterre and O. Pouliquen. Flows of dense granular media. *Annual Review of Fluid Mechanics*, 40(1):1–24, 2008.

[24] GDR MiDi. On dense granular flows. *The European Physical Journal E*, 14(4):341–365, 2004.

[25] C. S. Campbell. Granular shear flows at the elastic limit. *Journal of Fluid Mechanics*, 465:261–291, 2002.

[26] H. H. Shen and B. Sankaran. Internal length and time scales in a simple shear granular flow. *Physical Review E*, 70(5):051308, 2004.

[27] T. Unger, J. Török, J. Kertész, and D. E. Wolf. Shear band formation in granular media as a variational problem. *Physical Review Letters*, 92(21):214–301, 2004.

[28] J. A. Dijksman and M. van Hecke. Granular flows in split-bottom geometries. *Soft Matter*, 6(13):2901–2907, 2010.

[29] D. Fenistein and M. van Hecke. Wide shear zones in granular bulk flow. *Nature*, 425(6955):256–256, 2003.

[30] D. Fenistein, J. W. van de Meent, and M. van Hecke. Universal and wide shear zones in granular bulk flow. *Physical Review Letters*, 92(9):094301, 2004.

[31] X. Cheng, J. B. Lechman, A.o Fernandez-Barbero, G. S. Grest, H. M. Jaeger, G. S. Karczmar, M. E. Möbius, and S. R. Nagel. Three-dimensional shear in granular flow. *Physical Review Letters*, 96(3):038001, 2006.

[32] H. Ahn, Z. Başaranoğlu, M. Yılmaz, A. Buğutekin, and M. Z. Gül. Experimental investigation of granular flow through an orifice. *Powder Technology*, 186(1):65–71, 2008.

[33] S. M. Rubio-Largo, A. Janda, D. Maza, I. Zuriguel, and R. C. Hidalgo. Disentangling the free-fall arch paradox in silo discharge. *Physical Review Letters*, 114(23):238002, 2015.

[34] A. Janda, I. Zuriguel, and D. Maza. Flow rate of particles through apertures obtained from self-similar density and velocity profiles. *Physical Review Letters*, 108(24):248001, 2012.

[35] A. Janda, R. Harich, I. Zuriguel, D. Maza, P. Cixous, and A. Garcimartín. Flow-rate fluctuations in the outpouring of grains from a two-dimensional silo. *Physical Review E*, 79(3):031302, 2009.

[36] G. H. Ristow. Outflow rate and wall stress for two-dimensional hoppers. *Physica A: Statistical Mechanics and its Applications*, 235(3-4):319–326, 1997.

[37] J. Koivisto, M. Korhonen, M. Alava, C. P. Ortiz, D. J. Durian, and A. Puisto. Friction controls even submerged granular flows. *Soft Matter*, 13(41):7657–7664, 2017.

[38] Y. W. Yu and H. Saxén. Discrete element method simulation of properties of a 3d conical hopper with mono-sized spheres. *Advanced Powder Technology*, 22(3):324–331, 2011.

[39] S. Zhang, P. Lin, C. L. Wang, Y. Tian, J. F. Wan, and L. Yang. Investigating the influence of wall frictions on hopper flows. *Granular Matter*, 16(6):857–866, 2014.

[40] J. C. Tsai, W. Losert, G. A. Voth, and J. P. Gollub. Two-dimensional granular poiseuille flow on an incline: Multiple dynamical regimes. *Physical Review E*, 65(1):011306, 2001.

[41] M. Madrid, K. Asencio, and D. Maza. Silo discharge of binary granular mixtures. *Physical Review E*, 96(2):022904, 2017.

[42] P. Artega and U. Tüzün. Flow of binary mixtures of equal-density granules in hoppers—size segregation, flowing density and discharge rates. *Chemical Engineering Science*, 45(1):205–223, 1990.

[43] S. Humby, U. Tüzün, and A. B. Yu. Prediction of hopper discharge rates of binary granular mixtures. *Chemical Engineering Science*, 53(3):483–494, 1998.

[44] J. Y. Tang and R. P. Behringer. Orientation, flow, and clogging in a two-dimensional hopper: Ellipses vs. disks. *Europhysics Letters*, 114(3):34002, 2016.

[45] T. Börzsönyi, E. Somfai, B. Szabó, S. Wegner, P. Mier, G. Rose, and R. Stannarius. Packing, alignment and flow of shape-anisotropic grains in a 3d silo experiment. *New Journal of Physics*, 18(9):093017, 2016.

[46] T. Kanzaki, M. Acevedo, I. Zuriguel, I. Pagonabarraga, D. Maza, and R. C. Hidalgo. Stress distribution of faceted particles in a silo after its partial discharge. *The European Physical Journal E*, 34(12):1–8, 2011.

[47] S. D. Liu, Z. Y. Zhou, R. P. Zou, D. Pinson, and A. B. Yu. Flow characteristics and discharge rate of ellipsoidal particles in a flat bottom hopper. *Powder Technology*, 253:70–79, 2014.

[48] S. Q. Wang, Y. N. Fan, and S. Y. Ji. Interaction between super-quadric particles and triangular elements andits application to hopper discharge. *Powder Technology*, 339:534–549, 2018.

[49] Y. Xu, K. D. Kaful, C. Thornton, and G. P. Lian. Effects of material properties on granular flow in a silo using dem simulation. *Particulate Science and Technology*, 20(2):109–124, 2002.

[50] R. S. Rivlin. Large elastic deformations of isotropic materials. i. fundamental concepts. In *Collected Papers of R. S. Rivlin: Volume I and II*, pages 23–54. Springer, 1997.

[51] T. Murata. Deformation of an elastic particle suspended in an arbitrary flow field. *Journal of the Physical Society of Japan*, 50(3):1009–1016, 1981.

[52] T. Gao, H. H. Hu, and P. P. Castañeda. Dynamics and rheology of elastic particles in an extensional flow. *Journal of Fluid Mechanics*, 715:573–596, 2013.

[53] M. M. Villone, F. Greco, M. A. Hulsen, and P. L. Maffettone. Simulations of an elastic particle in newtonian and viscoelastic fluids subjected to confined shear flow. *Journal of Non-Newtonian Fluid Mechanics*, 210:47–55, 2014.

[54] C. R. Wassgren, M. L. Hunt, P. J. Freese, J. Palamara, and C. E. Brennen. Effects of vertical vibration on hopper flows of granular material. *Physics of Fluids*, 14(10):3439–3448, 2002.

[55] J. E. Hilton and P. W. Cleary. The effect of rotational shear on granular discharge rates. *Physics of Fluids*, 22(7):071701, 2010.

[56] P. A. Gago, D. R. Parisi, and L. A. Pugnaloni. "faster is slower" effect in granular flows. In *Traffic and Granular Flow'11*, pages 317–324. Springer, 2013.

[57] I. Zuriguel, A. Janda, A. Garcimartín, C. Lozano, R. Arévalo, and D. Maza. Silo clogging reduction by the presence of an obstacle. *Physical Review Letters*, 107(27):278001, 2011.

[58] C. Lozano, A. Janda, A. Garcimartin, D. Maza, and I. Zuriguel. Flow and clogging in a silo with an obstacle above the orifice. *Physical Review E*, 86(3):031306, 2012.

[59] S. I. Alonso-Marroquin, F .and Azeezullah, S. A. Galindo-Torres, and L. M. Olsen-Kettle. Bottlenecks in granular flow: when does an obstacle increase the flow rate in an hourglass? *Physical Review E*, 85(2):020301, 2012.

[60] P. Huber-Burnand. Über den ausfluß und den druck des sandes. schreiben des hrn. huber-burnand an hrn. prof. prevost. *Polytech. J.*, 34(4):270–280, 1829.

[61] F. C. Franklin and L. N. Johanson. Flow of granular material through a circular orifice. *Chemical Engineering Science*, 4(3):119–129, 1955.

[62] R. M. Nedderman, U. Tüzün, S. B. Savage, and G. T. Houlsby. Flow of granular materials-i. discharge rates from hoppers. *Chemical Engineering Science*, 37(11):1597–1609, 1982.

[63] C. Mankoc, A. Janda, R. Arevalo, J. M. Pastor, I. Zuriguel, A. Garcimartín, and D. Maza. The flow rate of granular materials through an orifice. *Granular Matter*, 9(6):407–414, 2007.

[64] A. Anand, J. S. Curtis, C. R. Wassgren, B. C. Hancock, and W. R. Ketterhagen. Predicting discharge dynamics from a rectangular hopper using the discrete element method (dem). *Chemical Engineering Science*, 63(24):5821–5830, 2008.

[65] A. Marin, H. Lhuissier, M. Rossi, and C. J. Kähler. Clogging in constricted suspension flows. *Physical Review E*, 97(2):021102, 2018.

[66] M. Souzy, I. Zuriguel, and A. Marin. Transition from clogging to continuous flow in constricted particle suspensions. *Physical Review E*, 101(6):060901, 2020.

[67] X. Hong, M. Kohne, M. Morrell, H. R. Wang, and E. R. Weeks. Clogging of soft particles in two-dimensional hoppers. *Physical Review E*, 96(6):062605, 2017.

[68] R. Stannarius, D. Sancho Martinez, T. Finger, E. Somfai, and T. Börzsönyi. Packing and flow profiles of soft grains in 3d silos reconstructed with x-ray computed tomography. *Granular Matter*, 21(3):1–10, 2019.

[69] A. Ashour, T. Trittel, T. Börzsönyi, and R. Stannarius. Silo outflow of soft frictionless spheres. *Physical Review Fluids*, 2(12):123302, 2017.

[70] R. Stannarius, D. Sancho Martinez, T. Börzsönyi, M. Bieberle, F. Barthel, and U. Hampel. High-speed x-ray tomography of silo discharge. *New Journal of Physics*, 21(11):113054, 2019.

[71] K. Harth, J. Wang, T. Börzsönyi, and R. Stannarius. Intermittent flow and transient congestions of soft spheres passing narrow orifices. *Soft Matter*, 16(34):8013–8023, 2020.

[72] R. C. Hidalgo, A. Goñi-Arana, A. Hernández-Puerta, and I. Pagonabarraga. Flow of colloidal suspensions through small orifices. *Physical Review E*, 97(1):012611, 2018.

[73] C. Mankoc, A. Garcimartín, I. Zuriguel, D. Maza, and L. A. Pugnaloni. Role of vibrations in the jamming and unjamming of grains discharging from a silo. *Physical Review E*, 80(1):011309, 2009.

[74] B. V. Guerrero, L. A. Pugnaloni, C. Lozano, I. Zuriguel, and A. Garcimartín. Slow relaxation dynamics of clogs in a vibrated granular silo. *Physical Review E*, 97(4):042904, 2018.

[75] B. V. Guerrero, B. Chakraborty, I. Zuriguel, and A. Garcimartín. Nonergodicity in silo unclogging: Broken and unbroken arches. *Physical Review E*, 100(3):032901, 2019.

[76] K. To and H. T. Tai. Flow and clog in a silo with oscillating exit. *Physical Review E*, 96(3):032906, 2017.

[77] I. Zuriguel, D. R. Parisi, R. C. Hidalgo, C. Lozano, A. Janda, P. A. Gago, J. P. Peralta, L. M. Ferrer, L. A. Pugnaloni, E. Clément, et al. Clogging transition of many-particle systems flowing through bottlenecks. *Scientific Reports*, 4(1):1–8, 2014.

[78] S. S. Manna and H. J. Herrmann. Intermittent granular flow and clogging with internal avalanches. *The European Physical Journal E*, 1(4):341–344, 2000.

[79] I. Zuriguel, A. Garcimartín, D. Maza, L. A. Pugnaloni, and J. M. Pastor. Jamming during the discharge of granular matter from a silo. *Physical Review E*, 71(5):051303, 2005.

[80] C. C. Thomas and D. J. Durian. Fraction of clogging configurations sampled by granular hopper flow. *Physical Review Letters*, 114(17):178001, 2015.

[81] C. C. Thomas and D. J. Durian. Geometry dependence of the clogging transition in tilted hoppers. *Physical Review E*, 87(5):052201, 2013.

[82] J. Wang, B. Fan, T. Pongó, K. Harth, T. Trittel, R. Stannarius, M. Illig, T. Börzsönyi, and R. C. Hidalgo. Silo discharge of mixtures of soft and rigid grains. *Soft Matter*, 17(16):4282–4295, 2021.

[83] T. Pongó, V. Stiga, J. Török, S. Lévay, B. Szabó, R. Stannarius, R. C. Hidalgo, and T. Börzsönyi. Flow in an hourglass: particle friction and stiffness matter. *New Journal of Physics*, 23(2):023001, 2021.

[84] J. R. Darias, M. A. Madrid, and L. A. Pugnaloni. Differential equation for the flow rate of discharging silos based on energy balance. *Physical Review E*, 101(5):052905, 2020.

[85] C. Kloss, C. Goniva, A. Hager, S. Amberger, and S. Pirker. Models, algorithms and validation for opensource dem and cfd–dem. *Progress in Computational Fluid Dynamics, an International Journal*, 12(2-3):140–152, 2012.

[86] T. Pöschel and T. Schwager. *Computational granular dynamics: models and algorithms*. Springer Science & Business Media, 2005.

[87] N. Brodu, J. A. Dijksman, and R. P. Behringer. Multiple-contact discrete-element model for simulating dense granular media. *Physical Review E*, 91(3):032201, 2015.

[88] N. Brodu, J. A. Dijksman, and R. P. Behringer. Spanning the scales of granular materials through microscopic force imaging. *Nature Communications*, 6(1):1–6, 2015.

[89] C. C. Thomas and D. J. Durian. Intermittency and velocity fluctuations in hopper flows prone to clogging. *Physical Review E*, 94(2):022901, 2016.

[90] F. Alonso-Marroquin and P. Mora. Beverloo law for hopper flow derived from self-similar profiles. *Granular Matter*, 23(1):1–8, 2021.

[91] S. Mondal and M. M. Sharma. Role of flying buttresses in the jamming of granular matter through multiple rectangular outlets. *Granular Matter*, 16(1):125–132, 2014.

[92] A. Kunte, P. Doshi, and A. V. Orpe. Spontaneous jamming and unjamming in a hopper with multiple exit orifices. *Physical Review E*, 90(2):020201, 2014.

[93] K. Chen, M. B. Stone, R. Barry, M. Lohr, W. McConville, K. Klein, B. L. Sheu, A. J. Morss, T. Scheidemantel, and P. Schiffer. Flux through a hole from a shaken granular medium. *Physical Review E*, 74(1):011306, 2006.

[94] M. G. Areán, A. Boschan, M. A. Cachile, and M. A. Aguirre. Granular flow through an aperture: Influence of obstacles near the outlet. *Physical Review E*, 101(2):022901, 2020.

[95] D. Helbing, P. Molnár, and F. Schweitzer. Computer simulations of pedestrian dynamics and trail formation. *arXiv preprint cond-mat/9805074*, 1998.

[96] D. Helbing, P. Molnár, I. J. Farkas, and K. Bolay. Self-organizing pedestrian movement. *Environment and Planning B: Planning and Design*, 28(3):361–383, 2001.

[97] H. A. Makse, S. Havlin, P. R. King, and H. E. Stanley. Spontaneous stratification in granular mixtures. *Nature*, 386(6623):379–382, 1997.

[98] K. Wieghardt. Experiments in granular flow. *Annual Review of Fluid Mechanics*, 7(1):89–114, 1975.

[99] A. Garcimartín, J. M. Pastor, C. Martín-Gómez, D. Parisi, and I. Zuriguel. Pedestrian collective motion in competitive room evacuation. *Scientific Reports*, 7(1):1–9, 2017.

[100] J. Adrian, A. Seyfried, and A. Sieben. Crowds in front of bottlenecks at entrances from the perspective of physics and social psychology. *Journal of the Royal Society Interface*, 17(165):20190871, 2020.

[101] I. Zuriguel, I. Echeverria, D. Maza, R. C. Hidalgo, C. Martín-Gómez, and A. Garcimartín. Contact forces and dynamics of pedestrians evacuating a room: The column effect. *Safety Science*, 121:394–402, 2020.

[102] I. Echeverría-Huarte, I. Zuriguel, and R. C. Hidalgo. Pedestrian evacuation simulation in the presence of an obstacle using self-propelled spherocylinders. *Physical Review E*, 102(1):012907, 2020.

[103] Á. Garcimartín, D. Maza, J. M. Pastor, D. R. Parisi, C. Martín-Gómez, and I. Zuriguel. Redefining the role of obstacles in pedestrian evacuation. *New Journal of Physics*, 20(12):123025, 2018.

[104] J. Wang, K. Harth, D. Puzyrev, and R. Stannarius. The effect of obstacles near a silo outlet on the discharge of soft spheres. *New Journal of Physics*, 24(9):093010, 2022.

[105] D. M. Walker, A. Tordesillas, N. Brodu, J. A. Dijksman, R. P. Behringer, and G. Froyland. Self-assembly in a near-frictionless granular material: conformational structures and transitions in uniaxial cyclic compression of hydrogel spheres. *Soft Matter*, 11(11):2157–2173, 2015.

[106] B. Bischke, P. Helber, J. Folz, D. Borth, and A. Dengel. Multi-task learning for segmentation of building footprints with deep neural networks. In *2019 IEEE International Conference on Image Processing (ICIP)*, pages 1480–1484. IEEE, 2019.

[107] X. G. Qin, Y. Zhou, Y. H. Guo, D. Y. Wu, Z. H. Tian, N. Jiang, H. B. Wang, and W. P. Wang. Mask is all you need: Rethinking mask r-cnn for dense and arbitrary-shaped scene text detection. In *Proceedings of the 29th ACM International Conference on Multimedia*, pages 414–423, 2021.

[108] T. Y. Lin, M. Maire, S. Belongie, J. Hays, P. Perona, D. Ramanan, P. Dollár, and C. L. Zitnick. Microsoft coco: Common objects in context. In *European Conference on Computer Vision*, pages 740–755. Springer, 2014.

[109] B. Daniel, C. van der Wel, Nathan C. K., and Thomas A. C. Trackpy: Fast, flexible particle-tracking toolkit. 2012.

[110] B. Steffen and A. Seyfried. Methods for measuring pedestrian density, flow, speed and direction with minimal scatter. *Physica A: Statistical Mechanics and its Applications*, 389(9):1902–1910, 2010.

[111] D. Helbing, A. Johansson, and H. Z. Al-Abideen. Dynamics of crowd disasters: An empirical study. *Physical Review E*, 75(4):046109, 2007.

[112] W. Yu and A. Johansson. Modeling crowd turbulence by many-particle simulations. *Physical Review E*, 76:046105, 2007.

[113] A. Garcimartín, D. R. Parisi, J. M. Pastor, C. Martín-Gómez, and I. Zuriguel. Flow of pedestrians through narrow doors with different competitiveness. *Journal of Statistical Mechanics: Theory and Experiment*, 2016(4):043402, 2016.

[114] O. Reynolds. Experiments showing dilatancy, a property of granular material, possibly connected with gravitation. *Proc. Royal Institution of Great Britain*, 11(354363):12, 1886.

[115] A. Panaitescu, K. A. Reddy, and A. Kudrolli. Nucleation and crystal growth in sheared granular sphere packings. *Physical Review Letters*, 108(10):108001, 2012.

[116] J. A. Dijksman, N. Brodu, and R. P. Behringer. Refractive index matched scanning and detection of soft particles. *Review of Scientific Instruments*, 88(5):051807, 2017.

[117] P. Richard, P. Philippe, F. Barbe, S. Bourlès, X. Thibault, and D. Bideau. Analysis by x-ray microtomography of a granular packing undergoing compaction. *Physical Review E*, 68(2):020301, 2003.

[118] W. L. Zhang, K. E. Thompson, A. H. Reed, and L. Beenken. Relationship between packing structure and porosity in fixed beds of equilateral cylindrical particles. *Chemical Engineering Science*, 61(24):8060–8074, 2006.

[119] K. H. Hausser and H. R. Kalbitzer. Principles of nmr. In *NMR in Medicine and Biology*, pages 1–36. Springer, 1991.

[120] W. Wichmann. Magnetic resonance imaging (mri). In *Imaging of orbital and visual pathway pathology*, pages 18–23. Springer Verlag, 2002.

[121] R. W. Brown, Y.C. N. Cheng, E. M. Haacke, Michael R Thompson, and R. Venkatesan. *Magnetic resonance imaging: physical principles and sequence design*. John Wiley & Sons, 2014.

[122] R. Stannarius. Magnetic resonance imaging of granular materials. *Review of Scientific Instruments*, 88(5):051806, 2017.

[123] G. N. Hounsfield. Computerized transverse axial scanning (tomography): Part 1. description of system. *The British journal of radiology*, 46(552):1016–1022, 1973.

[124] G. M. Bydder and I. R. Young. Mr imaging: clinical use of the inversion recovery sequence. *Journal of Computer Assisted Tomography*, 9(4):659–75, 1985.

[125] D. B. Twieg. The k-trajectory formulation of the nmr imaging process with applications in analysis and synthesis of imaging methods. *Medical physics*, 10(5):610–621, 1983.

[126] P. Mansfield. Multi-planar image formation using nmr spin echoes. *Journal of Physics C: Solid State Physics*, 10(3):L55, 1977.

[127] R. Bammer. Basic principles of diffusion-weighted imaging. *European journal of radiology*, 45(3):169–184, 2003.

[128] L. Kjær, C. Thomsen, O. Henriksen, P. Ring, M. Stubgaard, and E. J. Pedersen. Evaluation of relaxation time measurements by magnetic resonance imaging: a phantom study. *Acta Radiologica*, 28(3):345–351, 1987.

[129] A. Panaitescu and A. Kudrolli. Experimental investigation of cyclically sheared granular particles with direct particle tracking. *Progress of Theoretical Physics Supplement*, 184:100–109, 2010.

[130] O. Kuwano, R. Ando, and T. Hatano. Crossover from negative to positive shear rate dependence in granular friction. *Geophysical Research Letters*, 40(7):1295–1299, 2013.

[131] A. Fall, G. Ovarlez, D. Hautemayou, C. Mézière, J. N. Roux, and F. Chevoir. Dry granular flows: Rheological measurements of the μ (i)-rheology. *Journal of Rheology*, 59(4):1065–1080, 2015.

[132] D. Fenistein, J. W. van de Meent, and M. V. van Hecke. Core precession and global modes in granular bulk flow. *Physical Review Letters*, 96(11):118001, 2006.

[133] J. Wang, Z. Farmani, J. A. Dijksman, C. Lübeck, O. Speck, and R. Stannarius. Characterization of shear zones in soft granular beds by means of a novel magnetic resonance imaging technique. *Granular Matter*, 24(4):1–13, 2022.

[134] J. Wang, K. Harth, R. Stannarius, B. Fan, and T. Börzsönyi. Discharge of soft and hard grains and their mixtures from 2d silos. *EPJ Web Conf.*, 249:03002, 2021.

Appendix: Symbols

p	pressure
μ	friction coefficient
s	side length of square
h	height of one layer in silos
m_s	the weight of the layer at height h in silos
Q	flow rate in weight per length per second
ρ	granular bulk density
ρ_p	density of particle material
d	the diameter of one spherical particle
r	the radius of one spherical particle
D	the width of the general orifice
R	the radius of the round orifice
g	gravity acceleration
v	the velocity of particles passing through the orifice
I	inertial number
$\dot{\gamma}$	shear rate
τ	shear stress
Φ	volume fraction
ϕ	packing fraction of the bulk
H	the thickness of granular beds in the split-bottom shear cell
R_s	the radius of the bottom disk of the split-bottom shear cell
Ω	the rotation angle of split-bottom shear cells

ω	the angular rotation speed
χ	the mass concentration of mixtures
x	the volume concentration of mixtures
X	the number fraction in an arch structure
E	Young's modulus
G	shear modulus
ν	Poisson ratio
τ_t	'clog duration'
P	the probability of forming a clog
S	an avalanche size
f	the precession frequency
γ	the gyromagnetic ratio
B_0	the external magnetic field
M	magnetization
μ_i	the magnetic moment of one spin
T_1,T_2	relaxation time
G'	a linear magnetic field gradient

Acknowledgements

Time flies. It's hard for me to find that the incredible research experience is going to the end. I hope to work with everyone in the future. In this Ph.D. study process, I learned a lot from not only the research life but also the daily life in Germany. Indeed, it's from my persistence and hard work that I accomplish my Ph.D. study. But it cannot be left out of so many people's kind, warm, selfless help and support for me. So here I'd like to thank all of them sincerely.

First and foremost, I want to thank my supervisor, Prof. Dr. rer. nat. Ralf Stannarius, thank you for allowing me to join the group where I can work with so many amazing colleagues and explore many interesting discoveries in the research, thank you for instructing, inspiring, and encouraging me when I met difficulties and felt confused about solving the problems during the study, thank you for your tolerance with giving me much free space that I can be myself with less pressure to confront every challenge during the study. I learned a lot from you, your creative perspectives and sharp mind in finding interesting topics among complicated but common physical phenomena, your wide knowledge and wise thoughts in explaining peculiar objective facts in physics, your diligent attitude on working, and your always strong curiosity in learning new things... In a word, I appreciate the time working with you.

I want to thank my colleagues in the group of Nonlinear Phenomena. I want to thank Dr. Kirsten Harth, thank you for your instructions on my work and your patience and encouragement when I encountered problems on research, thank you for your caring and reminder when I just came to the group and was very shy, and not talkative at the beginning. I also want to thank Dr. Dmitry Puzyrev, thank you for your kind help on the work, which inspired me to find a way to solve problems in research. Besides, I want to thank Dr. Torsten Trittel, thanks a lot for your generous assistance with the preparation of experimental setups and administrative matters in the role of a patient interpreter. Your designs of those setups are considerable and I value and respect your practical skills in carrying out experiments. In addition, I want to thank all the other members of the group for their support.

Then, I want to thank all members of the Caliper project. I want to thank Dr. Joshua A. Dijksman, thank you for your organization in many activities of the projects and your concerns about our work progress. And thank you for your host at Wageningen Univerisity. Your smart and sharp thinking impressed me a lot. It was my pleasure to work with you. Otherwise, I want to thank Dr. Tamás Börzsönly. Thank you for your guidance and for hosting me at Wigner Institute. I respect your low profile but diligence and seriousness in the research with a lot of experiences and accomplishments in the field of experimental physics. Furthermore, I want to thank Raúl Cruz Hidalgo, thank you for being the host at Navarra University, and thank you for helping me a lot with the simulation work. Your passion, sense of humor, and determined faith make the sometimes-dull research colorful and light. I appreciate that I have a chance to work with you. Moreover, I want to thank the colleagues who made contributions to this work, Zohreh Farmani, Bo Fan, and Tivadar Pongó. It was wonderful to collaborate with you and indeed we together worked out some scientific discoveries! What's more, I want to thank all the other members of this project. It was with great pleasure to study with you and work together in the granular field. Finally, I want to thank the funding support, of the European Union's Horizon 2020 research and innovation programme under the Marie Skłodowska Curie grant agreement No 812638.

Last but not least, I would like to thank all my friends, my family for their help and support. And thanks every reviewer of the thesis for precious suggestions.

Thank you for all!

Declaration of Honour

I hereby declare that I prepared this thesis without the impermissible help of third parties and that none other than the aids indicated have been used; all sources of information are clearly marked, including my own publications.

In particular, I have not consciously:

- Fabricated data or rejected undesirable results,
- Misused statistical methods with the aim of drawing other conclusions than those warranted by the available data,
- Plagiarized external data or publications,
- Presented the results of other researchers in a distorted way.

I am aware that violations of copyright may lead to injunction and damage claims by the author and also to prosecution by law enforcement authorities. I hereby agree that the thesis may be electronically reviewed with the aim of identifying plagiarism.

This work has not been submitted as a doctoral thesis in the same or a similar form in Germany, nor in any other country. It has not yet been published as a whole.

(place, date) (signature)